# Atomic and Molecular Manipulation with a Scanning Tunneling Microscope

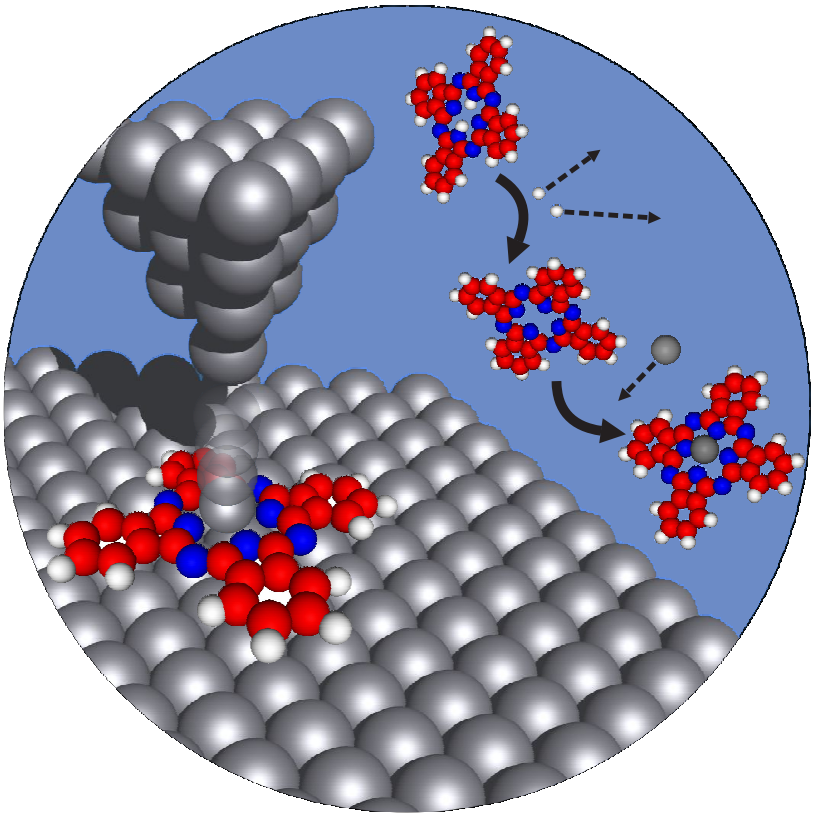

Dissertation

zur Erlangung des Doktorgrades
der Mathematisch-Naturwissenschaftlichen Fakultät
der Christian-Albrechts-Universität zu Kiel

vorgelegt von

**Alexander Sperl**

Kiel, April 2011

This work was typeset in LaTeX.

| | |
|---|---|
| Referent: | Prof. Dr. Richard Berndt |
| Korreferent: | Prof. Dr. Olaf Magnussen |
| Tag der mündlichen Prüfung: | 20.05.2011 |
| Zum Druck genehmigt: | 23.05.2011 |
| | gez. Prof. Dr. Lutz Kipp, Dekan |

# KURZDARSTELLUNG

In dieser Arbeit wurden strukturelle, elektronische und chemische Eigenschaften sowie dynamische Prozesse an adsorbierten Nanostrukturen mit einem Tieftemperatur-Rastertunnelmikroskop (RTM) untersucht.
Mittels atomarer Manipulationen wurde der Abstand zwischen zwei auf einer Ag(111)-Oberfläche adsorbierten Silberatomen variiert bis sie schließlich einen Dimer formten. Hierbei wurde die Veränderung der $sp_z$ Resonanz des Silberatoms, welche bei Annäherung an das zweite Silberatom in Richtung der Fermi-Energie schiebt, experimentell und theoretisch untersucht. Die theoretische Untersuchung zeigt, dass bei kleinen Abständen der Atome untereinander ($d_{\text{Ag-Ag}} \leq 1\,\text{nm}$) die Wechselwirkung zwischen den $sp_z$ Zuständen der Silberatome auf der Oberfläche ähnlich zwischen zwei $sp_z$ Orbitalen im Vakuum ist. Demzufolge sind indirekte Wechselwirkungen zwischen den Adatomen über das Substrat klein im Verhältnis zu den direkten Wechselwirkungen zwischen den Atomen.
Weiterhin wurde die laterale Translationsdynamik eines einzelnen Silberatoms auf einer Ag(111)-Oberfläche bei erhöhten Tunnelströmen untersucht. Die hier erzielte Zeitauflösung von 10 ns liegt etwa 1000mal höher als bei bisher publizierten Messungen [1–3], die ebenfalls mit einem konventionellen RTM aufgenommen wurden.[1] Bei erhöhten Tunnelströmen führt die außermittige Positionierung der Tunnelspitze über adsorbierten Atomen zu zufälligen Übergängen des Adatoms zwischen fcc und hcp Adsorptionsplätzen. Diese Übergänge machen sich als Fluktuationen im Tunnelstrom zwischen zwei diskreten Werten bemerkbar. Die Spannungsabhängigkeit dieser Fluktuationen wurde dazu benutzt, um effektive Temperaturen des Kontakts, welche von der relativen Position der Spitze zum Atom abhängen, sowie Diffusionsbarrieren des Adatoms, die in Anwesenheit der Spitze lediglich einige Millivolt betragen, abzuschätzen.
Unter Benutzung der Tunnelspitze wird zum ersten Mal die kontrollierte Metallisierung einzelner adsorbierter Phthalocyanine direkt auf der Oberfläche gezeigt. Hierbei erfordert die Konvertierung von $H_2$Pc zu AgPc verschiedene

[1] Andere Methoden wie z.B. das elektrochemische RTM [4,5] oder die Kombination aus RTM und optischer Anregung mit ultrakurzen Laserpulsen [6–8] erreichen Zeitauflösungen von $\mu$s bzw. sogar einigen fs.

Schritte, nämlich die schrittweise Entfernung von Wasserstoffatomen aus dem inneren Molekül sowie den darauffolgenden Einbau eines Silberatoms. Eine direkte Metallisierung des $H_2Pc$ wurde bei diesen Experimenten nicht beobachtet. Zusätzlich zu dem Metallisierungsprozess wurde mittels Anregungen durch Tunnelelektronen der Spitze die Tautomerisierung der inneren Wasserstoffatome beim $H_2Pc$ sowie das Schalten des verbliebenen Wasserstoffatoms beim HPc nachgewiesen. Nach jedem Reaktionsschritt wurde die elektronische Signatur des Moleküls mittels Rastertunnelspektroskopie bestimmt.
In einer Vorarbeit für die später gezeigte Demetallisierung wurde das Adsorptionsverhalten von Blei-Phthalocyaninen (PbPc) auf Blei-Inseln auf einer Ag(111)-Oberfläche untersucht. Im Gegensatz zu anderen (Metall-)Phthalocyaninen ordnet sich PbPc bereits bei kleinen Bedeckungen zu großen, wohldefinierten Anordnungen an. Als Vergleich hierzu werden Messungen für PbPc auf Ag(111) gezeigt. Für eine bestimmte Anordnung der PbPc Moleküle relativ zu den Blei-Inseln bildet sich eine elektronische Überstruktur mit einer extrem großen Einheitszelle von 22 Molekülen aus. Die Molekülorbitale sowie deren Wechselwirkungen mit Quantentrogzuständen der Blei-Inseln wurde mittels Rastertunnelspektroskopie untersucht.
Zusätzlich zur Metallisierung wird die erfolgreiche Demetallisierung einzelner Metall-Phthalocyanine zum ersten Mal gezeigt. Hierbei wird das zentrale Metallion eines PbPc Moleküls, welches auf Blei-Inseln auf einer Ag(111)-Oberfläche adsorbiert ist, zu der Tunnelspitze transportiert. Die erhöhte Länge der Spitze aufgrund des zusätzlichen Atoms sowie topographische und spektroskopische Signaturen des Phthalocyanins vor und nach der Demetallisierung erhärten die Annahme einer erfolgreichen Demetallisierung.
Abschließend wird die Entwicklung einer neuen Probenpräparationsstation beschrieben. Sie erlaubt Probentemperaturen von mindestens 2300 K, eine Bedampfung mit Metallen oder Molekülen bei zeitgleicher Heizung der Probe sowie eine spätere geplante Automatisierung des gesamten Reinigungsprozesses der Probenoberfläche, welche die Probenpräparation weiter vereinfachen soll.

# ABSTRACT

In this thesis structural, electronic, chemical properties and dynamic processes of adsorbed nanostructures on metal surfaces are investigated with a low-temperature scanning tunneling microscope (STM).
Atomic manipulation was used to vary the interatomic distance between two Ag atoms adsorbed on Ag(111) up to the formation of a dimer. In a combined experimental and theoretical study the evolution of a Ag monomer $sp_z$ resonance is investigated, which shifts toward the Fermi level upon approaching the second Ag atom. The theoretical analysis indicates that, at close adatom–adatom distances ($d_{\text{Ag-Ag}} \leq 1\,\text{nm}$), the interaction between the $sp_z$ electronic states of the Ag atoms on the surface is similar to the direct interaction between the two $sp_z$ orbitals in vacuum. Therefore, indirect interactions between the two adatoms via the substrate are small compared to direct contributions.
Lateral translation dynamics of Ag atoms adsorbed on Ag(111) at elevated tunneling currents are investigated with a time resolution of 10 ns, which is an improvement by three orders of magnitude compared to previously published works with conventional STM [1–3].[2] Positioning the tip off the center of an adsorbed atom at elevated tunneling conductances induces random transitions between fcc and hcp adsorption sites, which induce to two-level fluctuations of the tunneling conductance. The voltage dependence of these fluctuations was used to extract effective junction temperatures, which depend on the relative position of the tip to the adatom, and drastically lowered diffusion barrier heights for the adatom of several millivolts only in the presence of the tip.
Using the STM tip the controlled metalation of a single adsorbed phthalocyanine molecule directly on the surface is demonstrated for the first time. The conversion of single $H_2Pc$ molecules to AgPc requires several steps, namely stepwise dehydrogenation of the inner macrocycle and subsequent implantation of a Ag ion. Direct metalation of $H_2Pc$ was not observed in this type of experiment. In addition to the metalation process, hydrogen tautomerization

[2] Another methods like electrochemical STM [4, 5] or the combination of STM with optical excitation using ultrashort laser pulses [6–8] enable time resolutions of $\mu$s or even some fs, respectively.

of $H_2Pc$ and hopping of a single hydrogen in the inner macrocycle of HPc were induced by electron injection from the STM tip. After each reaction step the electronic fingerprint of the product was determined by scanning tunneling spectroscopy (STS).
In a preliminary work for the demetalation shown later the adsorption behavior of lead-phthalocyanine (PbPc) molecules adsorbed to Pb islands on Ag(111) is reported. In contrast to other phthalocyanines, PbPc aggregates into large, ordered assemblies even at low coverages. Data from PbPc on Ag(111) are shown for comparison. For a particular orientation of PbPc on Pb on Ag(111) we find that the electronic structure of the molecules is periodically modulated, which leads to an electronic superstructure with a very large unit cell containing 22 molecules. Scanning tunneling spectroscopy is used to probe the molecular states and their interaction with quantum well states, which are characteristic of the underlying Pb islands.
The successful controlled demetalation of single adsorbed metal-phthalocyanines is demonstrated for the first time by transferring the central metal ion of PbPc molecules adsorbed on ultrathin Pb films on Ag(111) from the inner macrocycle to the apex of the tip. The increased length of the tip and the spectroscopic fingerprints of reactants and products provide clear evidence for the demetalation process. Reactants and products are discriminated by their images and spectroscopic fingerprints.
Additionally a new sample preparation station is presented. It allows sample temperatures in excess of 2300 K, an evaporation of metals and molecules during sample heating and for the future a planned automatization of the whole sputter and annealing process, which will further facilitate the experimental preparation.

# CONTENTS

# 1. INTRODUCTION

The ongoing miniaturization in electronic devices, described by Moore's law, leads to structures at the nanometer scale. While the first transistor, invented 1947 at the Bell labs, had a size of 10 cm the recently presented newest generation of processors is based on the 32 nm node. The 16 nm node is expected to be reached by semiconductor companies in 2013 and the 11 nm node in 2015. With ongoing miniaturization the distance between identical features in an array will decrease and the nanostructures are brought closer together. In the near future the limits of the "top-down" lithographic process will be approached. Replacing this process by the "bottom-up" approach is one promising way towards technology on the nanometer scale. Here, single adsorbed atoms (adatoms) or molecules are arranged step by step forming more complex assemblies. To understand the principles during formation of such nanostructures a detailed investigation of the merging of adatoms is of fundamental interest. When adatoms are brought together to form a cluster, their outer wave functions overlap and the energy levels shift resulting in a change of their electronic, magnetic, and chemical properties. Systematic studies of the distance dependence of the interaction of single atoms on surfaces is required which is in contrast to the number of publications to this topic so far [9].
Additionally, for nanoscale electronics the electrical stability of nanostructures is one of the most important properties. Therefore, it is highly interesting to investigate the stability of single adatoms with current before studying electrical stability of nanostructures containing a few up to hundreds of atoms.

Instead of adatoms or clusters molecules can also be used in nanotechnology. The focus of research is to develop molecules with useful electronic, or chemical properties, which could then be used as single-molecule components in nanoscale devices. Metal-phthalocyanine and -porphyrin molecules appear particularly suitable for this task, because these molecules are cheap to produce, have a high thermal stability and exhibit an intriguing variety of functional properties, which allow the application of such molecules as data storage units, sensors, or dyes [10, 11]. The specific properties of such

molecules are determined by the metal ion in the center. From a nanotechnological point of view it is interesting to controllably remove the metal atom in the center and exchange it by another to tune the properties of the molecule directly on the surface. Such a tool box for the construction of molecules would be a step for the "bottom-up" approach of molecular components.

Since its invention by Gerd Binnig and Heinrich Rohrer in 1981 [12] the scanning tunneling microscope (STM) has proved to be an extremely powerful tool for the characterization of surfaces at the atomic scale. Additionally to the characterization the STM tip can achieve atomic and molecular manipulations such as dragging of adsorbates [13–15] or pick-up and release atoms and molecules [16–21]. Therefore, it is a promising tool for the construction of surface supported nanostructures like atomic chains [19, 22–26], two dimensional clusters [26–29], or atom-molecule-hybrids [30].

One aim of this thesis is to contribute to the fundamental understanding of interactions between single adatoms and dynamic processes of single adatoms on the surface. Another aim is to show the controlled tuning of the properties of single phthalocyanine molecules directly on the surface, *i. e.*, the metalation of phthalocyanine and demetalation of metal-phthalocyanine molecules.

This thesis is organized as follows. Chapter 2 gives a short introduction in the basic principles of scanning tunneling microscopy and scanning tunneling spectroscopy. Further, atomic and molecular manipulations with the STM and time-resolved measurements in STM are discussed.
In Chapter 3 atomic manipulation was used to vary the interatomic distance between two Ag adatoms on Ag(111) up to formation of a dimer. In a combined experimental and theoretical study the evolution of a Ag monomer $sp_z$ resonance is investigated, which shifts toward the Fermi level upon approaching the second Ag atom.
Chapter 4 contains a study of lateral translation dynamics of Ag atoms adsorbed on Ag(111) at elevated tunneling currents. Positioning the tip off the center of an adsorbed atom at elevated tunneling conductances induces random transitions between fcc and hcp adsorption sites, which are related to two-level fluctuations of the tunneling conductance.
In Chapter 5 the controlled metalation of a single adsorbed phthalocyanine molecule is demonstrated for the first time. In addition to the metalation process, hydrogen tautomerization of $H_2$Pc and hopping of a single hydrogen in the inner macrocycle of HPc were induced by electron injection from the STM tip.

In Chapter 6 the adsorption behavior of lead-phthalocyanine (PbPc) molecules adsorbed to Pb islands on Ag(111) is reported. For a particular orientation of PbPc on Pb on Ag(111) we find that the electronic structure of the molecules is periodically modulated, which leads to an electronic superstructure with a very large unit cell containing 22 molecules.
In Chapter 7 single adsorbed metal-phthalocyanines have been demetalized for the first time by transferring the central metal ion of PbPc molecules adsorbed on ultrathin Pb films on Ag(111) from the inner macrocycle to the apex of the tip. Reactants and products are discriminated by their images and spectroscopic fingerprints.
Finally, in the Appendix a new sample preparation station which permits sample temperatures in excess of 2300 K is presented.

The main parts of this thesis have been published, are accepted for publication in or submitted to peer reviewed journals as indicated below:

- Parts of Chapter 2 have been published as
  *Local Density of States from Constant-Current Tunneling Spectra*,
  M. Ziegler, N. Néel, A. Sperl, J. Kröger, and R. Berndt,
  Phys. Rev. B **80**, 125402 (2009).

- Chapter 3 has been published as
  *Evolution of Unoccupied Resonance during the Synthesis of a Silver Dimer on Ag(111)*,
  A. Sperl, J. Kröger, R. Berndt, A. Franke, and E. Pehlke,
  New J. Phys. **11**, 063020 (2009).

- Chapter 4 has been published in large parts as
  *Direct Observation of Conductance Fluctuations of a Single-Atom Tunneling Contact*,
  A. Sperl, J. Kröger, and R. Berndt,
  Phys. Rev. B **81**, 035406 (2010).

  and

  *Conductance of Ag Atoms and Clusters on Ag(111): Spectroscopic and Time-Resolved Data*,
  A. Sperl, J. Kröger, and R. Berndt,
  Phys. Status Solidi B **247**, 1077 (2010).

and

*Scanning tunneling microscopic investigations into the conductance of single-atom junctions*,
J. Kröger, A. Sperl, N. Néel, and R. Berndt,
J. Scan. Prob. Microsc. **4**, 49 (2009).

- Chapter 5 will be published as
  *Controlled Metalation of a Single Adsorbed Phthalocyanine*,
  A. Sperl, J. Kröger, and R. Berndt,
  Angew. Chem. Int. Ed. **50**, 5294 (2011), Hot Paper.

- Chapter 6 will be published as
  *Electronic Superstructure of Lead-Phthalocyanine on Lead Islands*,
  A. Sperl, J. Kröger, and R. Berndt,
  accepted for publication in J. Phys. Chem. A (2011).

- Chapter 7 is based on
  *Demetalation of a Single Organometallic Complex*,
  A. Sperl, J. Kröger, and R. Berndt,
  submitted to J. Am. Chem. Soc..

# 2. SCANNING TUNNELING MICROSCOPY AND SPECTROSCOPY

The scanning tunneling microscope (STM) was invented in 1981 by Gerd Binnig and Heinrich Rohrer at IBM Zürich [12]. Five years later they were awarded the Nobel prize in physics for its invention. Since its invention the STM has proved to be an extremely powerful tool for many disciplines in condensed-matter physics, chemistry, and biology. It enables the resolution of the local atomic and electronic structures of conducting solid surfaces.
With the STM tip positions of atoms and molecules can be manipulated. Therefore, the STM is an ideal tool for experiments in surface science. For a detailed description of the home–built STM used for this thesis the reader is referred to Reference [31].

In this chapter, the basic principles of scanning tunneling microscopy and scanning tunneling spectroscopy (STS) are introduced. For a more detailed description the reader is referred to the existing textbooks on this topic [32–38]. Further, atomic and molecular manipulations with the STM and time-resolved measurements in STM are discussed. While conventional STM measurements up to now allowed time resolutions as low as $10 - 100\,\mu$s [1–3] the time resolution of the experiments presented here are increased by a factor of 1000 to $\leq 10\,$ns.[1] This allows a detailed investigation of dynamic processes of adsorbates on surfaces.

## *2.1 Principles*

In an STM a sample voltage is applied between a sharp conductive tip and a conducting surface. When the tip is approached to a close proximity of some angstroms to the sample surface a tunneling current occurs.
Figure 2.1 shows a schematic diagram of the tunneling barrier. Two metallic electrodes are separated by a small tunneling gap. At a temperature of

[1] Another methods like electrochemical STM [4, 5] or the combination of STM with optical excitation using ultrashort laser pulses [6–8] enable time resolutions of $\mu$s or even some fs, respectively.

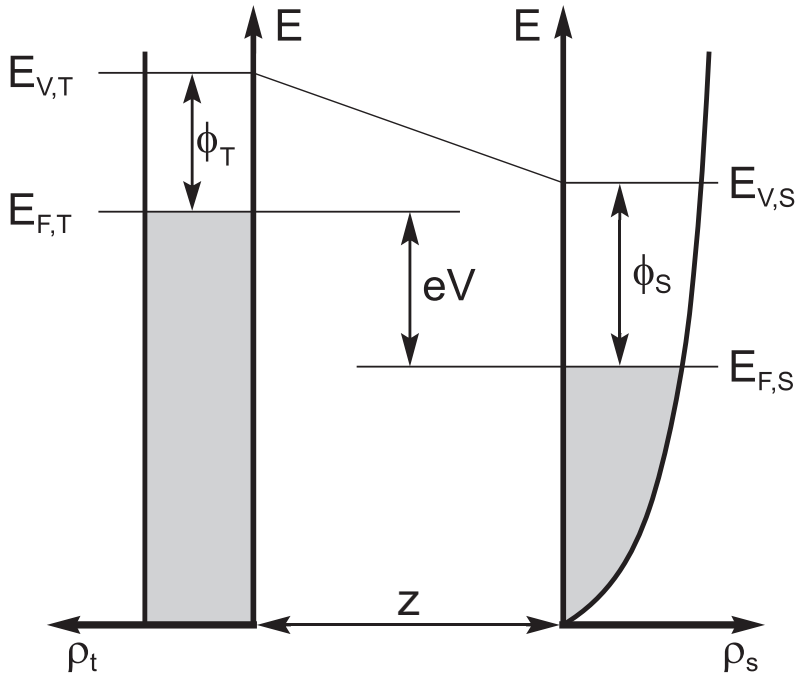


*Fig. 2.1:* Schematic diagram of the tunneling barrier of width $z$ between an ideal tip with flat density of states, $\rho_T$, and a sample with a varying density of states, $\rho_S$. The energy bands of tip and sample are filled up with electrons up to the Fermi energies $E_{F,T}$ and $E_{F,S}$, respectively. The difference between the vacuum energy levels ($E_{V,T}$ and $E_{V,S}$) and the Fermi levels are the work functions $\phi_T$ and $\phi_S$. When a positive voltage, $V$, is applied to the sample with respect to the tip, electrons from occupied tip states are able to tunnel into unoccupied sample states. The tunneling barrier appears approximately with a trapezoidal shape in this one-dimensional description.

$T = 0\,\mathrm{K}$ the electrons are filled up to the Fermi energies of the sample, $E_{F,S}$, and the tip, $E_{F,T}$, indicated by the gray shaded areas in Figure 2.1. When a positive voltage is applied to the sample the Fermi energies are shifted by $eV$ relative to each other. In the Wentzel-Kramers-Brillouin (WKB) approximation the transmission probability, $T(z, V, E)$, for an electron to tunnel through a one-dimensional trapezoidal barrier of width $z$ from the tip to the sample is expressed as

$$T(z, V, E) \propto \exp\left(-\alpha z \sqrt{\phi + \frac{eV}{2} - E}\right) \tag{2.1}$$

with $\alpha = 2\sqrt{2m}/\hbar$ ($m$: free electron mass; $\hbar$: reduced Planck's constant, $-e$: electron charge) and $\phi = \frac{\phi_S + \phi_T}{2}$ the average work function from sample, $\phi_S$, and tip, $\phi_T$ [39, 40].

For low temperatures, *i. e.*, $T \ll eV/k_B$ ($k_B$: Boltzmann's constant), the tunneling current at a tip–sample distance $z$ and a bias voltage $V$ is expressed as

$$I(z, V) \propto \int_0^{eV} \rho_S(E)\rho_T(E - eV)T(z, V, E)dE, \tag{2.2}$$

where $\rho_S$ and $\rho_T$ are the local densities of states of, respectively, the sample and the tip, and $E$ denotes the energy of states participating in the tunneling process [41].

To extract the LDOS of the sample, the first derivative of the tunneling current with respect to the tip–sample voltage, *i. e.*, the differential conductivity, $dI/dV$, is usually analyzed:

$$\begin{aligned} \frac{dI}{dV} \propto\ & \rho_S(E)\rho_T(E - eV)T(z, V, E) \\ & + \int_0^{eV} \rho_S(E)\frac{d\rho_T(E - eV)}{dV}T(z, V, E)dE \\ & + \int_0^{eV} \rho_S(E)\rho_T(E - eV)\frac{dT(z, V, E)}{dV}dE. \end{aligned} \tag{2.3}$$

The second and third terms are usually neglected assuming constant LDOS of the tip ($\frac{d\rho_T(E-eV)}{dV} \sim 0$) and only monotonous changes in the transmis-

sion probability at small tip–sample biases ($\frac{dT(z,V,E)}{dV} > 0$) [42]. Under these assumptions the differential conductivity can be approximated as

$$\frac{dI}{dV} \propto \rho_S(E)T(z,V,E). \tag{2.4}$$

The $dI/dV$ spectra can be directly measured by means of standard lock-in technique and hence, it is possible to probe the LDOS of the surface with atomic scale resolution.

## 2.2 Operation Modes

### 2.2.1 Imaging

The images presented in this thesis were exclusively acquired in the constant-current mode. Here, the tunneling current is kept constant using a feedback loop circuit, which varies the tip–sample distance. The vertical displacement of the tip reflects the surface topography as well as electronic surface structure. For a constant LDOS of the sample, the vertical displacement corresponds to the geometric height variation of the surface.
Another imaging mode of STM is the constant-height mode. In this mode the vertical tip displacement is kept constant during scanning. Since the feedback loop is disabled the tunneling current varies due to the different tip–sample distances. With this imaging mode a faster data acquisition compared to constant-current mode is feasible. However, this method is restricted to very flat surfaces, otherwise a tip crash may occur.

### 2.2.2 $dI/dV$ Spectroscopy

Scanning tunneling spectroscopy of the differential conductance is performed at constant-current and at constant-height as well. Spectra acquired in constant-height mode show smaller deviations from the real LDOS than constant-current spectra [43, 44]. Nevertheless it can be advantageous to record spectra at constant current, which implies varying vertical distances during spectroscopy. For instance, this allows to cover a wide range of voltages in a single spectrum avoiding a drastic increase of the tunneling current. However, the influence of the varying tip–sample distance on constant-current data is significant and should be taken into account in the data analyzing. Mapping of $dI/dV$ simultaneously with recording of a constant-current topograph can be performed conveniently. Similar maps at constant-height are sometimes difficult to achieve when the investigated surface exhibits

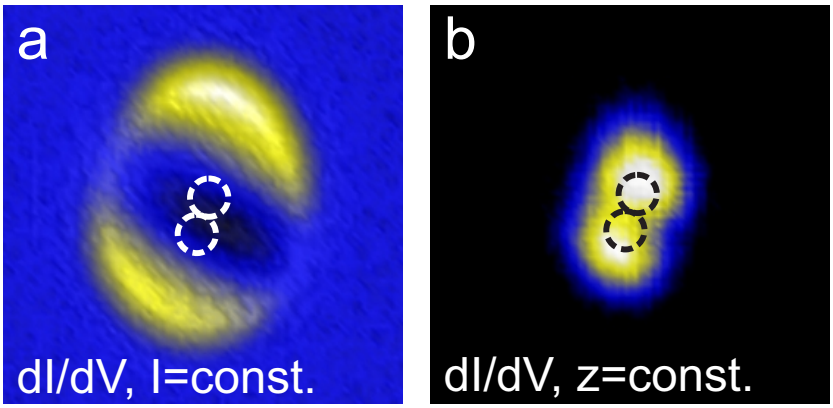


*Fig. 2.2:* Constant-current (a) and constant-height (b) map of $dI/dV$ recorded at a Ag dimer on Ag(111) at a sample voltage of 3.5 V (3 nm × 3 nm). The current in the constant-current map was set to 1 nA. For the constant-height map the feedback loop was opened atop the center of the dimer. Dashed circles indicate the positions of the dimer atoms.

prominent topographic features. Indeed, a number of recent publications reported constant-current spectra which were analyzed assuming that constant-current $dI/dV$ reflect the density of states [45–47]. The validity and precision of this assumption are questionable [43, 48].

Constant-current mode significantly affect peak positions and line shapes in spectra as well as patterns in spatial maps of the differential conductance [43, 44]. In an effort to measure the spatial distribution of an antibonding resonance of a Ag dimer adsorbed on Ag(111), maps of $dI/dV$ were acquired at constant-current and at constant-height (Figure 2.2).[2] While in the constant-current image sickle-shaped maxima are visible at both ends of the dimer (dashed circles in Figure 2.2 indicate the positions of the Ag atoms of the dimer), in the constant-height image the maxima have circular shape. Furthermore, the spatial extension of the dimer signal is strongly reduced compared to the constant-current $dI/dV$ map. The origin of these deviations between constant-current and constant-height mode is related to the vertical movement of the tip during the constant-current data acquisition. In Reference [43] a simple normalization scheme is shown, which takes into account experimental current–height characteristics. Including the third term in Equation (2.3), which is often neglected, approximately leads to

$$\frac{dI}{dV} \propto \rho_S(E)\rho_T(E-eV)T(z,V,E) - \frac{\alpha z}{\sqrt{\phi}} I(V). \tag{2.5}$$

[2] A detailed discussion of the antibonding resonance can be found in Chapter 3.

Allowing a variation of the tip–sample distance, $z(V)$, then leads to

$$\rho_S(E) \propto \frac{1}{eT(z(V),V,E)} \left\{ \frac{dI}{dV} + \frac{e\alpha z(V)}{\sqrt{\phi}} I_0 \right\}, \tag{2.6}$$

where $I_0$ is the constant current set for the measurements. Equation (2.6) suggests that the LDOS can be determined from constant-current spectra if $z(V)$ is available. While the absolute distance, $z(V)$, is not known in experiments, measuring a tip excursion, $\Delta z(V)$, is simple and can be done simultaneously with recording $dI/dV$. A reference distance $z_0$ has to be estimated to obtain $z = z_0 + \Delta z$.
Nevertheless, this normalization scheme cannot be applied to constant-current spectra in all cases. For the constant-current spectra later shown in Figure 6.8 an application of the normalization scheme leads to misleading results for the LDOS, *i. e.*, the extracted LDOS varies with voltage over 4 orders of magnitude. Most likely the reason is the combination of the assumption of a one-dimensional tunneling junction in the model and the huge retraction of the tip during data acquisition ($\Delta z \approx 0.7\,\mathrm{nm}$).

For further methods of extracting the LDOS of the sample from experimental $dI/dV$ curves the reader is referred to References [42, 48–51].

### *2.2.3 Atomic Manipulation*

The tip of an STM always exerts a force to the surface. This force contains both Van der Waals and electrostatic contributions. By adjusting the position and the voltage of the tip both the magnitude and direction of this force can be tuned. In particular, the possibility of inducing motion of atomic adsorbates was demonstrated in the early 1990s by Eigler and Schweizer [13].

To move an adsorbed atom (adatom) we follow the sequence of steps depicted in Figure 2.3, which was described for the first time by Eigler and Schweizer [13]. As a first step the tip is placed directly above the adatom to be moved. The tip–atom interaction is increased by lowering the tip toward the adatom (a); this is achieved by changing the required tunneling current to a higher value. Then the tip is moved across the surface (b). The adsorbate follows the tip by hopping from one surface binding site to the next. The tip is then retracted by reducing the tunneling current to the value used for imaging. An experimental example of atomic manipulation is shown in Figure 2.4. Here, three single adatoms and one cluster containing firstly an unknown number of atoms are shown (a). By increasing the tunneling current to $1.5\,\mu\mathrm{A}$ at a sample voltage of $0.1\,\mathrm{V}$, lateral translations of single adatoms

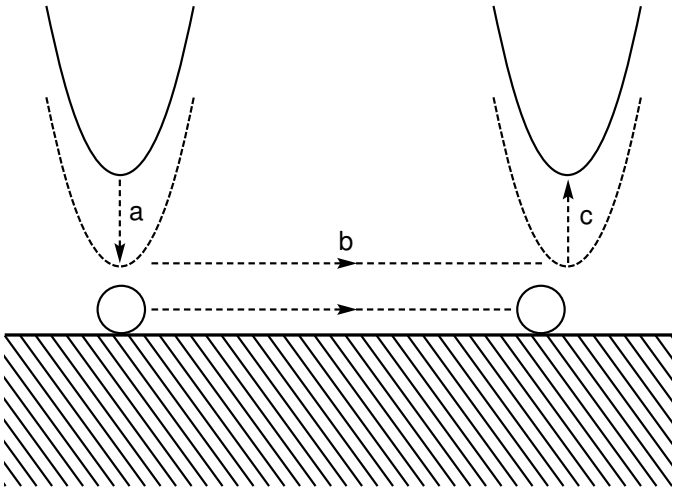


*Fig. 2.3:* A schematic illustration of the process for sliding an atom across a surface. (a) The tip is lowered to the position, where the atom-tip attractive force is sufficient to keep the atom located beneath the tip when the tip is subsequently moved across the surface (b) to the desired destination. (c) Finally, the tip is retracted to a position where the atom-tip interaction is negligible, leaving the atom bound to the surface at a new location. Figure adapted from Reference [13].

are feasible (b–d). The coalescence of two adatoms leads to the creation of a dimer with its typical shape (e) [26]. Lateral translations are sometimes accompanied by rotation of the dimer by 60° due to the hexagonal symmetry of the surface (f–j). The coalescence of the dimer and an adatom results in the fabrication of a compact trimer (k). The similarity of both clusters indicates that the lower cluster of initially unknown size contains three atoms as well. With this technique the low-temperature scanning tunneling microscope offers the unique opportunity to fabricate surface-supported model structures atom by atom, for example quantum corrals [52–57] or atomic wires [19, 22–26, 58, 59].

In this thesis tip-induced atomic manipulation was used to vary the interatomic distance between two Ag adatoms on Ag(111) in Chapter 3 and to induce lateral translations of a single Ag adatom between two adjacent adsorption sites on Ag(111) in Chapter 4.

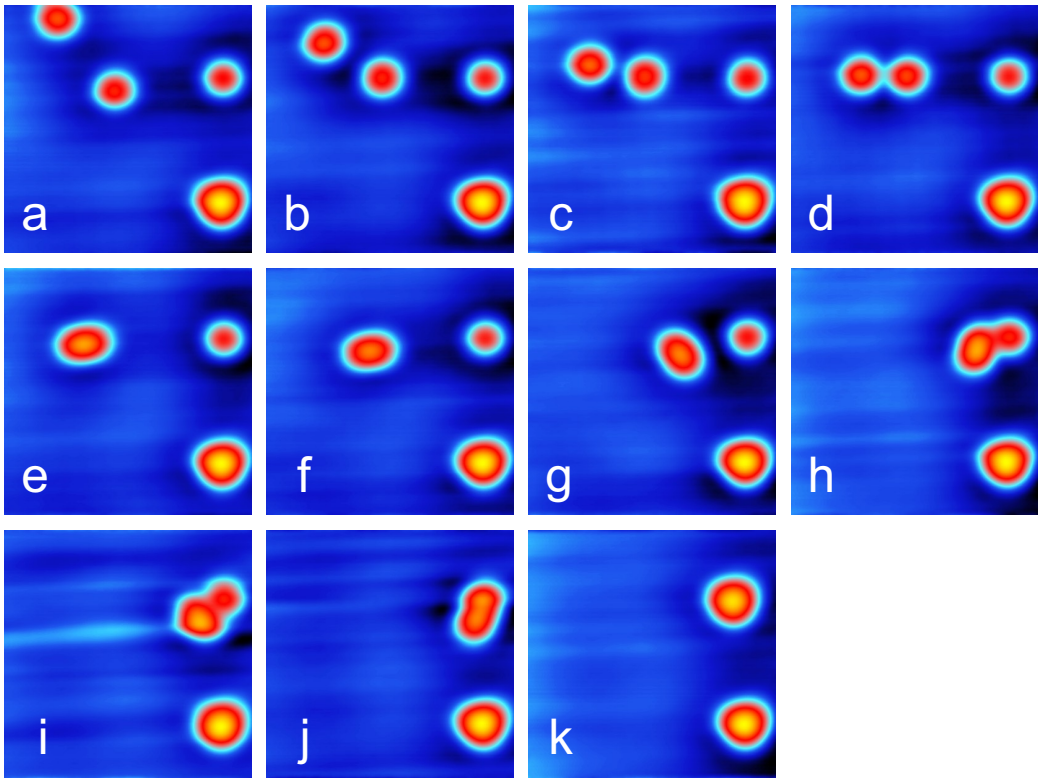


*Fig. 2.4:* Constant-current STM images of single Ag adatoms on Ag(111) whose lateral positions had been manipulated using the tip of the STM (2.1 nm× 2.1 nm, $V = 0.1$ V, $I = 0.1$ nA). (a) Three single adatoms and one cluster containing firstly an unknown number of atoms. (b–e) Construction of a dimer by atomic manipulation. (f–j) Lateral translations are sometimes accompanied by rotation of the dimer by 60° due to the hexagonal symmetry of the surface. (k) The coalescence of the dimer and an adatom result in the fabrication of a compact trimer. The similarity of both clusters indicates that the lower cluster contains three atoms as well.

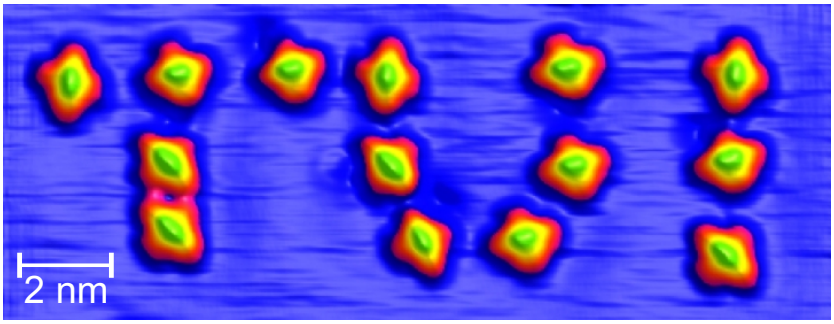


*Fig. 2.5:* Processed constant-current STM image of lead-phthalocyanine molecules on Ag(111) forming the initials TUI (Technische Universität Ilmenau). The molecules were laterally positioned with the STM tip at $V = 0.1\,\mathrm{V}$ and $I = 470\,\mathrm{nA}$. ($V = -0.1\,\mathrm{V}$, $I = 0.1\,\mathrm{nA}$)

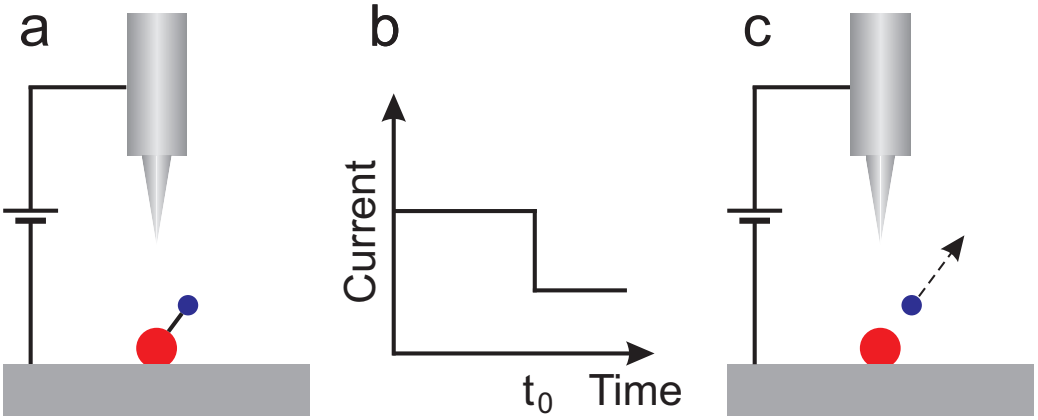


*Fig. 2.6:* Sketch for the tip induced dissociation of H from a molecule. (a) The tip is positioned atop the adsorbed molecule and a voltage pulse is applied. (b) Simultaneously the tunneling current is measured as a function of the time. (c) At time $t_0$, when the dissociation of the H atom occurs, the current signal decreases abruptly.

### 2.2.4 Molecular Manipulation

Manipulation of single molecules is feasible in an analogous manner as described for single atoms. In Figure 2.5 single lead-phthalocyanine molecules were positioned with the STM tip at $V = 0.1\,\mathrm{V}$ and $I = 470\,\mathrm{nA}$ on Ag(111) forming the initials TUI (Technische Universität Ilmenau). Furthermore, molecular manipulation such as conversion of conformations [60–71], chiral switching [72, 73], rotation of molecules [74–76], creation of bonds between molecules [77–79], dissociation of peripheral H atoms [80–83], or decomposition of the molecules [84, 85] have been performed up to now. In this sense, the STM constitutes a very powerful tool for single molecule chemistry. Additionally to Van der Waals and electrostatic forces the electrical current can be used for molecular manipulation. For the dehydrogenation processes described in Chapter 5 electrons with the required energy were injected with sub-angstrom precision at a specific site into the molecule. Upon dissipation of the electron energy into molecular vibrational degrees of freedom the hydrogen atom was detached from the molecule. A sketch for the tip induced dissociation of H from a molecule is presented in Figure 2.6. While the tip is positioned atop the adsorbed molecule a voltage pulse is applied. Simultaneously the tunneling current is measured as a function of the time. An abrupt drop in the current signals the successful dissociation. For other manipulations such as hydrogen tautomerization [64] or switching between bistable positions [68, 69, 73] instead of an abrupt drop an abrupt jump may occur in the current trace.

In this thesis STM induced molecular manipulation by the injection of electrons with the tip was used to induce hydrogen tautomerization, stepwise dehydrogenation, metalation, and switching of single phthalocyanine molecules in Chapter 5 and to demetalize lead-phthalocyanine molecules in Chapter 7.

## 2.3 Time-Resolved Measurements

Since the early 1990s the STM is used to investigate dynamical processes on surfaces, such as lateral diffusion of adatoms [1, 2, 86–88], contact to surfaces, adatoms, and molecules [89–93], molecular switches [62–70, 73], rotation of molecules [74–76], bond breaking of molecules [80–82, 84], or charging of adatoms on insulating films [94]. For these processes the time dependence of the tunneling current can be used to extract information such as diffusion barriers, attempt frequencies, vibrational heating or the number of electrons triggering the dynamic process [1, 2, 86–88]. An important limitation for such

FEMTO DLCPA-200, Setting: Low Noise

| Transimpedance (V/A) | $10^3$ | $10^4$ | $10^5$ | $10^6$ | $10^7$ | $10^8$ | $10^9$ |
|---|---|---|---|---|---|---|---|
| Cut-Off Frequency (-3db) (kHz) | 500 | 500 | 400 | 200 | 50 | 7 | 1.2 |
| Noise Current (fA/$\sqrt{\text{Hz}}$) | 20000 | 2300 | 460 | 130 | 43 | 13 | 4.3 |

FEMTO DHCPA-100, Setting: High Speed

| Transimpedance (V/A) | $10^3$ | $10^4$ | $10^5$ | $10^6$ | $10^7$ | $10^8$ |
|---|---|---|---|---|---|---|
| Cut-Off Frequency (-3db) (kHz) | 175000 | 80000 | 14000 | 3500 | 1800 | 220 |
| Noise Current (fA/$\sqrt{\text{Hz}}$) | 140000 | 6000 | 1500 | 450 | 150 | 55 |

*Tab. 2.1:* Performances depending on gain setting of the FEMTO DLCPA-200 and the FEMTO DHCPA-100 transimpedance amplifiers, which can be applied to the experimental setup.

time-resolved measurements is the time resolution of STM. While for imaging and spectroscopy preferably a low noise performance instead of an improved time resolution is required, for time-resolved measurements the situation is inverted. Therefore, two different transimpedance amplifiers can be used for the home-built STM. For low noise measurements the FEMTO DLCPA-200 and for a high time resolution the FEMTO DHCPA-100.
In Table 2.1 the performances of both transimpedance amplifiers depending on the gain settings are shown. Under normal imaging conditions ($I = 0.1\,\text{nA}$) a gain of $10^9\,\text{V/A}$ is required in the experimental setup. The upper cut-off frequency ($-3\,\text{dB}$) of the DLCPA-200 is then 1.2 kHz and the noise current $4.3\,\text{fA}/\sqrt{\text{Hz}}$. Approaching the tip towards the surface results in an increase of the tunneling current. Thus, the required transimpedance can be reduced resulting in an increased cut-off frequency and a higher noise current, which mostly does not bother the measurement. When the tip is brought close to contact the transimpedance can be reduced down to $10^4\,\text{V/A}$. Then the upper cut-off frequency of 500 kHz allows a time resolution of the order of some $\mu$s, which was up to now the lowest limit of time-resolved STM measurements [1–3].
By using the FEMTO DHPCA-100 the time resolution can be increased by orders of magnitude. For example, setting the transimpedance to $10^4\,\text{V/A}$ results in an upper cut-off frequency of 80 MHz (Table 2.1). Thus, a time resolution of some ns is feasible for the transimpedance amplifier. However, while the upper cut-off frequency for the DLPCA-200 is constant up to source capacitances of 1 nF [96], the upper cut-off frequency of the DHPCA-

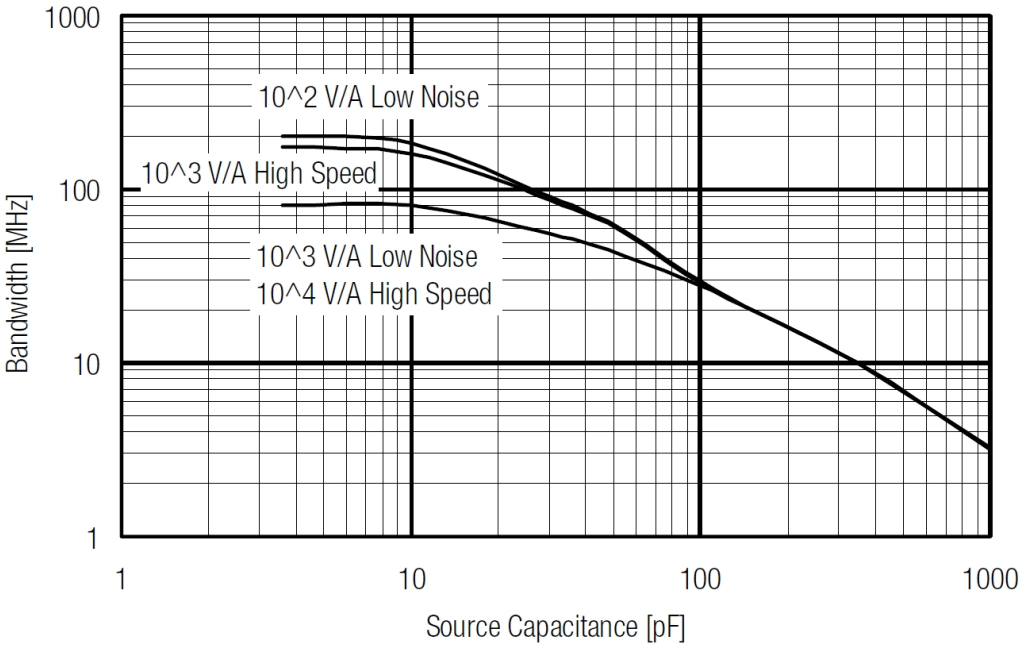


*Fig. 2.7:* Dependence of upper cut-off frequency (−3 dB) of the DHPCA-100 on source capacitance. Figure adopted from Reference [95].

100 depends on the source capacitance as shown in Figure 2.7. Increasing the source capacitance decreases the cut-off frequency rapidly. In the experimental setup the capacitance of the shielded cable carrying the tunneling current from the tip of the microscope to the amplifier is 50 pF/m. With the length of the cable in the experimental setup of ≈ 2 m the total source capacitance at the input of the transimpedance amplifier is ≈ 100 pF.[3] Therefore, the upper cut-off frequency for a transimpedance of $10^4$ V/A is ≈ 30 MHz (Figure 2.7).

To test the response of the transimpedance amplifier to sharp variations of the current which are typical of dynamic processes the experimental setup as schematically drawn in Figure 2.8a was built. A voltage pulse of a time duration of ≈ 840 ns with fall and rise times of the pulse of ≈ 3 ns (indicated by the black dashed vertical lines) was applied to a resistor of 100 kΩ simulating the tunneling barrier. The current through the resistor was then converted by the DHPCA-100 in a voltage. This voltage was recorded by a fast oscilloscope with a sampling rate up to 4 GSa/s together with the voltage

[3] For an STM with the focus on time-resolved measurements the source capacitance has to be decreased by using a shorter cable for the tunneling current to at most 10 pF. Then, the transimpedance amplifier has its full maximum bandwidth (Figure 2.7).

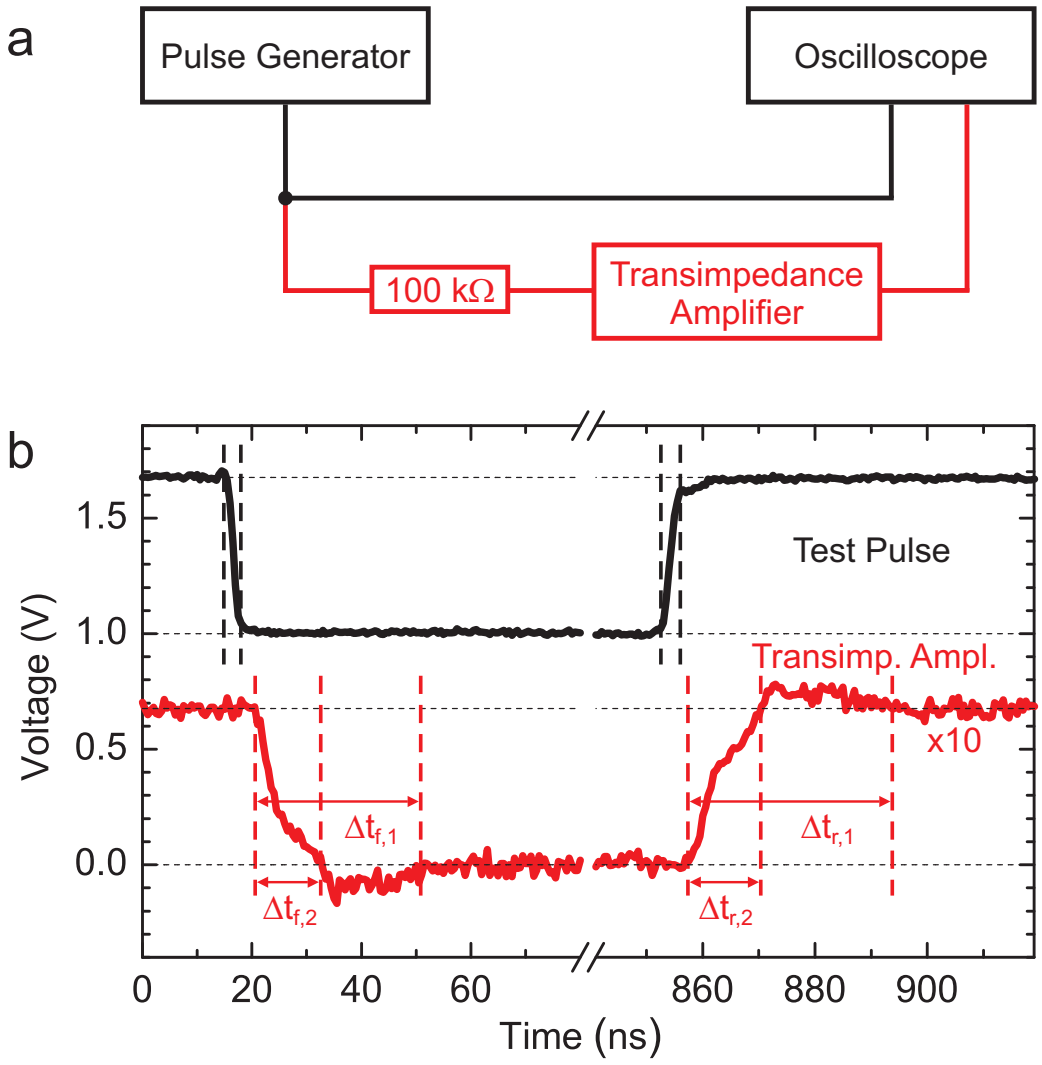


*Fig. 2.8:* (a) Schematic drawing of the experimental setup for the determination of the maximum bandwidth of the DHPCA-100. The total cable length in both parts was set to 2 m in accordance to the experimental setup of the STM. (b) Voltage curves for a test pulse with a time duration of $\approx$ 840 ns. The transimpedance of the amplifier was set to $10^4$ V/A. The voltage curve for the test pulse (black) is vertically offset by 1 V for clarity. The voltage curve after the transimpedance amplifier (red) shows a broadening of the fall and rise times.

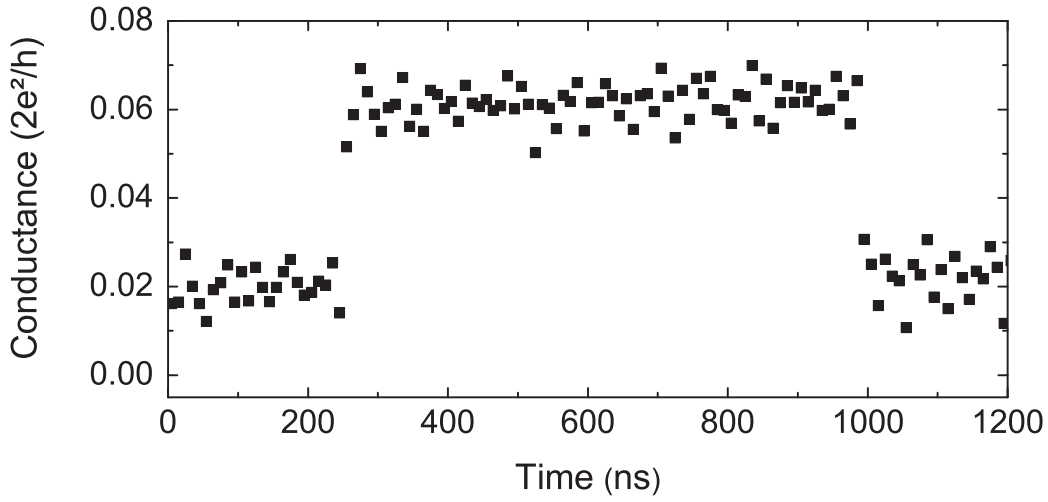


*Fig. 2.9:* Detailed time trace of a laterally fluctuating Ag adatom on Ag(111). Conductance levels of $\approx 0.06\,G_0$ and $\approx 0.02\,G_0$ correspond to the adatom residing at an hcp and fcc site, respectively. The time interval between two adjacent datapoints is 10 ns.

pulse of the generator. The total cable length in both parts was set to 2 m in accordance to the experimental setup of the STM. Figure 2.8b shows the test pulse (black, vertically offset by 1 V). The voltage curve after the transimpedance amplifier (red) shows a broadening of the fall and rise times. The fall time after the transimpedance amplifier until the output voltage is kept constant, $\Delta t_{f,1}$, is $\approx 30$ ns and the rise time, $\Delta t_{r,1}$, is $\approx 37$ ns. Although these values are in good agreement to the inverse of the upper cut-off frequency of $(30\,\mathrm{MHz})^{-1} = 33$ ns another definition of the fall and rises time is useful for the experiment. The under-/overshoot of the voltage is small compared to the huge drop of the voltage and therefore is not visible in real experimental data as shown later in Figure 2.9. Thus, we define the fall and rise times as the times until the output voltage has reached for the first time the value which is later kept constant. Using this definition fall and rise times of $\Delta t_{f,2} \approx 12$ ns and $\Delta t_{r,2} \approx 13$ ns are occurred. Additionally to the broadening of the fall and rise times a time delay between both signals of $\approx 5$ ns can be detected. Because the cable lengths in both parts are approximately the same the delay is based on the electronic of the transimpedance amplifier. However, the delay is constant and thus does not distort the measurement.

For the determination of the time resolution of the experimental setup of the STM we investigate conductance fluctuations which occur when a single Ag adatom reversibly switches between neighboring adsorption sites on Ag(111) as described later in Chapter 4. Figure 2.9 presents a detailed time trace of

such conductance traces acquired at a transimpedance of $10^4$ V/A. Conductance levels of $\approx 0.06\,G_0$ and $\approx 0.02\,G_0$ correspond to the adatom residing at hcp and fcc site, respectively. The time interval between two adjacent datapoints is 10 ns. The abrupt jump (drop) of the conductance without any datapoints between the two levels proves that the time resolution of our experimental setup is $\leq 10$ ns. Thus, we reach a time resolution of our STM which is by a factor of 1000 higher compared to the time resolution with conventional STM published so far ($10 - 100\,\mu$s) [1–3].

In this thesis fast time-resolved measurements were performed for the detailed investigation of laterally fluctuating Ag adatoms on Ag(111) in Chapter 4.

# 3. EVOLUTION OF UNOCCUPIED RESONANCE DURING THE SYNTHESIS OF A SILVER DIMER ON AG(111)

## *3.1 Introduction*

The electronic structure of adsorbed atoms (adatoms) or clusters of atoms on surfaces determines the coupling between adsorbate and substrate [97–100], the mutual interaction between the adatoms [9], magnetic properties [101], as well as their catalytic activity and selectivity [102,103]. The coupling between adatoms is particularly interesting since it plays a crucial role in nucleation and is thus at the base of the microscopic understanding of thin film growth on surfaces [104–106]. Typically, the mutual interaction comprises direct and indirect contributions. Direct interactions result from the overlap of atomic orbitals and are responsible for the bonding of dimers in vacuum. This type of interaction has been investigated for metal dimers in the gas phase and noble-gas matrices [107–109]. An exponential energy splitting of bonding and antibonding states with the atom–atom separation is characteristic for direct coupling. Indirect interactions may become important for adatoms on surfaces and they depend strongly on the electronic structure of the substrate. In particular, long-ranged and oscillatory coupling between two adatoms or adsorbed molecules is mediated by quasi-two-dimensional electronic continua [110–117].

The evolution of the electronic structure of clusters on surfaces with cluster dimensions and geometric shapes has been analyzed atom by atom. Examples are results from artificial gold chains [22], quantum confinement of one-dimensional electronic states to chains of copper atoms [23], unoccupied electronic resonances of silver clusters with various sizes and shapes [26], and the evolution of the Kondo effect of a single magnetic atom with the number of adjacent non-magnetic atoms in vertical [118] and lateral [29] hybridization geometries. In a recent study of Au dimers on NiAl(110) a splitting of the Au monomer resonance into bonding and antibonding states was reported as a function of the Au–Au separation [9]. The emerging picture, which may be inferred from this work, is that substrate-mediated adsorbate–adsorbate

interactions weaken the direct coupling between the adsorbates. In particular, it was found in Reference [9] that the splitting between bonding and antibonding states varies linearly with the reciprocal mutual Au distance, rather than exponentially as would be expected from a direct coupling in vacuum.

Here, in a combined experimental and theoretical study[1], we investigated the evolution of a Ag monomer $sp_z$ resonance, which shifts toward the Fermi level upon approaching a second Ag atom. The theoretical analysis indicated that, at not too large adatom–adatom distances, the interaction between the $sp_z$ electronic states on the surface is similar to the direct interaction between the two $sp_z$ orbitals in vacuum.

## 3.2 Experimental Details

Measurements were performed with a custom-built scanning tunneling microscope operated at 7 K and in ultrahigh vacuum with a base pressure of $10^{-9}$ Pa. The Ag(111) surface and chemically etched tungsten tips were cleaned by argon ion bombardment and annealing. Individual silver atoms were deposited onto the sample surface by controlled tip–surface contacts as previously described in Reference [91]. Using the tip of the microscope, silver dimers were fabricated by atom manipulation. Spectra of the differential conductance ($\mathrm{d}I/\mathrm{d}V$) were acquired by superimposing a sinusoidal voltage signal (root-mean-square amplitude 5 mV, frequency 4.7 kHz) onto the tunneling voltage and by measuring the current response with a lock-in amplifier. Prior to spectroscopy of monomers and dimers the tip status was monitored using spectra of the onset of the Ag(111) surface state band edge. To obtain sharp onsets of the surface state signal and to image single adatoms with nearly circular circumference the tip was controllably indented into the substrate. Due to this *in vacuo* treatment the tip apex was most likely covered with substrate material. All STM images were acquired in the constant current mode with the voltage applied to the sample. We divided the $\mathrm{d}I/\mathrm{d}V$ spectra by $I/V$ to reduce the influence of the voltage-dependent transmission of the tunneling barrier [119].

## 3.3 Results and Discussion

Figure 3.1(a) presents a sequence of constant-current STM images showing a single Ag adatom (top) on Ag(111), two Ag adatoms (middle) with a distance

[1] The theoretical analysis were performed by A. Franke and E. Pehlke, Institute of Theoretical Physics and Astrophysics (ITAP) of Kiel University.

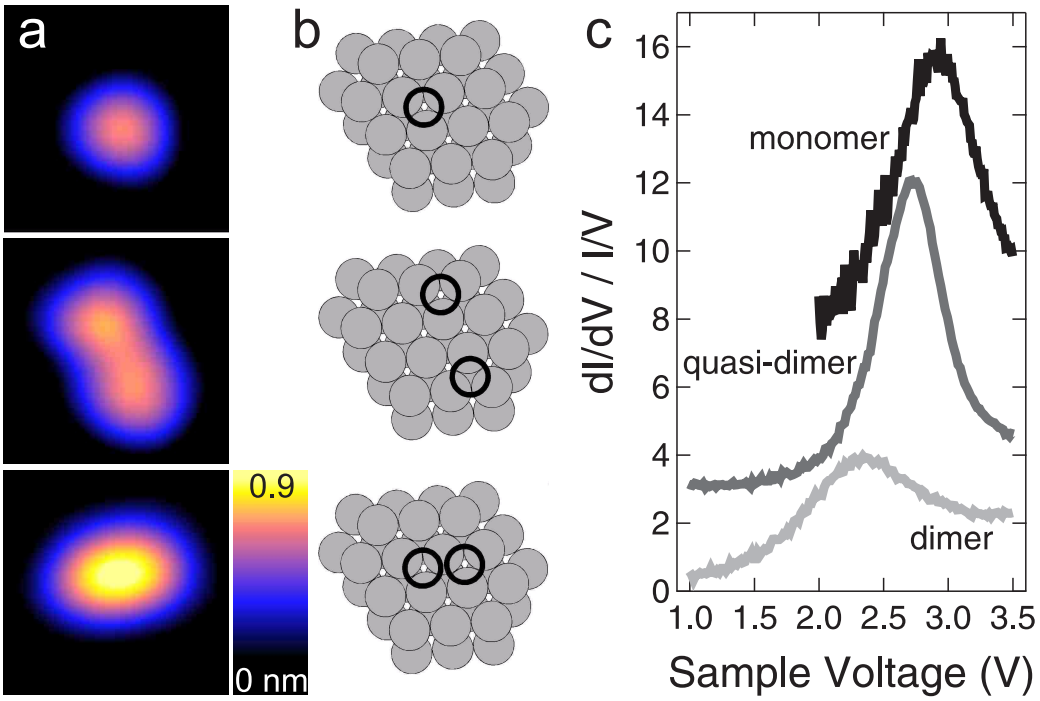


*Fig. 3.1:* (a) STM images of a single Ag adatom (top), two Ag adatoms with a mutual distance of 0.58 nm, and $Ag_2$ on Ag(111) (sample voltage: 0.1 V, tunnelling current: 0.1 nA, image size: 2.1 nm × 2.1 nm). (b) Schematics of adsorption sites of silver adatoms (black circles) on Ag(111) lattice (gray dots). (c) Spectra of $\mathrm{d}I/\mathrm{d}V/(I/V)$ acquired with the tip placed above the centre of the assemblies in (a). The spectrum of the quasi-dimer and of the monomer have been shifted vertically by 3 and 7, respectively. Prior to spectroscopy the tip–sample distance had been set at 3.5 V and 1 nA for all spectra.

of $\approx 0.58\,\mathrm{nm}$, and a silver dimer (bottom). Distances between adatoms of Ag–Ag assemblies were determined from maxima positions of cross-sectional profiles taken along the connecting line between the adatoms. Together with the orientation of the assembly with respect to high symmetry directions of the Ag(111) substrate, which was determined from dislocation lines on the surface, the extracted adatom–adatom distances agree with lattice site separations on Ag(111). The Ag dimer appears as a single entity in STM images and we assigned the nearest-neighbor distance of Ag(111) to the adatom–adatom distance of $Ag_2$. Our calculations indicated a slight preference of the Ag adatom to occupy the face-centered cubic (fcc) adsorption site to occupation of the metastable hexagonal close-packed (hcp) adsorption site, which is of the order of the accuracy of the calculation. We experienced that in the course of fabricating silver dimers individual Ag adatoms were also found to occupy hcp adsorption sites [see the middle STM image in Figure 3.1(a) and the corresponding sketch in Figure 3.1(b)]. Such assemblies occurred frequently for adatom distances smaller than 0.6 nm. In the following these assemblies are referred to as quasi-dimers. The schematics in Figure 3.1(b) illustrate adsorption sites of individual Ag adatoms (black circles) on the hosting Ag(111) lattice (gray dots) and the orientation of the quasi-dimer and the dimer with respect to the Ag(111) crystallographic directions. Figure 3.1(c) shows normalized $\mathrm{d}I/\mathrm{d}V$ spectra acquired on the center of the single Ag adatom (top), of a quasi-dimer (middle), and of the dimer (bottom). A gradual shift of the monomer-related peak from $\approx 2.9\,\mathrm{eV}$ via a resonance energy of $\approx 2.7\,\mathrm{eV}$ observed for the quasi-dimer to $\approx 2.3\,\mathrm{eV}$ for the dimer resonance binding energy was observed. The total shift of $\approx 0.6\,\mathrm{eV}$ toward the Fermi level was not induced by the electric field of the tip. Although the tip–surface distances may have differed for the spectra shown in Figure 3.1(c), it has been shown in References [120, 121] that for shifts of the order of 10 meV the tip–surface distance had to be varied by several Angstroms, which was not the case here.

Figure 3.2(a) summarizes the resonance energies measured for a variety of Ag adatom separations, $d_{\mathrm{Ag-Ag}}$. For $d_{\mathrm{Ag-Ag}} > 1\,\mathrm{nm}$ the shift of the resonance energy became too small to be resolved. For separations $d_{\mathrm{Ag-Ag}} < 1\,\mathrm{nm}$ a shift of the resonance energy became detectable and increased rapidly as $d_{\mathrm{Ag-Ag}}$ approached the nearest-neighbor distance of Ag(111). The solid line in Figure 3.2(a) is a fit to calculated data [Figure 3.2(b)], which has been extrapolated to larger Ag–Ag distances. The calculations are discussed below. For $d_{\mathrm{Ag-Ag}} > 2\,\mathrm{nm}$ the spectra at the center between two Ag adatoms were virtually identical with spectra of clean Ag(111) in the relevant voltage interval [26]. For this reason the data points for $d_{\mathrm{Ag-Ag}} > 2\,\mathrm{nm}$ in Figure 3.2 were acquired atop the individual adatoms.

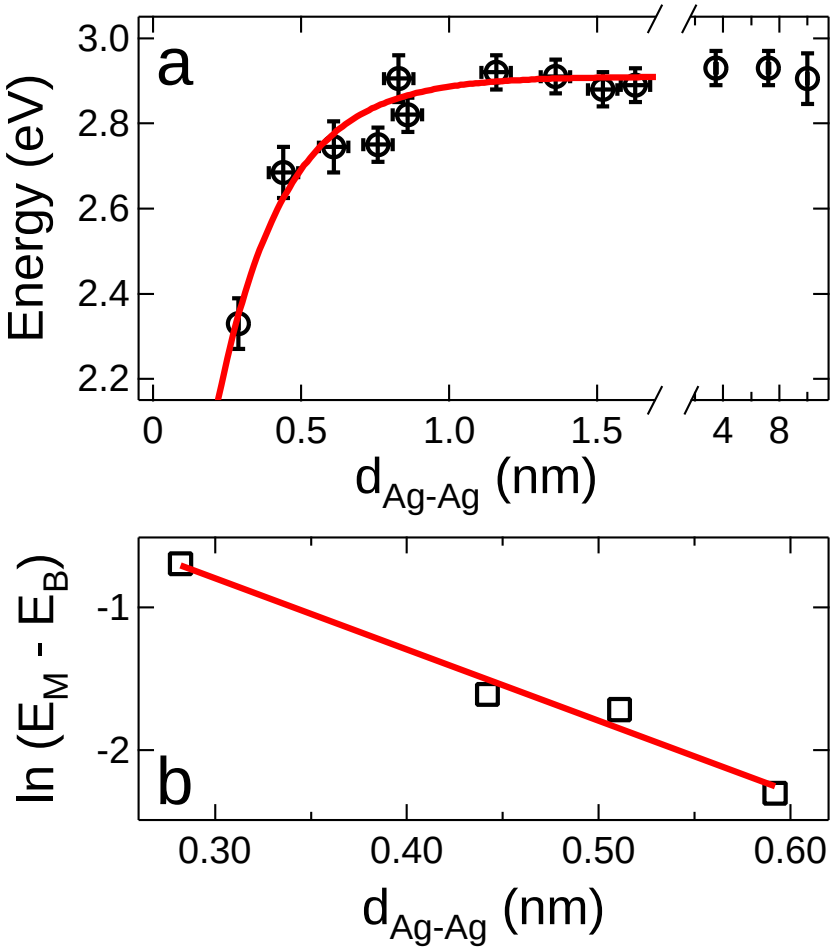


*Fig. 3.2:* (a) Energy of the unoccupied resonance as a function of the Ag adatom distance, $d_{\mathrm{Ag-Ag}}$. For distances larger than 2 nm the spectra were acquired atop the individual Ag adatoms while for smaller distances spectroscopy was performed with the tip positioned above the center of the assembly. The solid line is a fit to the calculated data in (b). (b) Logarithm of the calculated energy difference between monomer resonance (M) and bonding resonance (B) of an Ag–Ag assembly, $\ln(E_{\mathrm{M}} - E_{\mathrm{B}})$, plotted versus $d_{\mathrm{Ag-Ag}}$. The solid line is a linear fit to the data.

Using density functional theory as implemented in the Vienna *ab initio* Simulation Package (VASP) [122–125] we determined the electronic structure of silver dimers adsorbed on Ag(111) with increasing adatom–adatom separation. The generalized gradient approximation (GGA) PW91 by Perdew and Wang [126] was applied to the exchange correlation functional. The electron-ion interaction was treated within the framework of Blöchl's projector augmented wave (PAW) method [127]. The potentials for VASP were used from the database [128]. All configurations were modeled in a slab geometry comprising of 14 layers of Ag. Silver dimers with separations of 0.28, 0.44, 0.52, and 0.59 nm were modeled in a $(5\times4)$, $(6\times4)$, $(4\times4)$, and $(6\times4)$ surface unit cell, respectively. The surface Brillouin zone was sampled with 16, 9 and 6 $k$ points for the $(4\times4)$, $(5\times4)$, and $(6\times4)$ unit cells, respectively. The Kohn-Sham wave functions were expanded in a plane wave basis set with a 250 eV cutoff energy.

In order to identify the orbital composition of the experimentally observed unoccupied resonance, we have calculated the projected density of states (PDOS) with respect to atomic orbitals localized at the adatom sites. In case of the silver dimer with both atoms at neighboring fcc sites, the maximum of the resonance was found between 1.8 and 1.9 eV above the Fermi energy [26]. This resonance can clearly be observed in the $p_z$ PDOS [Figure 3.3(a)], while it is absent in the $s$ PDOS [Figure 3.3(b)]. From this we conclude a dominant $p_z$ character, with some $s$ admixture, of this resonance.

By projecting onto bonding and antibonding combinations of $p_z$ orbitals located at the two Ag atoms of the dimer, we identified the center of the bonding and antibonding $p_z$ resonance [Figure 3.3(c)]. From this we obtained the energy splitting between the bonding ($E_\mathrm{B}$) and the antibonding ($E_\mathrm{A}$) state, whose logarithm is plotted as a function of the mutual Ag atom distance in Figure 3.3(d). The results shown in Figure 3.3(d) are consistent with an exponential variation of $E_\mathrm{A}-E_\mathrm{B}$ within the calculated range of Ag adatom distances. In order to compare to experiment, we furthermore calculated the energy shift of the bonding resonance of the Ag adatom pair with respect to the energy of the monomer resonance ($E_\mathrm{M}$) [Figure 3.2(b)]. We found that the energy splitting between the bonding resonance with respect to the monomer resonance, $E_\mathrm{M}-E_\mathrm{B}$, quite accurately coincides with half the energy shift between the bonding and the antibonding states, $(E_\mathrm{A}-E_\mathrm{B})/2$. Thus, the splitting between bonding and antibonding states is approximately symmetric. The solid line in Figure 3.2(a) represents a linear fit to $\ln(E_\mathrm{M}-E_\mathrm{B})$ as a function of the Ag adatom separation $d_{\mathrm{Ag-Ag}}$, which has been extrapolated to larger separations. We conclude that both experimental and theoretical data are consistent with an exponential variation of the energy splitting with $d_{\mathrm{Ag-Ag}}$. However, due to computational limitations the range of Ag–Ag

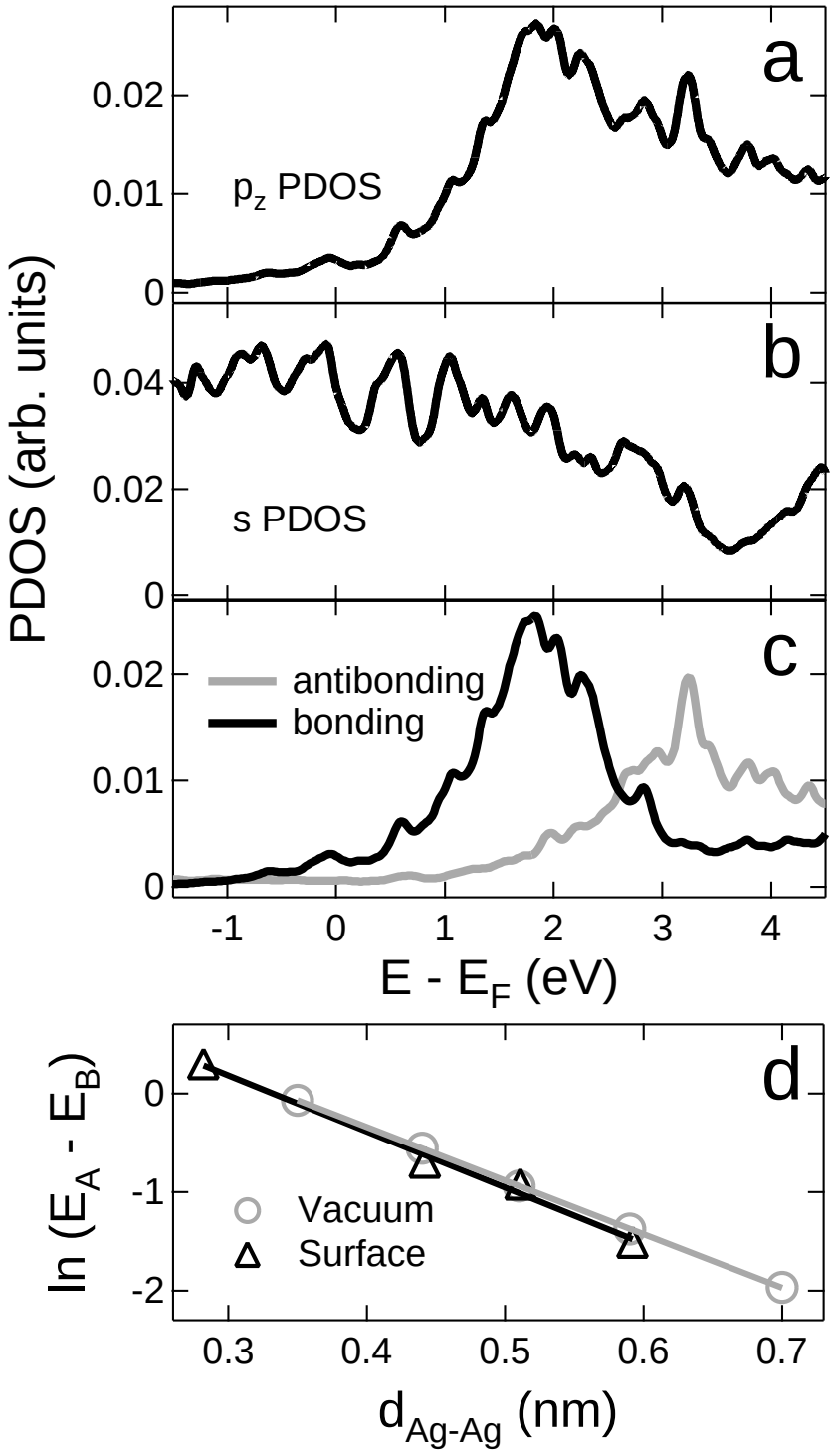


*Fig. 3.3:* (a) $p_z$ projected density of states (PDOS) and (b) $s$ PDOS for the silver dimer ($d_{\mathrm{Ag-Ag}} = 0.28\,\mathrm{nm}$, both adatoms at neighboring fcc sites). (c) Density of states projected onto bonding and antibonding $p_z$ orbitals located at the two atoms of the Ag dimer. (d) Logarithm of the Kohn-Sham energy splitting between bonding (B) and antibonding (A) resonances as a function of Ag–Ag distance for Ag assemblies on the Ag(111) surface (triangles) and for free Ag atom pairs (circles) in the supercell. The solid lines are linear fits to the data.

distances considered here for the two Ag adatoms on the Ag substrate is too narrow to reliably distinguish between an exponential and an algebraic $(1/d)$ [9] dependence of energy splitting on adatom separation.

For comparison we have calculated the energy splitting between the $5p_z$ bonding and antibonding orbitals of a Ag dimer in vacuum. The calculated splitting of the silver $5p_z$ bonding and antibonding orbitals varied exponentially with atom separation as expected [107, 109]. Surprisingly, as is evident from Figure 3.3(d), the energy splitting between bonding and antibonding states for the dimer in vacuum is similar to the splitting of the dimer adsorbed on the surface for the Ag–Ag distances considered in the *ab initio* calculations.

To further analyze the interaction between adatoms on a surface we resorted to a minimum tight-binding model, which is similar to the model reported in Reference [129]. For simplicity we did not consider a tight-binding model of the fcc crystal and its (111) surface, but we resorted to atoms with a single $s$ orbital forming a simple cubic lattice, and two adatoms adsorbed at on-top sites. We found a direct contribution, $2t$, to the energy splitting between bonding and antibonding states, which is due to direct adatom interaction. The parameter $t$ denotes the transfer integral for the two adatom states, and $2t$ is identical to the splitting occurring for the free dimer at the same adatom distance. Furthermore, there is a contribution to the splitting owing to the interaction via the substrate, $2\,\mathrm{Re}(G_{ab})\,|v|^2$, where $v$ denotes the next-neighbor transfer integral and $G_{ab}$ the matrix element of the Green's function of the substrate with respect to the adsorption sites. Calculations of such a matrix element of the Green's function for two next-neighbor sites on the Ag(111) surface yielded values of $\mathrm{Re}(G_{ab})(\varepsilon)$ varying between 0.05 and $0.15\,\mathrm{eV}^{-1}$ within the energy range of interest. For typical values of $|v|$ between 0.4 and 1 eV the simple model also predicts that the interaction via the substrate is distinctly smaller than the observed splitting. At large adatom separations we expect the substrate-mediated interaction to eventually dominate the direct interaction between the adatoms. In case of Ag atom pairs on Ag(111) this appears to occur at a separation which is too large for the splitting to be resolved in experiment.

In a previous investigation of Au dimers on NiAl(110) the splitting of bonding and antibonding Au dimer states was reported for varying Au-Au distances [9]. The authors of Reference [9] found that the variation of the splitting follows a $1/d_{\mathrm{Au-Au}}$ rather than an exponential law. This observation was argued to be due to the influence of the substrate electronic structure, which reduces the direct overlap of Au orbitals. In the case of Ag–Ag assemblies on Ag(111), however, the interaction between the individual Ag adatoms is similar to the one in vacuum [Figure 3.3(d)]. A tentative expla-

nation for this observation involves the electronic structures of the substrates. The Ag(111) surface exhibits an extended *sp* band gap of surface-projected bulk electronic states in the center of the surface Brillouin zone [130], while NiAl(110) does not [131–133]. Since the resonance energy of the Ag–Ag assemblies falls into the surface-projected *sp* band gap it is likely that the Ag(111) substrate electronic structure plays a less important role in mediating the interaction between the Ag adatoms. As a consequence, the Ag adatom assemblies on Ag(111) are subject to a substrate influence to a lesser extent than the Au adatom assemblies on NiAl(110). We suggest that the large direct interaction in case of Ag dimers on Ag(111) is also caused by the large extension of the *p* wave function, which dominates the resonance. This results in a slow decay of the transfer integral as a function of Ag–Ag distance.

## 3.4 Summary

The interaction between two Ag adatoms on Ag(111) gives rise to a shift of a $sp_z$ resonance toward the Fermi level with decreasing mutual adatom distances. The shift was modeled by density functional calculations and is similar to the shift calculated for a Ag dimer in vacuum. This observation indicates a weak net influence of the substrate on the Ag–Ag interaction, which may originate from the surface-projected *sp* band gap of the substrate. We suggest that adatom–adatom interactions on surfaces with band gaps in the relevant energy interval exhibit a similar behavior. As a further reason for the dominating direct interaction we suggest a weak decay of atomic orbitals participating in the interaction.

# 4. DIRECT OBSERVATION OF CONDUCTANCE FLUCTUATIONS OF A SINGLE-ATOM TUNNELING CONTACT

## *4.1 Introduction*

Local heating of atom-sized contacts is vividly discussed since it has profound influence on future atomic or molecular electronics [134]. Moreover, the measurement of effective junction temperatures provides insight into the balance between energy dissipation at the single atom or molecule and heat transfer into the contacting electrodes [135]. Measurements of effective temperatures, however, are difficult due to the lack of appropriate thermometers. Indirect probes for local heating effects have been reported by atomic force and scanning tunneling microscopy. The atomic force microscope was used to measure the force required to break molecule–electrode bonds [136]. Since the breakdown process is thermally activated, effective temperatures of the molecular junction were extracted as a function of the voltage applied to the junction. With STM conductance–distance curves were acquired on single $C_{60}$ molecules [137]. The width of the transition between tunneling and contact was used to extract an effective temperature. Another indirect probe for effective temperatures is the controlled decomposition of fullerene molecules, which were heated by elevated currents [138]. A more direct method to evaluate effective temperatures of nanometer-scaled junctions is the measurement of two-level fluctuations, which appear in the conductance of such contacts [139–142]. These two-level fluctuations occur when two stable atomic configurations exist and the contact switches between them by thermal activation. Time-resolved measurements of two-level conductance fluctuations with STM are rare. Agraït *et al.* [90] reported conductance switches of Au and Pb contacts resulting from atoms oscillating between tunneling and contact regimes. Stroscio *et al.* [1] investigated conductance fluctuations in the course of single-cobalt manipulation on Cu(111). In these experiments, the switching of Co adsorption sites between hexagonal close-packed (hcp) and face-centered cubic (fcc) sites was controlled by the tip–surface distance and by the tunneling voltage ($V$). While for $|V| \leq 5\,\mathrm{mV}$ an almost constant back-

ground of the switching rate was observed and explained in terms of voltage-independent quantum tunneling of the Co atom between hcp and fcc sites, a strong increase of the switching rate was reported for $5\,\mathrm{mV} \leq |V| \leq 10\,\mathrm{mV}$. This strong increase was interpreted in terms of a nonthermal population of Co vibration modes excited through inelastic electron tunneling.

In this chapter a study of lateral translation dynamics of a Ag atom adsorbed on Ag(111) with a time resolution of 10 ns and in an extended voltage range between 1 mV and 0.5 V is shown. Positioning the tip off the center of the adsorbed atom (adatom) at elevated tunneling conductances ($\approx 0.1\,\mathrm{G_0}$, $\mathrm{G_0} \approx 77.5\,\mu\mathrm{S}$: quantum of conductance) induces random transitions between fcc and hcp adsorption sites, which are related to two-level fluctuations of the tunneling conductance. The voltage dependence of these fluctuations was used to extract effective temperatures of the adatom and diffusion barrier heights in the presence of the tip. The effective temperature of the adatom depends on its position relative to the tip and reaches $\approx 20\,\mathrm{K}$ at the highest voltage applied. The barrier heights between adsorption sites are drastically lowered due to the presence of the tip and reach several millivolts only.

## 4.2 Experimental Details

Single silver atoms were deposited onto the surface by controlled tip–surface contacts [91]. To acquire time-resolved conductance fluctuations a transimpedance amplifier (FEMTO DHPCA-100) was used with a 3 dB cut-off frequency of 30 MHz at 100 pF, which is the capacitance of the shielded cable carrying the tunneling current from the tip of the microscope to the amplifier. The experimental setup allows a time resolution of less than 10 ns.

## 4.3 Results and Discussion

Figure 4.1 illustrates the experimental conditions, at which conductance fluctuations were observed. In Figure 4.1(a) the STM image shows a single Ag adatom on Ag(111), which according to calculations occupies fcc substrate sites [26]. The cross indicates the lateral position of the tip above the surface, which is $\approx 1\,\text{Å}$ off the adatom center. Placing the tip exactly atop of the adatom did not lead to conductance fluctuations, which indicates that a finite lateral force component is required to move the adatom. The vertical tip position likewise plays a role for the observation of conductance fluctuations as illustrated in Figure 4.1(b), which shows the evolution of the conductance, $G$, as a function of the tip displacement, $\Delta z$. The characteristics of such conductance traces have been discussed in Reference [143]. Here, we use

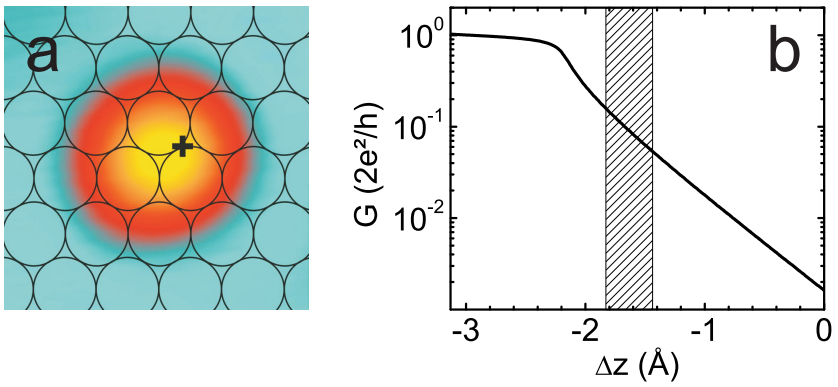


*Fig. 4.1:* (a) Constant-current STM image of a single Ag atom adsorbed on Ag(111) along with indicated surface lattice (black circles). The cross shows the lateral tip position during time-resolved measurements of the adatom translations (1.4 nm × 1.4 nm, 0.1 V, 0.1 nA). (b) Conductance ($G$) versus tip displacement ($\Delta z$) acquired at the center of the adatom. The conductance curve comprises tunneling ($0 > \Delta z > -2$ Å), transition from tunneling to contact ($-2$ Å $> \Delta z > -2.2$ Å), and contact ($\Delta z < -2.2$ Å). Zero displacement corresponds to feedback loop parameters of 0.1 V and 10 nA. The hatched area shows the conductance range where two-level fluctuations were probed.

the conductance curve to show that conductance fluctuations started to occur for conductances exceeding $0.05\,G_0$, which still belong to the tunneling regime. This conductance is in good agreement with the threshold conductance, which was reported to move single Ag adatoms on Ag(111) using the tip of a scanning tunneling microscope [57]. For different adsorbate–substrate combinations the tunnel parameters for tip-assisted single-atom or single-molecule translations vary [13, 144]. In particular, the conductance fluctuations to be discussed next, are most likely due to lateral motions of the adatom. Vertical adatom movements would lead to closing and opening of the tunneling gap between tip and adatom and would involve single-adatom conductances of $\approx 1\,G_0$ [91]. As soon as the tip–adatom spacing was small enough to observe two-level fluctuations of the conductance with a similar mean time spent in each level, then the tip–surface distance was frozen by opening the STM feedback loop and the sample voltage was varied to explore the voltage-dependence of the fluctuation rate.

Typical time-resolved two-level fluctuations are presented in Figure 4.3. At the indicated voltages the conductance displays fluctuations between $\approx 0.08\,G_0$ and $\approx 0.15\,G_0$. The high conductance level corresponds to the adatom residing at the hcp site, since in this case the tip–adatom distance is

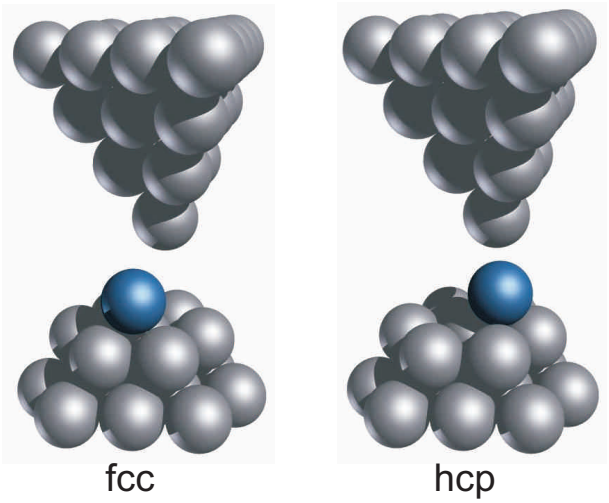


*Fig. 4.2:* Sketch of the tunneling junctions used in the time-resolved conductance measurements. The Ag adatom hops between fcc and hcp site and thus modifies the junction conductance.

smaller than for the adatom residing at the fcc site as indicated in Figure 4.2. Figure 4.3 shows two trends with increasing voltage: first, the fluctuation rate increases and, second, the average occupation time of the hcp site ($\bar{\tau}_{\mathrm{hcp}}$) decreases in favor of an increasing average occupation time of the fcc site ($\bar{\tau}_{\mathrm{fcc}}$). For instance, at 75 mV, $\bar{\tau}_{\mathrm{hcp}} > \bar{\tau}_{\mathrm{fcc}}$, while at 100 mV, $\bar{\tau}_{\mathrm{hcp}} \approx \bar{\tau}_{\mathrm{fcc}}$, and at 150 mV, $\bar{\tau}_{\mathrm{hcp}} < \bar{\tau}_{\mathrm{fcc}}$. Consequently, for small voltages the adatom preferentially occupies the hcp site, which is closer to the tip apex. We note that for $|V| < 1$ mV two-level fluctuations occurred with a rate of less than $0.2\,\mathrm{s}^{-1}$, which is most likely due to Ag adatom tunneling between hcp and fcc sites. For Co atoms on Cu(111) a tunneling rate between 1 and $20\,\mathrm{s}^{-1}$ was reported [1].

Two-level conductance fluctuations are random in nature and a model that describes these fluctuations must take the stochastic behavior into account. In particular, the question arises how to define a reasonable mean residence time for hcp and fcc sites based on the measured time series of random conductance fluctuations. Conductance fluctuations have previously been considered as Markov processes [1], in which two subsequent events occur independently from each other. The probability, $P_i$, that a fluctuation to level $i$ occurs within the time $t$ is given by

$$P_i(t) = R_i \exp(-R_i t), \tag{4.1}$$

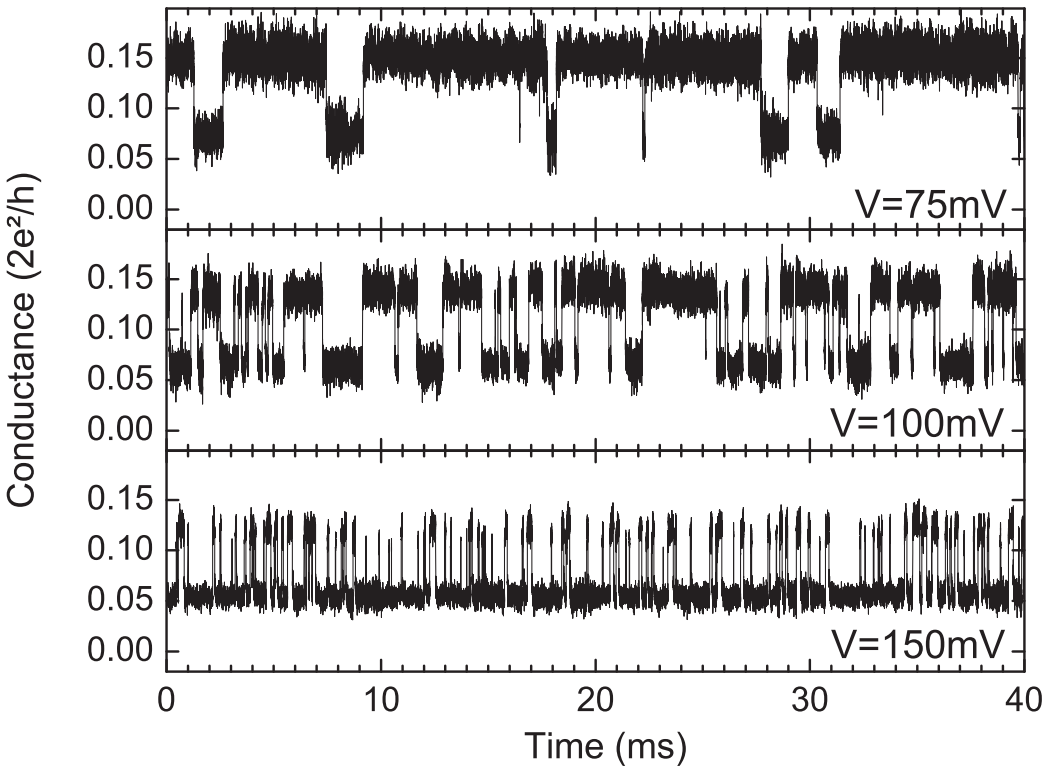


*Fig. 4.3:* Two-level fluctuations of the conductance at the indicated voltages and acquired with the tip–adatom configuration shown in Figure 4.1(a). The feedback loop was opened at $G \approx 0.08\,\mathrm{G_0}$. Conductance levels of $\approx 0.15\,\mathrm{G_0}$ and $\approx 0.08\,\mathrm{G_0}$ correspond to the adatom residing at an hcp and fcc site, respectively.

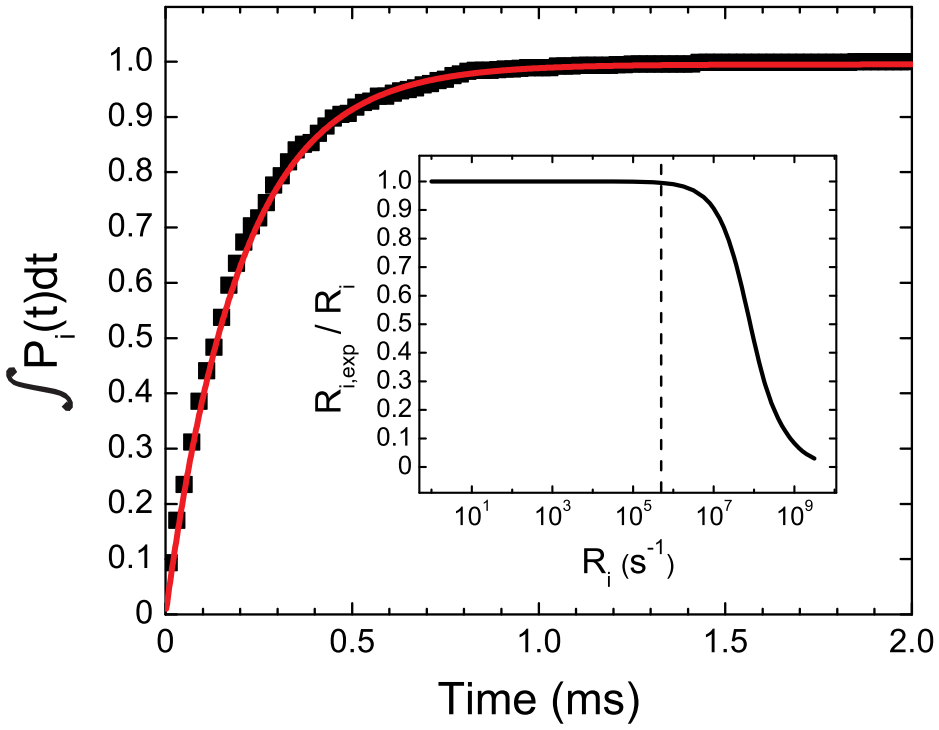


*Fig. 4.4:* Integrated probability for a typical time series of conductance fluctuations at the fcc adsorption site measured at a sample voltage of $-0.3\,\mathrm{V}$. Experimental data appear as symbols while the line represents a fit to experimental data according to $\int_0^t P_i(\tilde{t})\mathrm{d}\tilde{t}$ with $P_i$ from Equation (4.1) Inset: Ratio of the mean fluctuation rate $R_{i,\mathrm{exp}} = \bar{\tau}_i^{-1}$ as extracted from the arithmetic mean residence time $\bar{\tau}_i$ and the expected transition rate $R_i$ [Equation (4.1)] as a function of $R_i$. The dashed line denotes the maximum mean fluctuation rate of $5 \times 10^5\,\mathrm{s}^{-1}$ as measured in the experiments.

where $R_i$ denotes the sought-after mean transition rate (see Appendix A). To corroborate that the measured conductance fluctuations may indeed be described by a Markov process, Figure 4.4 shows the good agreement between experimental (symbols) and calculated (line) integrated probability, $\int_0^t P_i(\tilde{t})\mathrm{d}\tilde{t}$. The experimental data have been obtained by statistically evaluating residence times of a given time series, *i. e.*, by calculating the probability with which residence times, $\tau_i$, lower than a given time, $t$, occur. To approximate the mean transition rate we resorted to the reciprocal mean residence time, *i. e.*, $R_{i,\mathrm{exp}} = \bar{\tau}_i^{-1}$, where $\bar{\tau}_i$ denotes the arithmetic mean residence time as calculated from measured times series of conductance fluctuations. However, due to the finite time resolution of the experimental setup, arbitrarily small residence times cannot be resolved and thus do not enter in the calculation of $\bar{\tau}_i$. As a consequence, the mean residence time $\bar{\tau}_i$ contains a small systematic error and $R_{i,\mathrm{exp}}$ deviates from the ideal $R_i$. To estimate this deviation, the inset in Figure 4.4 shows the ratio $R_{i,\mathrm{exp}}/R_i$ as a function of $R_i$. For fluctuation rates $R_i$ below $5 \times 10^5\,\mathrm{s}^{-1}$, which is the highest rate observed in the experiments reported here, the deviation of $R_{i,\mathrm{exp}}$ from $R_i$ is less than 0.5 %. As a consequence, the arithmetic mean residence time describes the real mean residence time very well.

To describe the experimental observations, we assume that the conductance fluctuations are induced by lateral translations of the adatom, which may be facilitated by a lowering of the diffusion barrier height between adjacent adsorption sites owing to the presence of the tip [1]. These translations are most likely due to adatom vibrations excited by inelastically tunneling electrons. An appropriate way to describe the dynamics of such lateral adatom translations is to use an Arrhenius-type expression for the average time of the adatom in adsorption site $i$ ($i = \mathrm{hcp}, \mathrm{fcc}$):

$$\bar{\tau}_i = \tau_{0,i} \exp\left(\frac{E_i - \zeta_i V}{\mathrm{k_B} T_{\mathrm{eff},i}}\right), \tag{4.2}$$

where $\tau_{0,i}$ is the attempt time, $E_i$ the diffusion barrier height separating fcc and hcp sites in the presence of the tip, $\zeta_i$ is the electromigration parameter, which takes a possible asymmetry for positive and negative voltages into account [140, 141], $\mathrm{k_B}$ is Boltzmann's constant, and $T_{\mathrm{eff},i}$ is the effective temperature of the adatom. The voltage dependence of the effective temperature has been derived by Todorov [145, 146], who explicitly considered heat transfer into the electrodes:

$$T_{\mathrm{eff},i} = \sqrt[4]{T_0^4 + \alpha_i^4 V^2}. \tag{4.3}$$

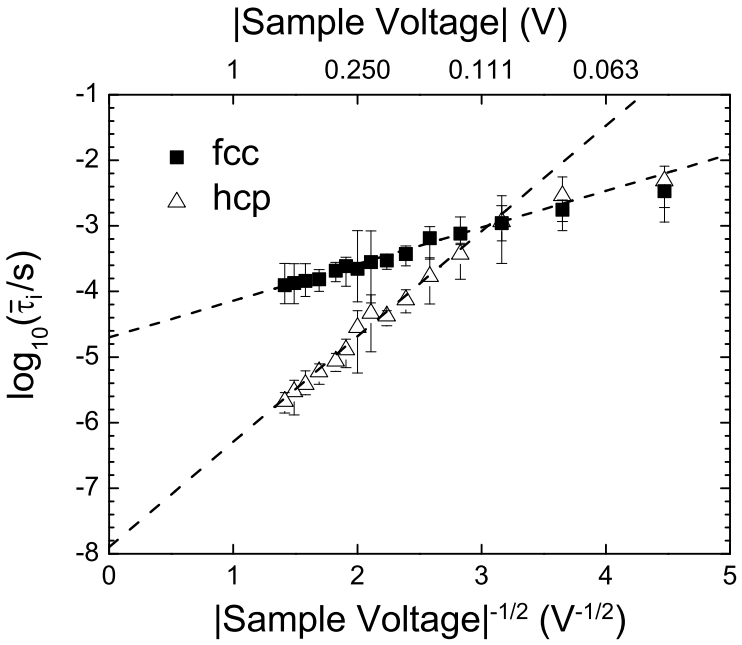


*Fig. 4.5:* Logarithm of the residence time $\bar{\tau}_i$ ($i$ = hcp: △, $i$ = fcc: ■) as a function of $|V|^{-1/2}$ for a representative fluctuation measurement. Dashed lines are fits to data for $|V| > 0.1\,\mathrm{V}$ according to Equations (4.2), (4.3).

Here, $T_0$ denotes the ambient temperature and $\alpha_i$ describes the dependence of $T_{\mathrm{eff},i}$ on the voltage. This expression for the effective temperature is consistent with several experimental results [136, 147, 148].

An alternative description of random telegraph noise of the conductance is based on vibrational heating [16, 149–151]. Within this description the atom overcomes the potential barrier separating adjacent adsorption sites by receiving vibrational energy from inelastically tunneling electrons. Energy is dissipated by decay of vibrational excitations into electron-hole pairs and phonons of the substrate. According to Reference [152] the fluctuation rate reads

$$R_i \approx m_i \Gamma_\uparrow \exp\left(-\frac{\tilde{E}_i}{k_\mathrm{B} T_v}\right). \tag{4.4}$$

Here, $\tilde{E}_i = (m_i - 1)\hbar\Omega$ with $\hbar\Omega$ the vibrational energy, $m_i$ is the number of vibrational levels in the potential well with spacing $\hbar\Omega$ and $\Gamma_{\uparrow(\downarrow)}$ is the vibrational excitation (deexcitation) rate between adjacent vibration levels of the harmonic oscillator potential. At vanishing voltages the excitation and deexcitation rates are balanced, which yields a vibrational motion that is in thermal equilibrium with the substrate. Atom translations are driven only

by thermal fluctuations and are spontaneous with a vanishing rate at low temperatures. If a voltage is applied between sample and tip the excitation rate increases and a vibrational temperature

$$T_v = \frac{\hbar\Omega}{k_\mathrm{B}\ln(\Gamma_\uparrow/\Gamma_\downarrow)} \tag{4.5}$$

will be higher than the substrate temperature. This leads to a characteristic power-law dependence of the transfer rate with applied voltage or current as derived in Reference [152]. Both features, the power-law dependence as well as the thermally activated regime, have been observed experimentally [1, 2, 66].

Both models have been applied to analyze our time-resolved fluctuation data. In principle the expected power-law dependence should be observed as a linear curve in a double-logarithmic plot of the mean time as a function of sample voltage. However, mean residence times obtained here showed a non-linear behavior in the double-logarithmic plot which indicated that the vibrational heating model is less appropriate in describing the experimental data. By assuming the validity of the first model, better results were obtained as shown below.

By performing experiments with positive and negative voltages, we found no significant influence of the voltage polarity on the mean occupation times, which indicated a small electromigration parameter. Indeed, fits to experimental data presented in Figure 4.5 worsened appreciably for $|\zeta_i| > 0.005\,\mathrm{eV/V}$. As a consequence, $\zeta_i$ was neglected in the subsequent analysis.

In Figure 4.5 the logarithms of the average residence times at fcc (squares) and hcp (triangles) sites are plotted as a function of the sample voltage. While for $|V| < 0.1\,\mathrm{V}$ these times are similar, for $|V| > 0.1\,\mathrm{V}$ the average time the adatom resides at the hcp site becomes lower than the average time at the fcc site. The overall evolution of the average occupation time with the voltage is well described by Equations (4.2) and (4.3). The dashed lines in Figure 4.5 are fits to experimental data according to these equations with $T_{\mathrm{eff},i} = \alpha_i\sqrt{|V|}$ for $|V| > 0.1\,\mathrm{V}$ (hcp) and $|V| > 0.15\,\mathrm{V}$ (fcc). For these voltages the term $T_0^4$ in Equation (4.3) may be neglected compared to $\alpha_i^4 V^2$. Deviations of the fits from experimental data were observed for $|V| < 0.1\,\mathrm{V}$, which can be explained by the ambient temperature, $T_0$, which becomes more important for smaller voltages. Averaging the intersections of the fits with the ordinate for all investigated adatoms, we obtained that $\tau_{0,\mathrm{fcc}}$ ($\tau_{0,\mathrm{hcp}}$) varied between $10^{-4.8}$ and $10^{-3.8}\,\mathrm{s}$ ($10^{-8.2}$ and $10^{-6.5}\,\mathrm{s}$). These values are remarkably high compared to typical attempt times reported for self-diffusion of Ag adatoms on Ag(111), which range between $10^{-12}$ and $10^{-11}\,\mathrm{s}$ [106]. However,

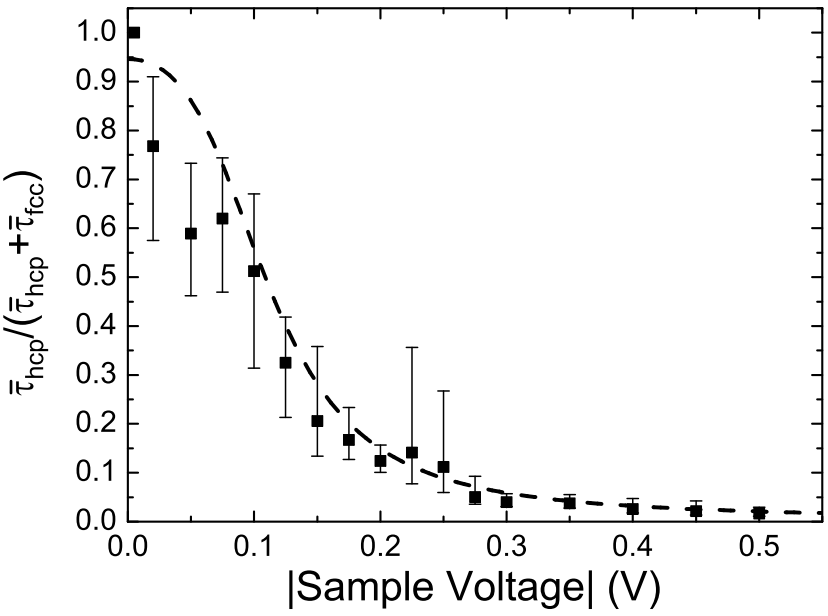


*Fig. 4.6:* Duty cycle for the adatom of Figure 4.4 as a function of the voltage. The dashed line depicts simulated data based on Equations (4.2), (4.3) and fit parameters summarized in Table 4.1.

Boisvert *et al.* [153] showed that the attempt time depends on the diffusion barrier height, which separates the adjacent adsorption sites. In particular, with decreasing barrier height the attempt time may increase by several orders of magnitude. High values of the attempt time have been predicted for CO on Cu(110) by helium atom scattering [154] and then confirmed by STM experiments [155]. Tunneling from thermally excited states of CO has been suggested to be the reason for extraordinarily high attempt times for CO diffusion on Cu(111) [61]. A theoretical treatment of diffusion processes on metal surfaces [156] demonstrated that neglecting adsorbate–adsorbate interactions may be at the origin of diffusion prefactor anomalies that have been extracted from nucleation experiments [157–159]. As we will show below, the presence of the tip and its attractive interaction with the adatom lowers diffusion barrier heights appreciably and thus may be the reason for the high attempt times.

The fit of experimental residence times has been performed by neglecting the ambient temperature, $T_0$, and led to the attempt times $\tau_{0,i}$ and the slopes $E_i/\alpha_i$ of the dashed lines in the Arrhenius-type plot of Figure 4.5. To determine the diffusion barrier heights $E_i$ and the parameters $\alpha_i$, the so-called duty cycle, $\bar{\tau}_{\mathrm{hcp}}/(\bar{\tau}_{\mathrm{hcp}} + \bar{\tau}_{\mathrm{fcc}})$ [140], was fitted using Equations (4.2), (4.3) without neglecting $T_0$. Figure 4.6 shows the evolution of the duty cy-

| Adatom | Polarity | $i$ | $\log(\tau_{0,i}/\mathrm{s})$ | $\mathrm{E}_i$ (meV) | $\alpha_i$ ($\mathrm{K}/\sqrt{\mathrm{V}}$) |
|---|---|---|---|---|---|
| 1 | + | fcc | −4.8 | 1 | 20.5 |
| | | hcp | −8.2 | 11.3 | 37.1 |
| 2 | − | fcc | −4.7 | 1.8 | 19.9 |
| | | hcp | −7.9 | 8.1 | 25.4 |
| 3 | − | fcc | −3.8 | 1.4 | 19.9 |
| | | hcp | −6.5 | 6.6 | 30.1 |

*Tab. 4.1:* Summary of fit parameters obtained from two-level fluctuations of three adatoms. Adatom 1 was analyzed at positive sample voltage, while Adatoms 2 and 3 were investigated at negative voltages.

cle as a function of the sample voltage. For high voltages, it approaches zero, which means that the hcp site is visited very briefly by the adatom and that the fcc site is preferentially occupied. Starting from $|V| \approx 0.1\,\mathrm{V}$, where $\bar{\tau}_{\mathrm{hcp}}/(\bar{\tau}_{\mathrm{hcp}} + \bar{\tau}_{\mathrm{fcc}}) \approx 50\,\%$, this trend is inversed for $|V| < 0.1\,\mathrm{V}$ and the hcp site becomes the preferred site, *i. e.*, the adatom is located near the tip apex. For nearly zero voltages the duty cycle reaches values close to 100 % reflecting the propensity of the adatom to stay in the vicinity of the tip apex. This observation is in agreement with molecular-dynamics simulations of tip-induced lateral atom manipulation at zero voltage [160]. In the absence of an applied voltage between tip and sample Yildirim *et al.* [160] showed that Ag (Cu) adatoms on Ag(111) [Cu(111)] follow the lateral trajectory of the tip apex. Using Equations (4.2) and (4.3) the behavior of the duty cycle was simulated (dashed line in Figure 4.6). With $\zeta_i = 0$, $T_0 = 7\,\mathrm{K}$ and the ratio $E_i/\alpha_i$ extracted from the slopes of the fits in Figure 4.5, only two fit parameters were left to describe the voltage dependence of the duty cycle. In Table 4.1 the fit parameters obtained for three investigated atoms are compared.

Remarkably, the barrier height between the adsorption sites is several millivolts only, which is much less than the reported diffusion barrier height for Ag adatoms on Ag(111) ($\approx 100\,\mathrm{meV}$) [106]. Most likely, the observed lowering of the barrier height is due to the presence of the tip, which has been already proposed in Reference [1]. Adatom translations in the combined potential of tip and surface has also been reported in Reference [161]. If the tip is positioned above a bridge position between hcp and fcc sites [Figure 4.1(a)] then the barrier height is substantially lowered owing to the superimposed tip potential [1]. As a consequence of strongly lowered energy

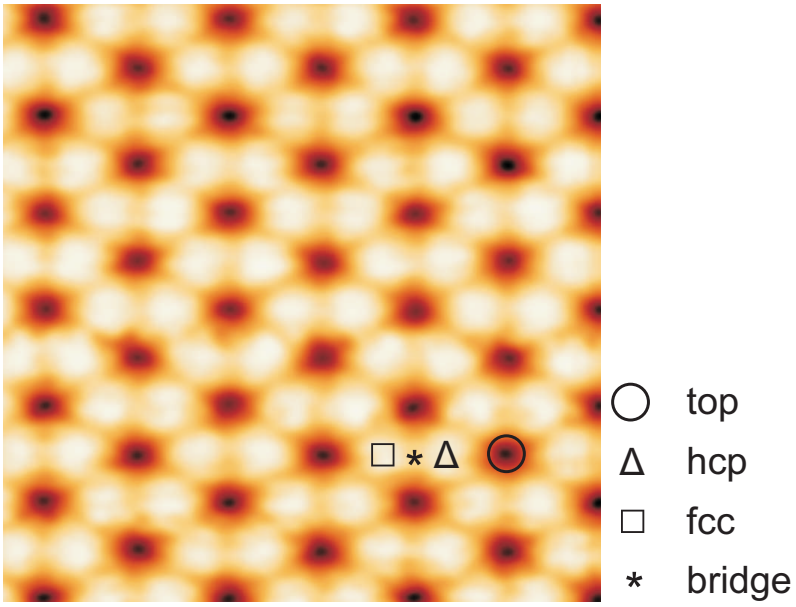


*Fig. 4.7:* (color online) Constant-current STM image of Ag(111), which was obtained by dragging a single Ag adatom. Dark areas correspond to top (circle) and bridge (asterisk) sites, while bright areas are fcc and hcp sites (square and triangle) (1.7 nm × 1.7 nm, 0.1 V, 2 $\mu$A).

barrier heights an extraordinary imaging mode with atomic resolution is feasible. The STM image in Figure 4.7 was acquired by dragging a Ag adatom with the scanning tip. During the measurement the adatom follows the tip by hopping from fcc to hcp sites. Similar tip-induced adatom translations have been reported for, *e. g.*, quantum corral construction using single atoms [57] and single-atom manipulation on vicinal surfaces [14]. Bright areas in Figure 4.7 correspond to fcc and hcp sites, where the adatom prefers to stay close to the tip at the chosen tunneling parameters (0.1 V, 2 $\mu$A). Dark areas monitor sites, which for the adatom are energetically not favorable (bridge and top sites) and which thus lead to an increase of the tip–adatom distance. In contrast to a similarly acquired STM image using a dragged Co adatom on Cu(111) where Cu(111) fcc sites appeared larger than hcp sites [1], fcc and hcp sites appear with virtually identical lateral dimensions on Ag(111) when imaged with a dragged Ag adatom. In an additional experiment, which is not discussed in detail here, we imaged a Cu(111) surface with a dragged Cu adatom and obtained a similar difference in the lateral dimensions of fcc and hcp sites as observed for Co on Cu(111) [1]. These observations may tentatively be explained on the basis of different adsorption energies in fcc and hcp sites for Cu(111) and Ag(111). The experimental observations on

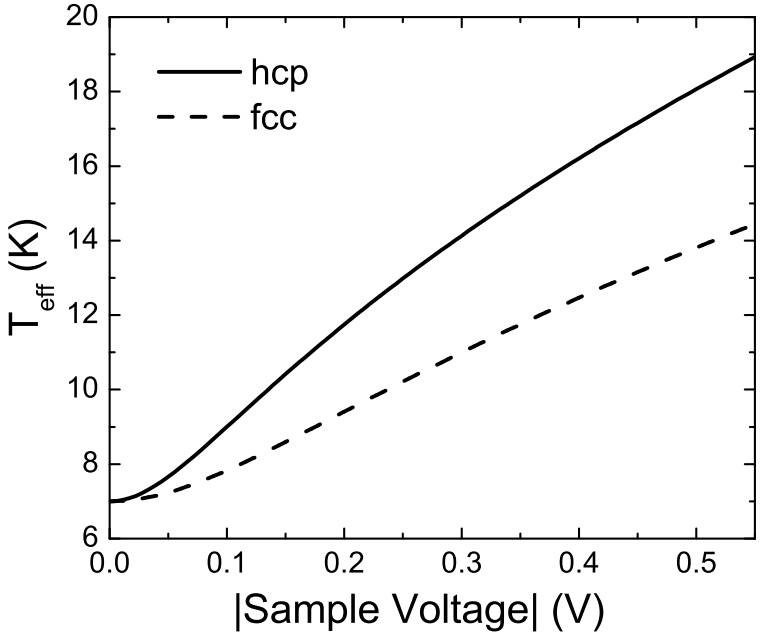


*Fig. 4.8:* Simulated effective temperatures of Ag adatom residing at hcp (solid line) and fcc (dashed line) sites of Ag(111). Calculations are based on Equation (4.3) and fit parameters for Adatom 2 (Table 4.1).

Cu(111) are compatible with a higher adsorption energy at the fcc than at the hcp site. In this case, the tip has to be close to the hcp site until the deformation of the hcp potential due to the tip is strong enough to make the adatom hop from the fcc to the hcp site. In contrast, approaching an fcc site a slight deformation of the fcc adsorption potential is necessary to drag the adatom from the hcp to the fcc site. Consequently, hcp sites appear with smaller lateral dimensions than fcc sites on Cu(111). For Ag(111) the difference between fcc and hcp adsorption potentials appears to be marginal, which results in the observed essentially identical dimension of fcc and hcp sites during imaging.

According to Table 4.1, for all investigated adatoms the barrier heights $E_{\mathrm{fcc}}$ and $E_{\mathrm{hcp}}$ differ by factors of 5 to 10. In particular, the energy needed to induce a transition from fcc to hcp is smaller than for the inverse transition. This observation may be understood by the presence of the tip, which in the experiments is positioned closer to the hcp than to the fcc site. According to a theoretical investigation, the adatom exhibits the propensity to stay close to the tip apex atom at zero voltage [160], which is in good agreement with a duty cycle of $\approx 100\,\%$ at very low voltages (Figure 4.6). Higher voltages provide higher energies to the tunneling electrons, which excite adatom

translations to the adjacent fcc site. Despite these translations the adatom prefers to stay close to the tip, which explains the different barrier heights. This phenomenon is closely related to the different heating of the adatom in hcp and fcc sites. According to Table 4.1, the parameter $\alpha_i$ is always higher for hcp than for fcc sites, which is due to the closer proximity of the adatom to the tip at the hcp site, which in turn is related to a higher current across the adatom. By simulating effective temperatures of Ag adatoms according to Equation (4.3) and to the obtained fitting parameters (Table 4.1), we found that local heating at the hcp site is more pronounced than at the fcc site (Figure 4.8). At 0.5 V, for instance, the effective temperature of the adatom at the hcp site is $\approx 18$ K, while it is $\approx 14$ K at the fcc site. Compared to effective temperatures of several hundreds of Kelvin reported for single-molecule junctions [136–138, 162], the adatom effective temperatures are low. A possible reason for this observation may be the low decay rate of molecule vibrations due to an inefficient coupling with the phonon modes of the electrodes [163]. A low decay rate can result from a mismatch of vibrational density of states of the molecule and the electrodes. For instance, 174 out of a total of 180 vibration modes of $C_{60}$ exhibit energies exceeding 25 meV and are thus higher than typical metal phonon energies [164]. In contrast, the single metal adatom has vibrational energies [165] that match the phonon energies of the electrodes. As a consequence, heat dissipation to the substrate is more effective for the adatom than for the molecule, which may explain the lower effective temperature of the adatom.

## 4.4 Summary

In summary, lateral translations of a Ag adatom on Ag(111) between adjacent adsorption sites were monitored by time-resolved two-level conductance fluctuations of the tunnel junction. The presence of the tip considerably lowers the diffusion barrier heights of the adatom and leads to different heating of the adatom depending on its relative position to the tip. Based on the voltage-dependence of conductance fluctuation rates, a means is provided to estimate the temperature in nanostructures through which elevated currents are passed.

# 5. CONTROLLED METALATION OF A SINGLE ADSORBED PHTHALOCYANINE

## *5.1 Introduction*

Phthalocyanine (Pc) molecules exhibit an intriguing variety of functional properties in biological and artificial systems [10]. Owing to their electronic and optical properties they are perceived as promising building blocks for nanotechnology [11]. The phthalocyanine macrocycle can host two hydrogen atoms ($H_2$Pc) or a metal ion (MPc) (Figures 5.1a, b). Metalation of $H_2$Pc and porphyrins on surfaces has been achieved for molecular layers at elevated temperatures by either evaporating metal atoms onto a previously formed molecular layer [166–174] or by depositing molecules onto a substrate which had been precovered with metal atoms [171, 175]. These approaches lead to a statistical distribution of MPc as observed with STM [170, 174]. Here, we demonstrate the controlled metalation of single $H_2$Pc molecules to AgPc using low-temperature STM. The reaction requires several steps, namely stepwise dehydrogenation of the inner macrocycle and subsequent implantation of a Ag ion. Direct metalation of $H_2$Pc was not observed in this type of experiment. In addition to the metalation process, hydrogen tautomerization of $H_2$Pc and hopping of a single hydrogen in the inner macrocycle of HPc were induced by electron injection from the STM tip. After each reaction step the electronic fingerprint of the product was determined by STS.

## *5.2 Experimental Details*

Experiments were performed with a home-made scanning tunneling microscope operated at 7 K and in ultrahigh vacuum with a base pressure of $10^{-9}$ Pa. Ag(111) surfaces and chemically etched tungsten tips were cleaned by argon ion bombardment and annealing. *In vacuo*, tips were indented into the substrate. Due to this treatment the tip apices were covered with silver from the substrate. $H_2$Pc (Figure 5.1a) and AgPc (Figure 5.1b) molecules were deposited from a heated tantalum crucible onto the surface at ambient temperature. To induce chemical reactions such as tautomerization or suc-

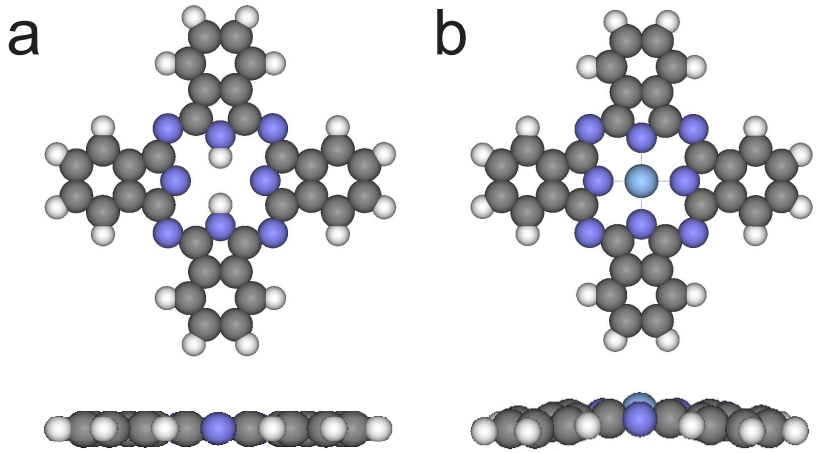


*Fig. 5.1:* Top and side views of optimized structures of (a) $H_2Pc$ and (b) AgPc in the gas phase. Calculations were performed using Gaussian 03 with the ROHF/LANL2DZ basis set.

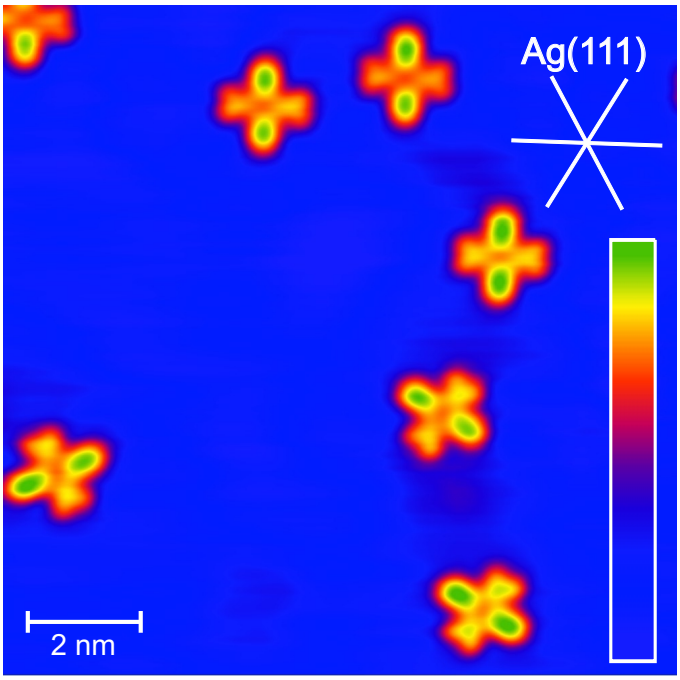


*Fig. 5.2:* Constant-current STM image of $H_2Pc$ adsorbed on Ag(111) (0.1 V, 0.1 nA). The close-packed directions of the Ag(111) are indicated by lines. The color scale covers apparent heights from 0 (blue) to 80 pm (green).

cessive dehydrogenation of the inner macrocycle of $H_2Pc$, rectangular voltage pulses were applied to the sample for sub-second time intervals with the feedback enabled. Spectroscopy of the differential conductance $dI/dV$, which is related to the local density of electronic states, was performed by adding a sinusoidal voltage ($20\,mV_{rms}$, 1.9 kHz) to the sample bias $V$ and measuring the first harmonic of the current response with a lock-in amplifier.

## 5.3 Results and Discussion

STM images of single $H_2Pc$ molecules adsorbed on a Ag(111) surface exhibit a two-fold symmetry (Figure 5.2). The ligands which are oriented along a crystallographic $\langle 1\bar{1}0\rangle$ direction appear lower. Density-functional calculations indicate that the reduced symmetry involves a saddle-shaped distortion of the molecule [176], similar to CoPc on Cu(111) [177]. Similar reduced symmetry was observed from some other adsorbed phthalocyanines (CuPc, CoPc, and FePc on Cu(111) [176, 178–181], SnPc on Ag(111) [69, 182]). Hopping of the hydrogen atoms at the pyrrolic nitrogen atoms of the inner macrocycle may be induced by positioning the tip over the center of the molecule and pulsing the sample voltage from 0.16 V above a threshold of 1.6 V (Figures 5.3a–c). The changes observed in STM images cannot be due to a rotation of the molecule as rotations to other orientations along equivalent $\langle 1\bar{1}0\rangle$ directions were never observed in repeated experiments despite the hexagonal symmetry of the surface layer. A similar tautomerization reaction has recently been reported for phthalocyanine and naphthalocyanine adsorbed on a variety of insulating films (NaCl, RbI, and Xe) [64].

A single hydrogen atom can be removed from the inner macrocycle by applying a voltage above a threshold of 3.0 V similar to the breaking of a C–H bond in a single acetylene molecule [80]. In STM images of dehydrogenated molecules (Figure 5.3d) the apparent height of one of the lobes which originally was higher is reduced below the height of the low lobes oriented along $\langle 1\bar{1}0\rangle$. This effect cannot be attributed to a change of the STM tip as the height of the other ligands is virtually not affected. It may be due to a N–Ag bond, which forms upon detaching the hydrogen atom. A related reduction of the apparent height was reported from Co and Sn phthalocyanine molecules whose peripheral hydrogen atoms were removed. According to first principles calculations bending of the ligands towards the metal substrate and the formation of bonds occurs in those cases [81, 83].

Hopping of the remaining central hydrogen between two opposite positions was induced by applying a voltage above a threshold of 2.5 V. The resulting molecule can be imaged at voltages below the threshold for induc-

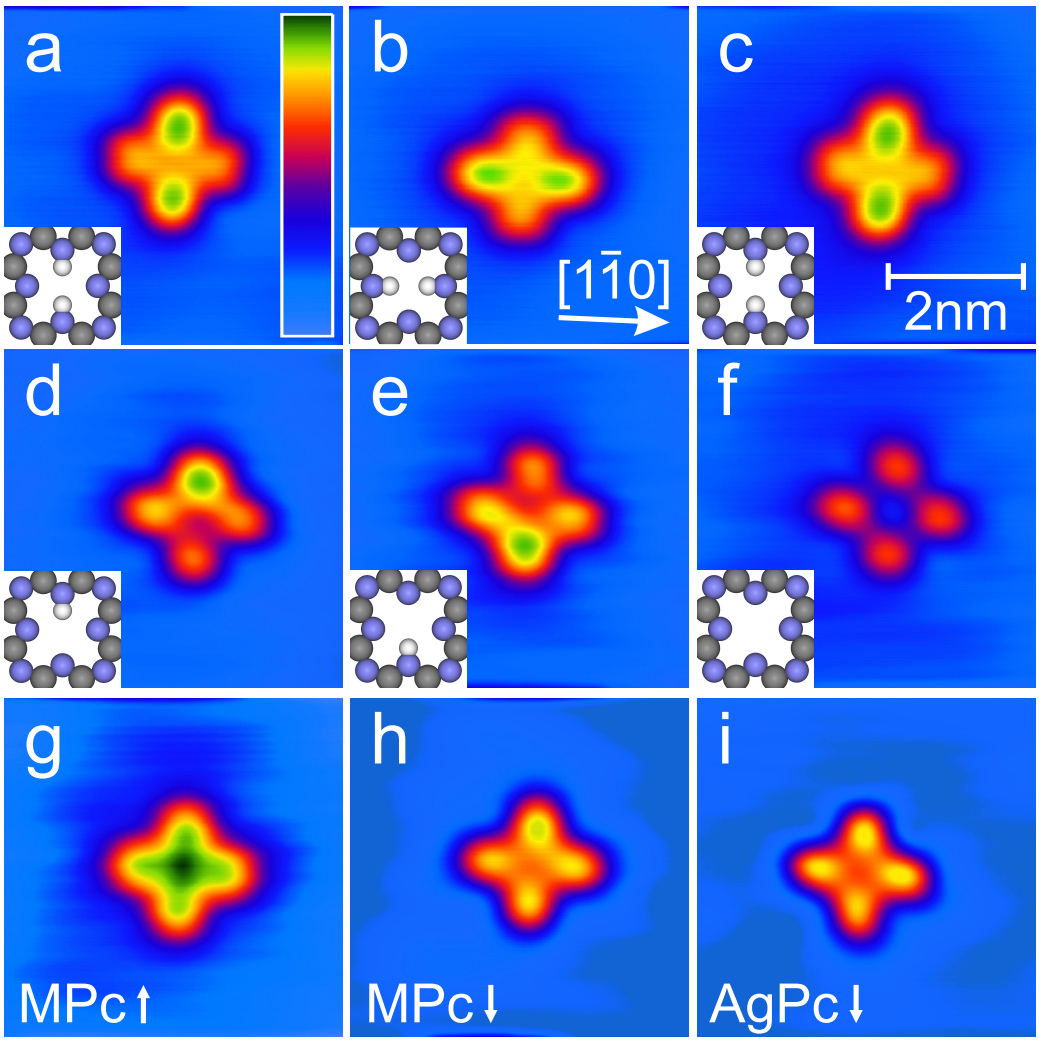


*Fig. 5.3:* (a–h) Constant-current STM images (0.1 nA, 0.1 V) of $H_2Pc$ and derived molecules. The color scale covers apparent heights from 0 (blue) to 77 pm (green). Schematics of the central part of the Pc molecules indicate the inferred molecular structures. (a–c) Tautomerization of $H_2Pc$, which was induced by voltage pulses of 1.6 V. (d,e) STM images of HPc obtained after removal of one pyrrolic hydrogen from $H_2Pc$ by a voltage pulse of 3.0 V. Hopping of the remaining pyrrolic hydrogen atom was induced by voltage pulses of 2.5 V. (f) Pc molecule fabricated by pulsing the voltage to 3.5 V. (g) After approaching the Ag tip to the center of the Pc, MPc↑ is formed. (h) A voltage pulse of 3.0 V leads to an interconversion of MPc↑ to MPc↓. By comparison with the image of AgPc on Ag(111) prepared by sublimation from a heated crucible (k) the molecule in (j) is identified as AgPc with the Ag atom between the surface and the molecular plane (AgPc↓).

ing hydrogen motion (Figures 5.3d, e). Switching of the hydrogen atom to any of the other two positions (at ligands along $\langle 1\bar{1}0\rangle$) was not observed.

The second central hydrogen atom was removed by applying a voltage exceeding 3.5 V. In STM images of the remaining Pc (Figure 5.3f) the molecular ligands appear with very similar heights ($\approx 45$ pm), which makes the molecule almost four-fold symmetric. This height is reduced compared to STM images of $H_2$Pc acquired at the same voltage ($\approx 55$ pm and $\approx 70$ pm parallel and perpendicular to $\langle 1\bar{1}0\rangle$) which reflects a modified bonding of the molecule to the surface mediated by the unsaturated nitrogen atoms.

The final step of the metalation reaction is the insertion of a metal ion into the completely dehydrogenated inner macrocycle. Previously the transfer of single atoms from the tip to metal surfaces has been observed and attributed to strong adhesive forces [16, 91, 183, 184]. Although the Pc molecule is adsorbed on a metal substrate the dehydrogenated molecular center may be expected to be rather reactive towards an atom at the apex of an STM tip. Therefore, the tip was approached to the molecular center at low voltage (0.1 V). Figure 5.4a displays the evolution of the current, $I$, with the displacement, $\Delta z$, of the tip (the direction of the tip approach is from right to left). Starting from the tunneling range the current rises exponentially as expected. At $\Delta z \approx -30$ pm, an abrupt increase of the current from $\approx 0.15\,\mu$A to $0.26\,\mu$A occurs, which signals the formation of a tip–molecule contact. In repeated experiments using a sample voltage $V = 0.1$ V, the conductance, $I/V$, of the single molecule contact exhibited some variability over the range $0.009 \ldots 0.036\,G_0$, where $G_0 = 2e^2h^{-1}$ is the quantum of conductance.

For tip displacements up to $\approx 80$ pm beyond contact formation no modifications of the molecule were observed in STM images subsequently recorded. Further approach of the tip to $\Delta z \approx -120$ pm results in a second abrupt increase of the current from $\approx 0.95\,\mu$A to $\approx 1.5\,\mu$A. Subsequent imaging in the tunneling range (Figure 5.3g) reveals a drastic change of the molecular structure. The central depression of the empty inner macrocycle (Figure 5.3f) has turned into a protrusion with an apparent height of $\approx 77$ pm (Figure 5.3g). The STM image suggests that an atom has been transferred from the tip to form a metallized Pc (MPc)[1,2]. The intermediate product molecule can be laterally moved by the tip at elevated tunneling current ($I = 400$ nA,

[1] An alternative explanation, capture of a substrate atom, appears unlikely. At the cryogenic temperature of the experiments diffusing ad-atoms are not available. The extraction of surface atoms upon contact is energetically less favorable than the abstraction of an atom from the tip [91]. Moreover, the STM images of the fabricated AgPc↓ and deposited AgPc are virtually identical. This appears to be inconsistent with a substrate atom missing underneath the fabricated molecule.

[2] We monitored the tip status by comparing the apparent height of the substrate before and after the metalation procedure. In 6 out of 11 metalation processes no change of the tip (defined as changes below 30 pm) was detected. In 3 cases the tip length increased by 1, 0.50, and 0.50 nm. In 2 cases the tip length decreased by 0.10 nm and 0.24 nm. These values cannot directly be interpreted in terms of added or removed single atoms. We attribute them to rearrangements of the atomic structure of a larger apex region.

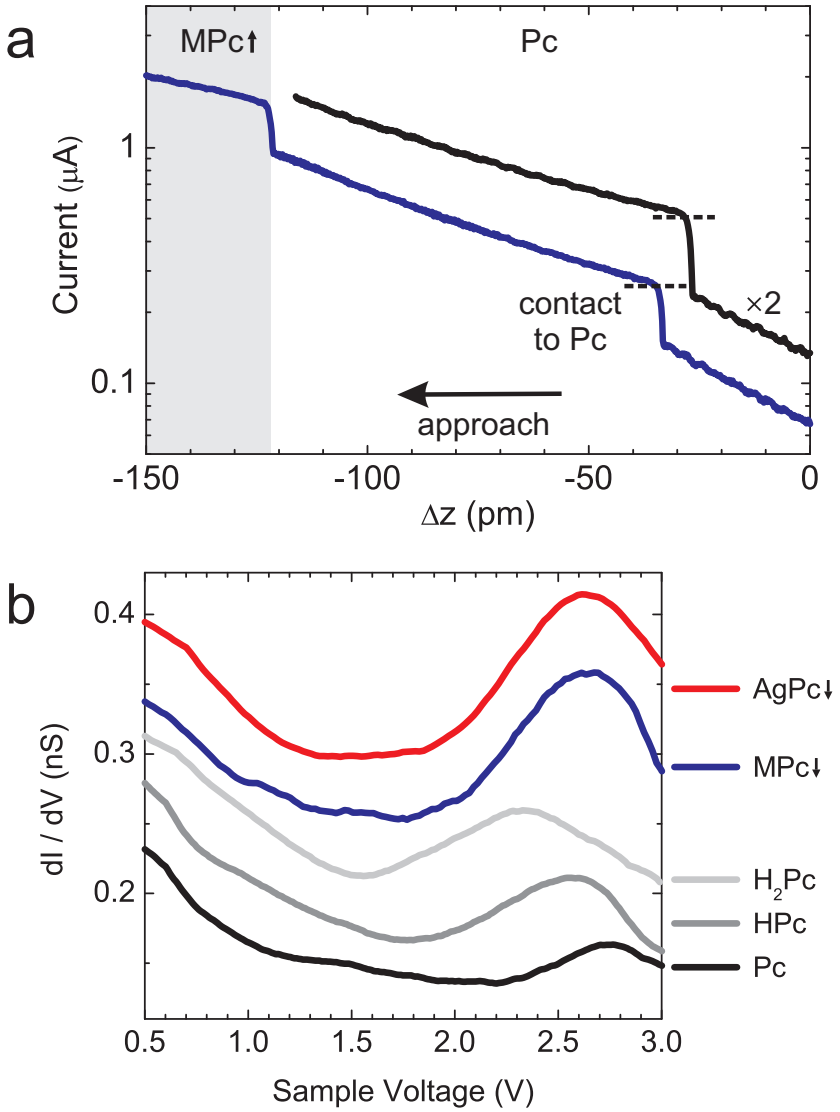


*Fig. 5.4:* (a) Evolution of the current upon approaching (from right to left) the tip to the center of a Pc molecule with dehydrogenated inner macrocycle. Zero displacement ($\Delta z = 0$) corresponds to the tip–molecule distance at 0.1 V and 67 nA. No irreversible changes of the molecular structure occur as long as $\Delta z > -120$ pm (black line). At contact (indicated by dashed lines) the conductance is $\approx 0.034\,G_0$. Further approach leads to a second abrupt rise of the current (blue) signalling the transfer of an atom from the tip to the molecule (Figure 5.3g). (b) Constant-current $dI/dV$ spectra of the molecules presented in Figure 5.3. Spectra are vertically offset for clarity in +0.05 nS steps. The broad peak at $\approx$ 2.5 V is attributed to the lowest unoccupied molecular orbital. While systematic differences exist between Pc, HPc, $H_2$Pc, and MPc the spectra of MPc↓ (blue) and sublimated AgPc (red) are identical within the experimental uncertainty.

$V = 0.1$ V) indicating its stability. As will become clear below, the new molecule is most likely AgPc with the Ag atom located at the vacuum side of the molecule (AgPc↑).

The injection of electrons at elevated voltages ($> 3$ V) at the center of the MPc↑ leads to a molecule with a central depression (Figure 5.3h, MPc↓)[3]. A similar interconversion from ↑ to ↓ configuration was reported for SnPc on Ag(111) [69]. With its four-fold symmetry the STM image of MPc↓ is similar to STM images of Pc but can be easily discriminated by its different apparent height, *e. g.*, $\approx 60$ pm for MPc↓ compared to $\approx 45$ pm for Pc. The STM image of MPc↓ is virtually identical to the image of AgPc molecules, which were sublimated onto Ag(111) at ambient temperature (Figure 5.3i). Sublimated AgPc molecules exclusively appear with a central depression in constant-current STM images, which is consitent with a position of the central Ag ion below the molecular plane (AgPc↓). It is therefore tempting to identify MPc↓ with AgPc↓. As a consequence, the MPc↑ configuration generated by the manipulation sequence presented above turns out to be metastable.

To further test the chemical identity of the synthesized MPc↓ molecule, spectra of $dI/dV$ were recorded at positive sample voltages to probe its lowest unoccupied molecular orbitals close to the Fermi energy (Figure 5.4b). The fingerprint of MPc↓ (blue line) is clearly different from those of $H_2$Pc (light grey), HPc (grey), and Pc (black). However, it is virtually identical to the data from sublimated AgPc (red), which further confirms the interpretation of Figures 5.3g,h in terms of ↑ and ↓ configurations of AgPc. In addition, the spectra provide a hint to the mechanism driving the interconversion from the ↑ to the ↓ configuration. Spectra of AgPc↓ exhibit a broad unoccupied orbital centered at $\approx 2.6$ V. The threshold voltage for interconversion of $\approx 3$ V is consistent with the injection of electrons into this orbital along with coupling to vibrational degrees of freedom of the molecule. The efficiency of such processes was previously studied theoretically [185] and in contact experiments with $C_{60}$ [85]. This type of mechanism appears to be at work in removing the second hydrogen atom from the inner macrocycle of HPc, too. Its threshold is higher than for the removal of hydrogen from $H_2$Pc in agreement with the different positions of the lowest unoccupied orbital (Figure 5.4b, black and gray lines).

## 5.4 Summary

In summary, we presented a stepwise single-molecule synthesis of AgPc on Ag(111) from $H_2$Pc. One may speculate with some confidence that this

[3] Attempts to induce the reverse process from ↓ to ↑ were not successful.

experimental approach will be feasible for a variety of metal ions and may be extended to other related molecules. It will be interesting to use these possibilities to tailor arrays of such molecules and probe their mutual coupling and properties.

## *Acknowledgements*

Financial support by the Schleswig-Holstein Fonds and the Deutsche Forschungsgemeinschaft through SFB 677 is acknowledged.

# 6. ELECTRONIC SUPERSTRUCTURE OF LEAD-PHTHALOCYANINE ON LEAD ISLANDS

## *6.1 Introduction*

Single crystal surfaces provide many opportunities for controlling the arrangement of functional molecules into ordered patterns [186–191]. While direct intermolecular interactions are particularly versatile and play a decisive role in determining molecular structures at surfaces, the interaction with a substrate leads to several additional possibilities. The geometric structure of a substrate with its atomic corrugation may favor particular molecular orientations and arrangements [192]. Electronic surface states mediate interactions which affect molecules over nanometer distances [111, 193, 194]. In addition to high symmetry surfaces, vicinal surfaces may be used, which exhibit regular arrays of steps and kinks [195–199]. Regular meshes of molecules may act as templates for selective adsorption [200–203]. A similar template effect may be achieved by metal-on-metal heteroepitaxy, where a small mismatch of lattice parameters may be used to generate long-range moiré patterns [204–207]. Densely packed molecular monolayers often exhibit moiré patterns themselves. Owing to their large unit cells, these patterns are most conveniently observed with STM. Over the unit cell of the moiré mesh, the relative positions of atoms in the layer and the substrate vary. The geometric pattern may be expected to induce a related variation of the electronic and other properties of the molecules. Indeed, short-range superstructures of the electronic states have been reported in a number of cases [208–211].

Here, we report on lead-phthalocyanine (PbPc) molecules adsorbed to Pb islands on Ag(111). Data from PbPc on Ag(111) are shown for comparison. As expected, the molecules lie flat on both substrates. Owing to their shuttlecock geometry PbPc molecules (Figure 6.1) adopt two adsorption configurations, either with the Pb atom above the molecular plane (PbPc↑) or below (PbPc↓). In contrast to other phthalocyanines, PbPc aggregates into large, ordered assemblies on Pb islands on Ag(111) even at low coverages. While we find equal amounts of PbPc↑ and PbPc↓ on Ag(111), on Pb islands

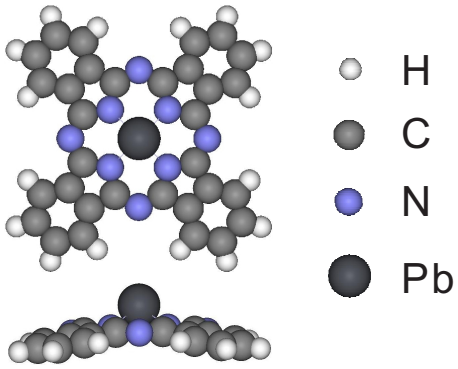


*Fig. 6.1:* Top and side views of the optimized geometrical structure of PbPc. Calculated with Gaussian 03 using a B3LYP/LANL2DZ basis set.

PbPc↑ is more abundant and forms almost pure PbPc↑ islands in various orientations with respect to the substrate lattice. For a particular orientation we find that the electronic structure of the molecules is periodically modulated, which leads to an electronic superstructure with a very large unit cell. Scanning tunneling spectroscopy is used to probe the molecular states and their interaction with quantum well states, which are characteristic of the underlying Pb islands.

## *6.2 Experimental Details*

The experiments were performed with a home-made STM operated at 7 K and in ultrahigh vacuum with a base pressure of $10^{-9}$ Pa. Ag(111) surfaces and chemically etched W tips were cleaned by $Ar^+$ bombardment and annealing. Pb was evaporated from a heated Pb-coated W filament and deposited onto Ag(111) at room temperature at a rate of 1 atomic layer per minute. A quartz microbalance used to monitor the flux was calibrated from STM images. PbPc molecules were deposited on Pb-covered Ag(111) at room temperature from a heated Ta crucible at a rate of 1 monolayer per minute. Based on the superstructure presented below, a monolayer (ML) of PbPc is defined as a surface density of 22 molecules per 280 Pb atoms. All images were acquired in the constant-current mode of the STM with the voltage applied to the sample. Spectra of the differential conductance ($\mathrm{d}I/\mathrm{d}V$) were acquired by superimposing a sinusoidal modulation (25 $\mathrm{mV_{rms}}$, 1.9 kHz) onto the sample voltage and measuring the first harmonic of the current response with a lock-in amplifier.

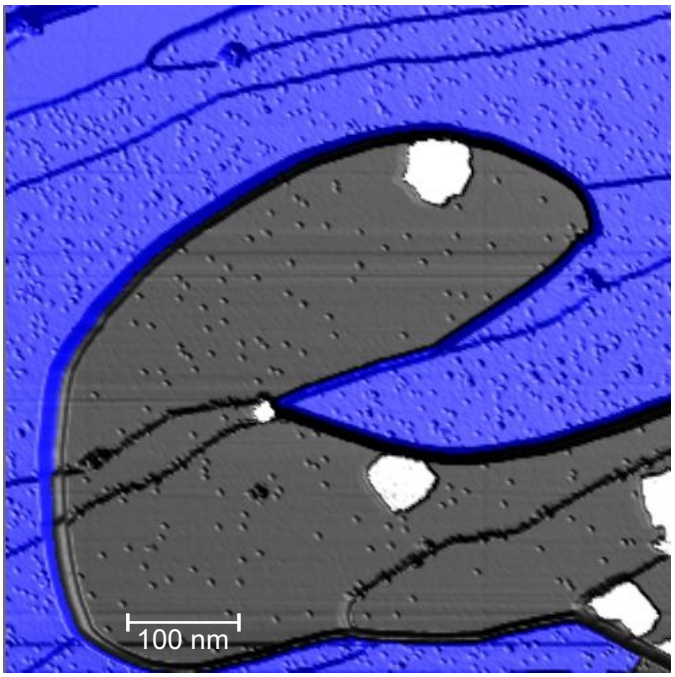


*Fig. 6.2:* Constant-current STM image of ≈ 0.07 ML PbPc adsorbed on a Pb island (6 ML, gray) as well as on the Pb wetting layer (blue) on Ag(111). The Pb island covers several Pb-wetted Ag(111) terraces while keeping a uniform thickness of 6 ML. Monatomic Ag(111) step edges appear as dark lines. While on the wetting layer the molecules adsorb separately, on the Pb island they form large islands (white) and only few single molecules are observed (600 nm × 600 nm, 0.1 V, 0.1 nA).

## 6.3 Results and Discussion

### 6.3.1 Structure

Pb grows on Ag(111) in the Stranski–Krastanov mode with an in-plane lattice constant corresponding to that of bulk Pb and forms islands with extended flat tops [212–214]. Figure 6.2 shows a large-scale STM image of PbPc molecules on Pb-covered Ag(111) at a coverage of ≈ 0.07 ML. The Pb wetting layer appears blue while a Pb island with 6 ML thickness is depicted in gray. This island covers several Pb-wetted Ag(111) terraces, whose step edges appear as dark lines. Single PbPc molecules are visible as circular protrusions at this image size. From this and similar STM images we infer a characteristic difference in the PbPc adsorption on the wetting layer and on Pb islands. While PbPc molecules preferentially adsorb as single molecules on

the wetting layer, they tend to form agglomerations on the islands. These agglomerations appear as white areas in Figure 6.2 and will be shown below to comprise a single molecular configuration.

Below, we focus on PbPc adsorbed on these lead islands, where the in-plane lattice constant corresponds to that of bulk Pb. Figure 6.3a shows a large-scale STM image of PbPc molecules (0.07 ML) on an 8 ML Pb island. While a large number of molecules (white) has aggregated into islands, a small number of PbPc (blue) remain isolated on the Pb substrate (gray). A close-up view of PbPc molecules is presented in Figure 6.3b. PbPc is imaged in two forms with either a central protrusion or a depression. Similar to earlier work for PbPc on $MoS_2$ [215] or on Ag(111) [216] these images may be attributed to two configurations with the Pb atom above (PbPc↑) or below (PbPc↓) the molecular plane. An alternative interpretation is that PbPc↓ corresponds to molecules that have lost their central Pb atom. For PbPc on Ag(111) it has been argued that Pb detachment from the molecule is likely owing to the propensity of Ag and Pb to form a surface alloy [216, 217]. The present data do not enable a clear decision between these possibilities. The figure also shows the typical clover-leaf shape of the molecule. One of the molecular axes encloses an angle of $\approx 10^\circ$ with $[1\bar{1}0]$ of Pb(111). Around the molecules, an additional height modulation with a spatial periodicity of $1.6 - 1.7$ nm is observed. Shown more clearly in Figure 6.3c, along with atomic resolution of the Pb mesh, the pattern is caused by a moiré effect, which reflects the lattice mismatch between Ag(111) and Pb(111). The moiré pattern is rotated by 25° with respect to the $[1\bar{1}0]$ direction of Pb(111). This angle corresponds to a rotation of the Pb(111) lattice by $4 - 5^\circ$ with respect to the Ag(111) lattice, in agreement with previous results [213]. The PbPc molecules are located with their central Pb atom close to the apparently highest point of the moiré unit cell.

Figure 6.3a reveals a clear preference of PbPc↑ to agglomerate in ordered islands. The molecules arrange in an approximately square unit cell which will be analyzed in more detail below. PbPc↓ molecules are more frequently observed as isolated molecules. Related observations were made for SnPc, another non-planar phthalocyanine, on Ag(111) [69, 218]. In this case, SnPc↓ agglomerates to form chains while SnPc↑ molecules remain isolated. This preference has been interpreted in terms of the higher calculated dipole moment of adsorbed SnPc↑ compared to SnPc↓, which is expected to lead to more repulsive interaction [218]. The present data indicate that the charge transfer between the molecule and the substrate is different for PbPc and leads to a higher electrical dipole moment for PbPc↓ than for PbPc↑.

Figure 6.3a shows that PbPc↑ molecules are significantly more abundant on Pb islands than PbPc↓. Counting molecules with different configurations

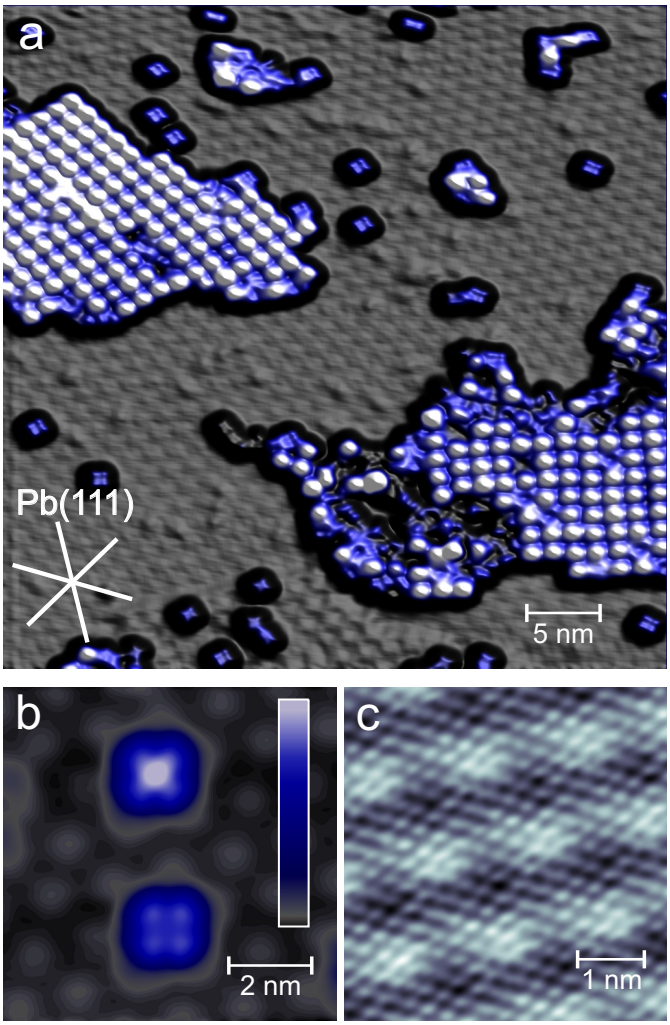


*Fig. 6.3:* (a) Constant-current STM image of ≈ 0.07 ML PbPc adsorbed on a Pb(111) island (8 ML) on Ag(111) (40 nm × 40 nm, 0.1 V, 0.1 nA). The data are shown as an illuminated pseudo-threedimensional relief to enhance the visibility of small features. The close-packed directions of the Pb(111) island are indicated by lines. (b) Close-up view of PbPc on an 8 ML Pb island (7.8 nm × 8.0 nm, 0.1 V, 0.1 nA). PbPc is imaged in two forms with either a central protrusion or a depression. The color scale covers a height range from 0 (black) to 0.25 nm (white). (c) Atomically resolved image of an 8 ML Pb island. It exhibits a moiré pattern with a spatial periodicity of $1.6 - 1.7$ nm (4.8 nm × 5.0 nm, 0.1 V, 0.1 nA).

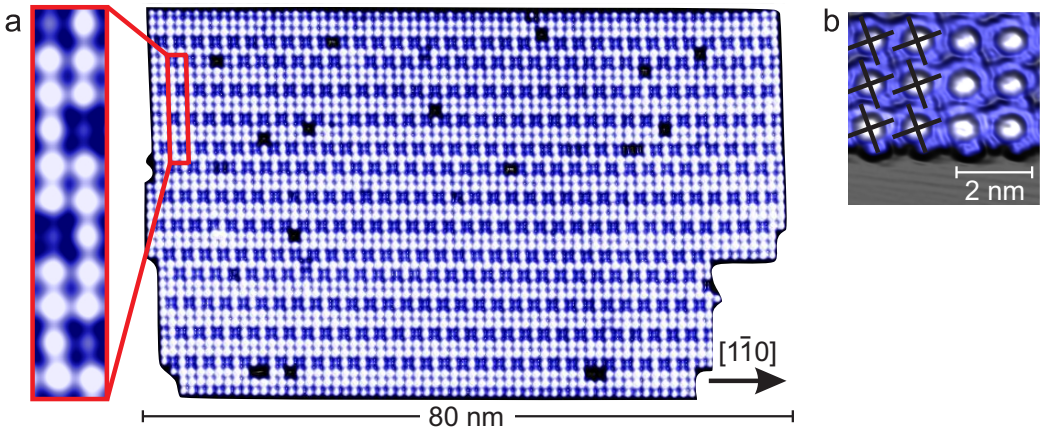


*Fig. 6.4:* (a) Constant-current STM image of $\{2\times11\}$ PbPc↑ superstructure on a 6 monolayer Pb island on Ag(111) (80 nm × 49 nm, 3 V, 0.1 nA). The arrow indicates the [1$\bar{1}$0] direction of the Pb(111) layer. The STM images in b is shown with the same orientation. A rectangle delineates a unit cell of the superstructure. Defects (dark depressions) are due to PbPc↓ or missing molecules. The small deviation of the angle between the island edges from 90° is due to an asymmetry of the piezoelectric scanner of the STM. (b) Close-up view of molecules at an island edge (5.1 nm × 5.1 nm, 0.1 V, 0.1 nA). Crosses indicate the molecular axes.

on the wetting layer and on the surface of Pb islands within areas of the same dimensions leads to the following ratios. On Pb islands the ratio of PbPc↑ with respect to the total number of molecules on the island is ≈ 95 %, while this ratio on the wetting layer is ≈ 5 %. When only single molecules are considered, *i. e.*, omitting the ordered PbPc↑ arrays, the ratio of PbPc↑ is virtually the same as on the wetting layer. The vastly different adsorption behaviors of PbPc on the Pb wetting layer and on Pb islands on Ag(111) may be interpreted in terms of different adsorption energies. The observed molecular assemblies hint at a higher adsorption energy of PbPc↓ than PbPc↑ on the wetting layer and an inverse situation on the Pb islands. The conversion of PbPc↑ into PbPc↓ on the wetting layer and of PbPc↓ into PbPc↑ on the Pb islands may occur via a vertical movement of the central Pb ion through the molecular plane. While this movement requires ample energy in the gas phase (4.27 eV) [219] it may be reduced upon adsorption. Another conversion scenario is flipping of the molecule, which may occur as a rotation of the molecule about an axis parallel to the surfaces as reported for chloro[subphthalocyaninato]-boron(III) on Cu(100) [220]. Additionally, from

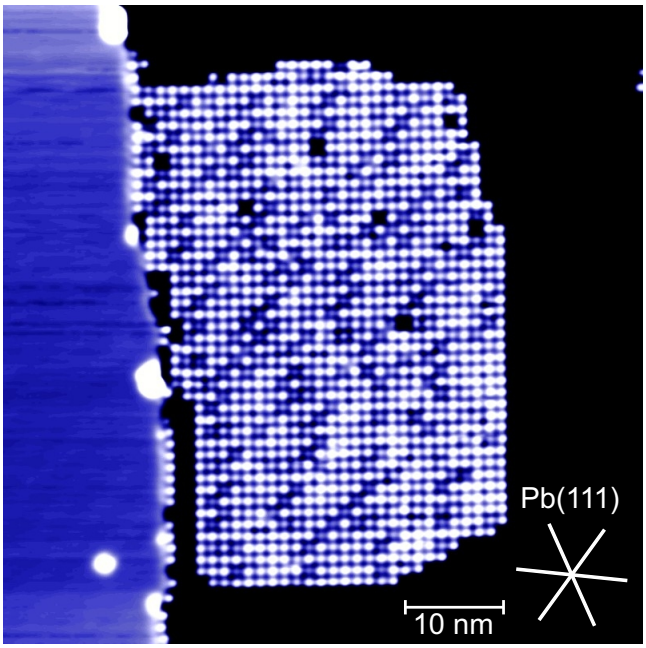


*Fig. 6.5:* Constant-current STM image of PbPc↑ molecules on a Pb island (thickness 6 ML) on Pb-wetted Ag(111) (65 nm × 65 nm, 3 V, 0.1 nA). This island is not oriented along a crystallographic direction (indicated by the cross) and does not exhibit the $\{2 \times 11\}$ superstructure.

the observation of ordered PbPc↑ arrays one may infer an enhanced mobility of PbPc↑ at room temperature.

Surveys of large surface areas revealed various orientations of the edges of islands of PbPc↑ molecules. The lack of a preferred orientation indicates that the potential energy landscape of the Pb-molecule interaction is rather weakly corrugated. However, some islands stand out. Islands whose edges are oriented along the Pb(111) $[1\bar{1}0]$ direction exhibit a superstructure (Figure 6.4a) of apparently higher (white) and lower (blue) molecules. The island of Figure 6.4a contains more than 2500 PbPc↑ molecules whose central Pb atoms appear as protrusions with different apparent heights. Some defects (black) are observed, which are due to PbPc↓ molecules or empty sites, but they do not perturb the long range periodicity of the arrangement. While the superstructure is related to a geometric moiré pattern discussed below, the striking height modulation is essentially due to a concomitant electronic effect. The superstructure is absent from STM images recorded at low sample voltages (Figure 6.4b), but it dominates the image contrast at more elevated voltages ($> 1$ V). Further, the superstructure vanishes even at elevated volt-

ages as soon as none of the island edges is oriented along the $[1\bar{1}0]$ direction (Figure 6.5). From these two observations we infer that molecules within the island adopt a uniform configuration, PbPc↑. In particular, it is the registry with the substrate which determines the apparent height of these molecules. The electronic superstructure exhibits an extraordinarily large unit cell and long range periodicity. At the voltage used in Figure 6.4a, 3 V, the apparent height difference between high and low protrusions is $\approx 0.035$ nm. The left panel of Figure 6.4a shows a close-up view of the unit cell of the superstructure, which contains 18 PbPc↑ molecules with bright and 4 PbPc↑ molecules with less bright centers. The matrix notation of the superstructure reads $\begin{pmatrix} 7 & -7 \\ 20 & 20 \end{pmatrix}$ on the basis of the Pb(111) lattice vectors $\mathbf{a_1}$ and $\mathbf{a_2}$ depicted in Figure 6.6. For simplicity, we refer to this superstructure as the $\{2 \times 11\}$ structure since its unit cell contains $2 \times 11$ molecules.

The ligands of the molecules are hardly visible at voltages that clearly show the superstructure. At lower voltages ($< 1$ V) the apparent height of the central Pb atoms is virtually identical for all PbPc↑ molecules embedded in the island (Figure 6.4b). Moreover, the ligands of the molecules are discernible, which enables a determination of the molecular axes (black crosses in Figure 6.4b). One axis encloses an angle of $\approx \pm 20°$ with the $[1\bar{1}0]$ direction of Pb(111). This angle induces a chirality of the metal–molecule complex. As a result, islands are usually homochiral, although domain boundaries between $+20°$ and $-20°$ domains occasionally occur.

### *Model*

The experimental observations suggest a model of the adsorption geometry (Figure 6.6). Molecules are represented by white and blue crosses, which indicate high (bright) and low (dim) PbPc↑ molecules, respectively, in STM images (Figure 6.4a). The $\{2 \times 11\}$ unit cell is marked by the rectangle. The experimental intermolecular distances of 1.22 nm along $[1\bar{1}0]$ and 1.16 nm perpendicular to this direction are reproduced by the model, which places the Pb atoms of bright molecules close to bridge or hollow sites of the Pb layer and dim molecules close to on-top sites. Assuming that the bonding of PbPc at bridge or hollow sites is different compared to on-top positions, the model is consistent with the observed modulation of the molecular electronic structure (see below). Moreover, in agreement with the experimental results, the $\{2 \times 11\}$ superstructure is lost as soon as none of the island edges is oriented along the $[1\bar{1}0]$ direction (Figure 6.5).

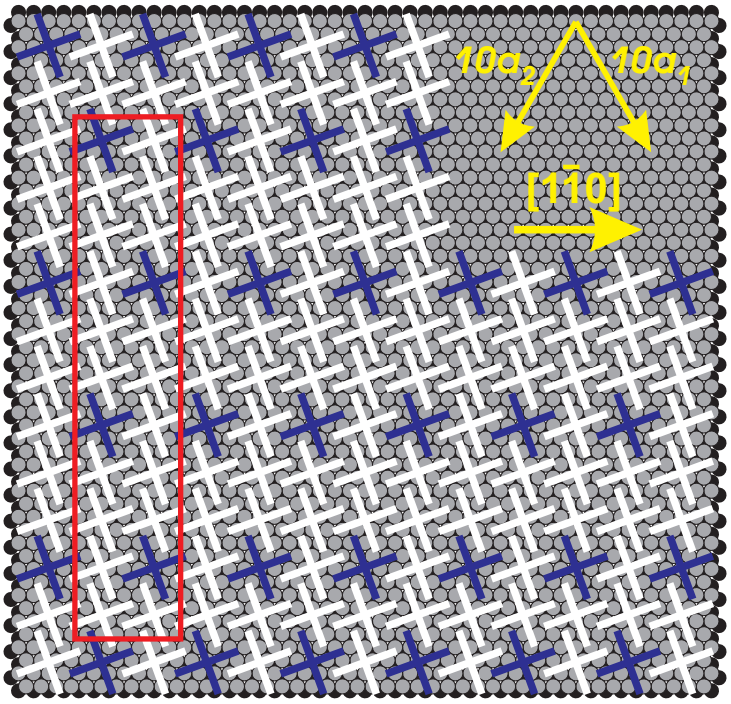


*Fig. 6.6:* Schematic representation of the suggested adsorption geometry of PbPc↑ molecules on a hexagonal Pb layer. The rectangle depicts the $\{2 \times 11\}$ unit cell. The unit cell vectors $\mathbf{a_1}$ and $\mathbf{a_2}$ of the underlying Pb(111) lattice are indicated by the arrows.

### *PbPc on Ag(111)*

The structure of PbPc on pristine Ag(111) (Figure 6.7) is rather different from the pattern observed on Pb-covered Ag(111). Again, molecules with central protrusions (PbPc↑) and depressions (PbPc↓) are observed. At lower coverages ($\approx 0.1$ ML, not shown), the adsorption of single molecules is frequently observed while small agglomerations in the form of molecule chains occur scarcely. At higher coverages islands containing PbPc↑ and PbPc↓ molecules form. A typical STM image of PbPc on Ag(111) at a coverage of $\approx 0.2$ ML is shown in Figure 6.7a (1 ML corresponds to a surface density of 1 molecule per 25 Ag atoms). Very large islands have formed, while single molecules appear rarely on the surface. A close-up view of the indicated island in Figure 6.7a is presented in Figure 6.7b. Within the island molecular chains are found along a direction that encloses an angle of 8° with $[1\bar{1}0]$. Both configurations, PbPc↑ and PbPc↓, appear with identical abundances (*e. g.*, $\approx 48\,\%$ PbPc↑, $\approx 52\,\%$ PbPc↓ in an array of 1250 molecules).

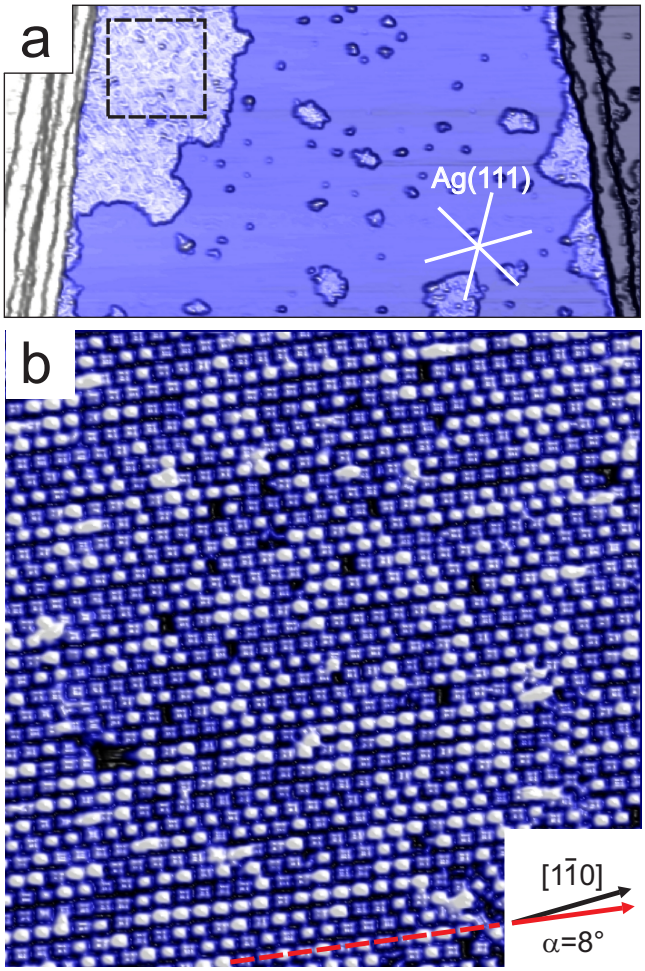


*Fig. 6.7:* (a) STM image of PbPc on Ag(111) at a coverage of $\approx 0.2$ ML (146 nm $\times$ 295 nm, 100 mV, 0.1 nA). (b) Close-up view of the indicated area in (a) (45 nm $\times$ 45 nm). PbPc$\uparrow$ and PbPc$\downarrow$ appear with, respectively, central protrusions and depressions. Inset: Angle $\alpha = 8°$ enclosed by the molecule chain direction and a Ag(111) compact direction.

The identical abundances indicate that adsorption energies of both molecular configurations are similar and no conversion of PbPc↑ into PbPc↓ and vice versa has occurred upon adsorption. While a comparison of PbPc↑ and PbPc↓ adsorption energies on Ag(111)[1] is not available, for an apparently similar case, SnPc on Ag(111), these data exist [69, 218]. At low submonolayer coverages, SnPc↑ and SnPc↓ configurations appear with nearly identical abundances and exhibit adsorption energies, which differ by $\approx 0.5\,\mathrm{eV}$ [218]. Furthermore, conversion of SnPc↑ into SnPc↓ on Ag(111) requires an energy of $\approx 1.5\,\mathrm{eV}$, which makes a thermally induced vertical movement of the Sn ion through the molecular plane rather unlikely [69].

The intermolecular distances of $\approx 1.5\,\mathrm{nm}$ are $\approx 25\,\%$ larger than observed on Pb-covered Ag(111). Clearly, the adsorption energy landscape is different compared to Pb-covered Ag(111). The increased intermolecular distances in the islands again hints at a repulsive molecular interaction at close distances. While disordered PbPc assemblies on Ag(111) were reported from molecules deposited at 570 K [216], our data from PbPc deposited at ambient temperature show little disorder, except for molecules at island edges.

### 6.3.2 Electronic properties

Pb islands are a particularly interesting substrate as they exhibit quantum well states [214, 221–224]. Figure 6.8a (gray line) shows a $\mathrm{d}I/\mathrm{d}V$ spectrum, which was recorded at constant current, on 6 ML Pb island. Three quantum well peaks are the dominating features in these data. Spectra of $\mathrm{d}I/\mathrm{d}V$ acquired above the centers of PbPc↑ molecules on the same island are shown by red and blue lines. Peaks are observed at $\approx 0.7$, 2.1, 2.6, 3.1, and 3.4 V. The voltages of the features at $\approx 2.1$, 3.1, and 3.4 V vary little ($\approx 200\,\mathrm{mV}$, shaded rectangles in Figure 6.8a, b) with different thicknesses of the Pb islands. We therefore attribute them to molecular orbitals. The other peaks reflect quantum well states of the Pb layer [214], but are slightly shifted by the presence of the molecules. Their energies (Figure 6.8b, circles) vary with the Pb thickness as expected [214, 222].

#### *Molecular orbitals*

While the features related to quantum well states will be discussed below, we first focus on the apparent height difference between bright and dim molecules. Figure 6.8a compares spectra from PbPc↑ molecules located at hollow/bridge (red line) and on top (blue line) adsorption sites. According to

[1] The binding energies for PbPc↓ on Ag(111) at hcp (fcc) adsorption site were determined by Baran *et al.* [216] as 0.71 eV (0.59 eV). For PbPc↑ no data is available.

the model in Figure 6.6, PbPc↑ and PbPc↓ molecules are centered close to on-top and bridge or hollow positions, respectively. Their spectra only deviate at voltages larger than $\approx 1\,\mathrm{V}$, which explains the observed variation of the image contrast with the sample voltage. For voltages $< 1\,\mathrm{V}$ the centers of PbPc↑ molecules appear with similar heights throughout the $\{2 \times 11\}$ superstructure (Figure 6.4b) whereas for voltages $> 1\,\mathrm{V}$ the centers appear high or low (Figure 6.4a). Similar adsorption site-dependent electronic structures have been reported for other molecules [78, 208–211].

*Quantum well states*

Returning to the quantum well states in Figure 6.8, we find that the spectral peaks occur at slightly higher voltages in molecular spectra than on the Pb island underneath (cf. encircled pairs of data points in Figure 6.8b). On average, the shift amounts to $\approx 100\,\mathrm{mV}$ towards higher voltages and is rather independent of the energy of the quantum well states. However, it slowly decreases with increasing thickness.

The phase accumulation model [225, 226] may be used to tentatively interpret this shift. Within this model, the energy $E_n$ of quantum well state $n$ may be calculated from

$$2\,(d + d_0 + d_{\mathrm{mol}})\,k(E_n) + \Phi_0 + \Phi_{\mathrm{mol}} = 2\pi n. \tag{6.1}$$

Most parameters of this equation are available from previous work on Pb quantum well states. $k(E_n)$ denotes the wave vector of the quantum well state parallel to the surface normal and has recently been reported to depend almost linearly on $E_n$ for pristine Pb on Ag(111) [214]. $\Phi_0$ is the phase shift the quantum well state experiences upon reflection at the Ag–Pb interface. It may be empirically evaluated as

$$\Phi_0 = 2\,\sin^{-1}\sqrt{\frac{E_n - E_{\mathrm{l}}}{E_{\mathrm{u}} - E_{\mathrm{l}}}} \tag{6.2}$$

with $E_{\mathrm{l}} = -0.4\,\mathrm{eV}$ [227] and $E_{\mathrm{u}} = 3.9\,\mathrm{eV}$ [227] denoting the lower and upper edges of the surface-projected Ag(111) band gap [214, 228, 229]. Two new parameters were introduced in Equation (6.1) to model the molecule, namely $\Phi_{\mathrm{mol}}$, the scattering phase at the molecule, and $d_{\mathrm{mol}}$, which mimics a change of the effective film thickness.

For $\Phi_{\mathrm{mol}}$ we use an expression originally derived for a vacuum barrier within the Wentzel-Kramers-Brillouin approximation [230],

$$\Phi_{\mathrm{mol}} = \pi\left(\sqrt{\frac{3.4\,\mathrm{eV}}{E_{\mathrm{V}} - E_n}} - 1\right) \tag{6.3}$$

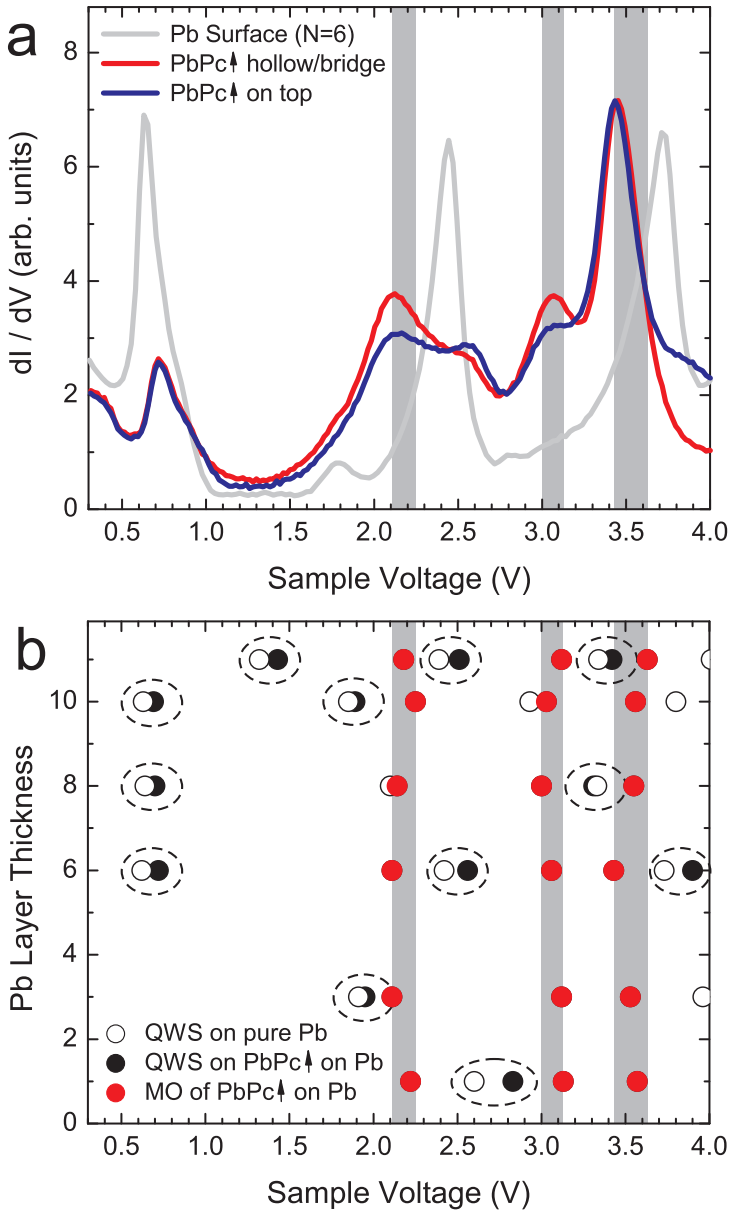


*Fig. 6.8:* (a) Constant-current ($I = 0.1\,\mathrm{nA}$) $\mathrm{d}I/\mathrm{d}V$ spectra. Red and blue lines show data acquired above the centers of high and low PbPc↑ molecules, respectively. The different heights are attributed to different adsorption position with the molecular center close to bridge/hollow sites (red) and on-top sites (blue). A spectrum from the underlying Pb island (6 ML) is shown in gray. Shaded areas indicate the variation of molecular orbitals with the thickness of the islands. (b) Variation of spectroscopic features with the thickness of the Pb islands. ○: quantum well states (QWS) on pristine Pb islands, ●: QWS on PbPc↑, and ●: PbPc↑ molecular orbitals (MO). Ellipses indicate the shift between QWS on pristine Pb and molecules. MO energies vary little with island thickness (shaded areas). In contrast, QWS energies depend strongly on the thickness.

with the vacuum energy, $E_V$, and $E_n$ given in units of eV. The thickness of the Pb island is $d = Na$ with an interlayer separation of $a = 0.286\,\text{nm}$ [213]. The constant $d_0$ takes into account the different positions of the Ag–Pb interface and the jellium plane between the Ag substrate and the Pb film and has recently been determined as $d_0 = -0.018\,\text{nm}$ [214]. $d_0$ and $\Phi_0$ describe the Ag–Pb interface and are not affected by the presence of a molecule. As a result, the only adjustable parameters of the model are $d_{\text{mol}}$ and $E_V$. We find that $d_{\text{mol}} = -0.015\,\text{nm}$ and an unchanged value for $E_V$ compared to pure Pb films on Ag(111), *i. e.*, $E_V = 4.5\,\text{eV}$ [214], reproduce the experimental shift of the quantum well states. Moreover, the calculated shift is rather independent of $E_n$ and decreases with increasing thickness $N$ in agreement with the experimental results. As an alternative model, we considered a change of the local work function induced by PbPc. The work function may affect the vacuum energy, $E_V$ and, via Equation (6.3), $\Phi_{\text{mol}}$. However, a modified $E_V$ leads to a considerable dependence of the energy shift as a function of $E_n$, which was not observed in the experiments. As a consequence, the observed shift of quantum well state energies is dominantly influenced by a reduction of the effective Pb layer thickness.

## 6.4 Summary

Structural and electronic properties of PbPc on Pb-covered Ag(111) have been investigated. PbPc↑ molecules arrange in ordered arrays. PbPc↓ molecules preferentially remain as isolated molecules. An electronic superstructure with long range order and a large unit cell has been observed from PbPc↑ arrays with a specific orientation. Moreover, PbPc interacts with the quantum well states of the Pb islands and causes an increase of their energies. On Ag(111), PbPc molecules arrange into a significantly less dense pattern and, at low coverages, remain almost isolated.

## Acknowledgements

Financial support by the Deutsche Forschungsgemeinschaft through SFB 677 is acknowledged. We thank Rainer Herges, Yongfeng Wang, Thiruvancheril G. Gopakumar and Werner A. Hofer for discussions.

# 7. DEMETALATION OF AN ORGANOMETALLIC COMPLEX AT THE SINGLE-MOLECULE LEVEL

## *7.1 Introduction*

Phthalocyanine (Pc) molecules are perceived as promising candidates for nanotechnological applications [11]. They are planar organometallic complexes with extended $\pi$-conjugation and offer, along with their stability and availability [10], a wide range of functionalities such as chemical reactivity, optoelectronic conductance, optical absorbance and acting as electron donors or acceptors [10, 231]. The central metal ion of Pc molecules has recently attracted particular interest. It has been shown that the spin state of FePc molecules on Au(111) can be controlled by ligand attachment to the Fe atom [232]. Further, the reversible vertical movement of the central metal ion through the molecular plane of a Pc molecule has been considered as a single-molecule switch [69, 233]. To understand the chemical reactivity of the central metal ion and its influence on the electronic structure of the molecule, metal-free $H_2$Pc molecules have been metalized by exposing preadsorbed $H_2$Pc to metal atoms [169, 170, 173, 174, 234]. The controlled metalation of a single $H_2$Pc molecule using the tip of an STM has recently been reported [235].

Here, we show the preparation of a demetalized Pc at the single-molecule level. The central metal ion of PbPc molecules adsorbed on ultrathin Pb films on Ag(111) has been transferred from the inner macrocycle to the apex of the tip of a scanning tunneling microscope (STM). The increased length of the tip and the spectroscopic fingerprints of reactants and products provide clear evidence for the demetalation process.

## *7.2 Experimental Details*

The experiments were performed with a home-made STM operated at 7 K and in ultrahigh vacuum with a base pressure of $10^{-9}$ Pa. Ag(111) surfaces and chemically etched W tips were cleaned by $Ar^+$ bombardment and annealing. Pb was evaporated from a heated Pb-coated W filament and deposited

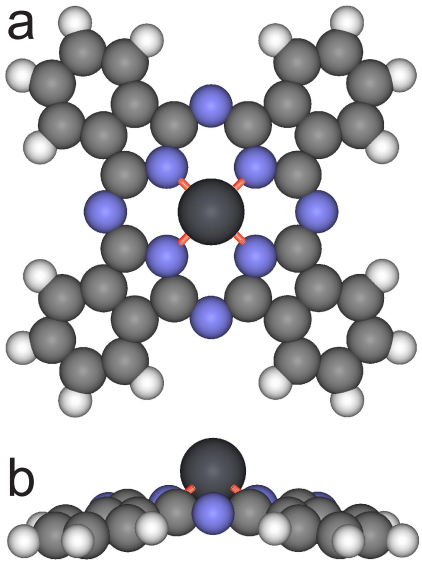


*Fig. 7.1:* (a) Top and (b) side views of optimized structures of PbPc in the gas phase. Calculations were performed using Gaussian 03 with a B3LYP/LANL2DZ basis set. Demetalation of the PbPc requires breaking of the red indicated bonds of the Pb ion and the four N atoms of the inner macrocycle.

onto Ag(111) at room temperature at a rate of 1 monolayer (ML) per minute. PbPc molecules were deposited on Pb-covered Ag(111) at room temperature from a heated Ta crucible at a rate of 1 ML/min$^{-1}$. Deposition rates were monitored with a quartz microbalance and calibrated from STM images. *In vacuo*, the tips were conditioned by indentation into Pb islands. As a consequence of this tip treatment the tip apex is most likely covered with Pb. All images were acquired in the constant-current mode with the voltage applied to the sample. Spectra of the differential conductance ($dI/dV$) were acquired by superimposing a sinusoidal modulation (25 mV$_{\mathrm{rms}}$, 1.9 kHz) onto the sample voltage and measuring the first harmonic of the current response with a lock-in amplifier.

## 7.3 Results and Discussion

Demetalation of a metal-phthalocyanine requires breaking of chemical bonds between the central metal ion and the four N atoms of the inner macrocycle (Figure 7.1a). PbPc molecules are favorable candidates for this process as the molecule adopts a shuttlecock geometry (Figure 7.1b) with the central Pb atom weakly bonded to the Pc. According to density-functional calculations

for the gas phase molecule using Gaussian 03 with a B3LYP/LANL2DZ basis set, the Pb ion is positively charged. On the surface the molecule may be found in two configurations, PbPc↑ and PbPc↓, in which the Pb atom is located above or below the molecular plane [236].

The proposed demetalation process is schematically depicted in Figure 7.2a. The tip is approached towards the central Pb atom of PbPc↑ at elevated negative tip voltage. At small distances the Pb cation is detached from the macrocycle and transferred to the tip apex while the remaining empty Pc adopts a flat geometry.

Figure 7.2b shows six molecules of a PbPc↑ array on Pb on Ag(111). To demetalize PbPc↑ molecule at the island edge the tip was approached to the center of the molecule marked by a black cross at a sample voltage of +2 V. During the approach the current recorded simultaneously suddenly dropped, which, as will be discussed below, signals the demetalation process. Next, the tip was retracted and an STM image of the demetalized molecule (Figure 7.2c) was recorded. The central protrusion of the original PbPc has been converted into a depression. More quantitatively, the apparent height (with respect to the metal substrate) of the center after demetalation is $\approx 120$ pm compared to $\approx 270$ pm for PbPc↑. Simultaneously, the additional atom at the tip apex leads to a retraction of the tip above the metal surface from Figure 7.2b to Figure 7.2c of $\Delta h \approx 110$ pm.

To demonstrate the reproducibility of the demetalation process, the procedure was repeated on the PbPc↑ molecules marked with red crosses in Figure 7.2c. The measured retraction of the tip was $\Delta h = 60 - 120$ pm per transferred Pb atom. Negative values of $\Delta h$ were not observed. Demetalation is accompanied by lateral translation of the molecule (270 – 350 pm) from its original position (Figure 7.2b–d). Moreover, some rotation occurs. Demetalation of molecules within dense arrays is feasible, too (Figure 7.2e, f). STM images of such molecules exhibit submolecular resolution of the ligands, in contrast to the less feature-rich images of molecules at island edges (Figure 7.2c, d). Moreover, within arrays demetalized molecules appear higher (height $\approx 190$ pm) than at edges. Lateral translation or rotation do not occur.

The experimental observations are consistent with the process of Figure 7.2a. The conversion of the central protrusion into a depression may safely be attributed to the transfer of the Pb ion to the tip apex as it leads to stepwise retraction of the tip upon each demetalation process. Demetalation of free PbPc changes the molecular geometry from shuttlecock-shaped to flat. Adsorbed to a surface, flat Pc is expected to require more space than

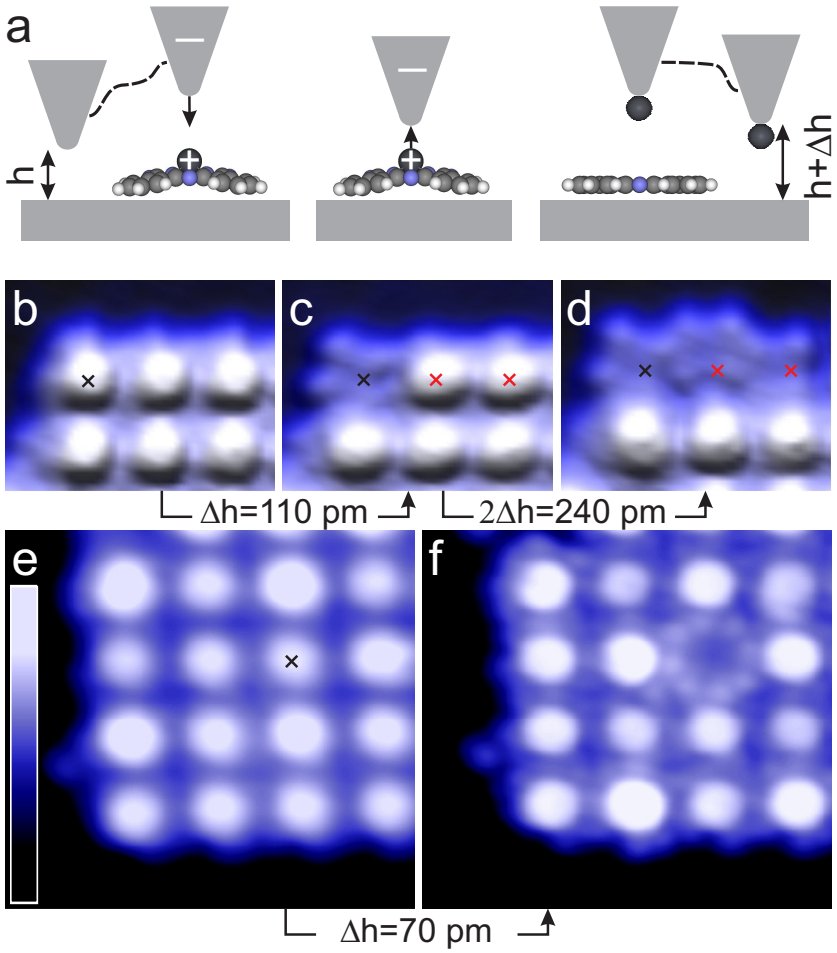


*Fig. 7.2:* (a) Schematics of the demetalation of a PbPc molecule. From its initial position above the metal substrate, with a tip height $h$, the tip is moved to the center of PbPc and approached to the Pb ion. Next, transfer of the Pb atom to the tip apex occurs. Subsequent imaging reveals a modified molecular geometry. Moreover, the tip height above the substrate has increased to $h + \Delta h$. (b–d) Pseudo three-dimensional representations of constant-current STM images of PbPc↑ islands on 3 ML of Pb on Ag(111) (4.4 nm × 3.5 nm, 0.1 V, 0.1 nA). (b) before demetalation. (c) after demetalation of the molecule marked by a black cross. (d) after demetalation of the molecules marked by red crosses. From (b) to (c) the tip has retracted by $\Delta h = 110$ pm. From (c) to (d), $\Delta h = 240$ pm. (e–f) Constant-current STM images of PbPc↑ islands. (3 ML of Pb on Ag(111), 12.4 nm × 5.7 nm, 0.1 V, 0.1 nA.) (e) prior to and (f) after demetalation of the indicated molecule. The lobes of the remaining Pc appear higher in STM than those of demetalized molecules at the edges of PbPc arrays. In contrast to other molecules, it exhibits clear submolecular features. The color scale applies to (b–f) and covers apparent heights from 0 (black) to 280 pm (white).

PbPc[1]. Indeed, molecules at edges laterally move and rotate upon demetalation. Within arrays, where neighboring molecules constrain lateral motion, demetalized Pc is apparently lifted from the substrate. This is reflected by the submolecular resolution of the molecules, which is typical of partial electronic decoupling from the metal substrate [64, 182, 206, 237]. The increased apparent height in STM images is supplementary indication.

In principle, the procedure described in Figure 7.2a may convert a PbPc↑ into a PbPc↓ molecule, which likewise appears with a central depression in STM images [236]. However, $dI/dV$ spectra of PbPc↑, PbPc↓, and demetalized Pc molecules are distinctly different (Figure 7.3a). The spectrum of PbPc↑ (black) exhibits a broad feature due to an unoccupied molecular orbital (MO) centered at $\approx 2.1\,\mathrm{V}$ [236]. For PbPc↓ (red) this feature is slightly shifted to $\approx 2.2\,\mathrm{V}$. Calculation of the frontier orbitals of a similar system, PbPc on Ag(111), show that the lowest unoccupied molecular orbital exhibits some spectral weight at the Pb site, which may be the case here, too [216]. The spectrum of demetalized Pc (green) from Figure 7.2f, however, is virtually featureless. Moreover, the spectra of PbPc↑ and PbPc↓ exhibit an additional shoulder at $\approx 2\,\mathrm{V}$ (blue dashed line), which is due to a quantum well state of the Pb film [214]. The absence of this state from the spectrum of demetalized Pc is consistent with the suggested partial decoupling of the molecule from the substrate. Overall, these differences are supplemental evidence for demetalation.

We note that demetalation of PbPc↑ did not occur at low bias voltage (0.1 V) but was successful at elevated positive sample bias. This may indicate that the demetalation involves injection of electrons into the unoccupied MO along with vibrational excitation [85, 135]. Moreover, the orientation of the electric field in the junction favors transfer of the Pb ion to the tip.

The demetalation process exhibits some variability, which is most clearly seen in repeated measurements of the evolution of the current, $I$, with the displacement of the tip, $\Delta z$, towards the central Pb atom (Figure 7.3b). Starting from the tunneling range ($0 > \Delta z > -100\,\mathrm{pm}$) $I$ increases approximately exponentially until a drastic order-of-magnitude drop occurs[2]. Beyond this point, $I$ again grows exponentially at a rate which is similar to that of the tunneling range. The tip displacement where the drop takes place and the magnitude of the current show some scatter. In all cases, however, images recorded after the current drop occurred showed a demetalized molecule whereas smaller tip displacements left the PbPc intact. The cur-

[1] The intermolecular distance of $\approx 1.2\,\mathrm{nm}$ in PbPc islands is significantly smaller than observed from other metal-phthalocyanines [170, 174, 182, 194].

[2] The width of the drop is broadened due to using a low-pass filter ($-3\,\mathrm{dB}$ cutoff at $10\,\mathrm{kHz}$).

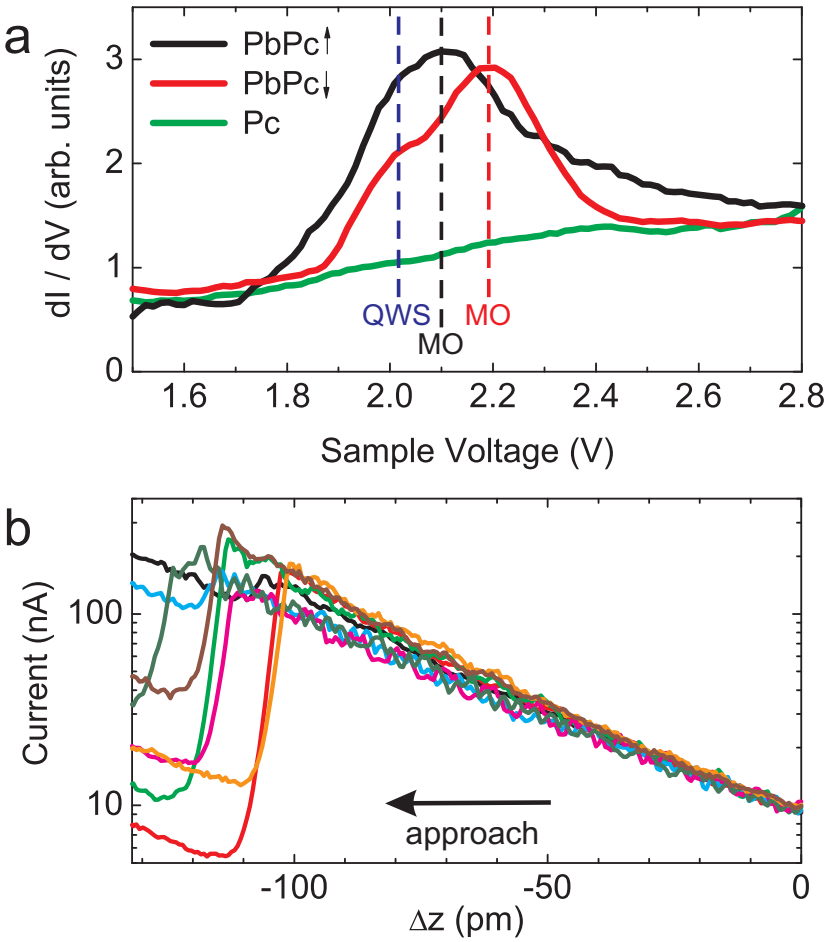


*Fig. 7.3:* (a) Constant-current $dI/dV$ spectra of PbPc↑ (black) and its demetalized product, Pc (green) in an ordered array on 3 ML of Pb. For comparison the spectrum of PbPc↓ (red) on the same Pb island is shown. An unoccupied molecular orbital (MO) gives rise to a broad peak in the spectra of PbPc↑ ($\approx 2.1\,\mathrm{V}$) and PbPc↓ ($\approx 2.2\,\mathrm{V}$). A quantum well state (QWS) of the Pb film appears as a weak shoulder in both spectra at $\approx 2\,\mathrm{V}$ [236]. The spectrum of demetalized Pc is featureless in this range. (b) Evolution of the current with tip displacement, $\Delta z$, towards the center of PbPc↑ molecules. Different colors show measurements from molecules on Pb islands with thicknesses between 3 and 8 ML. ($V = 2\,\mathrm{V}$, $\Delta z = 0\,\mathrm{pm}$ corresponds to the tip–molecule distance at 10 nA).

rent decrease is, therefore, a clear signal of the demetalation of the molecule. While a detailed interpretation of the current drop requires atomistic modeling, the experimental data indicate the relevant factors. The transfer of the Pb atom from the molecule to the tip alone would not necessarily reduce the conductance, however it has two side-effects. First, the spectroscopic signature of the molecular orbital at $\approx 2\,\mathrm{V}$ disappears. Second, the geometry of the molecule is expected to change from shuttlecock to flat. Both factors are likely to contribute to the conductance change. A possibly related observation was reported from $C_{60}$ on Cu(110), which is irreversibly changed at elevated currents [85]. In Figure 7.3b, small deviations from a purely exponential variation of $I$ with $\Delta z$ may be discerned. They most likely reflect relaxations of the junction, which result from attractive forces between the tip and the molecule.

## 7.4 Summary

In summary, an organometallic complex has been demetalized at the single-molecule level. Demetalation is evidenced by a combination of imaging, the transfer of the metal ion to the tip, and the spectroscopic fingerprint of the demetalized molecule. It will be interesting to use this reaction as a first step for subsequent metalation with atoms in order to tailor electronic or magnetic properties. Time-resolved measurements of the demetalation process may provide more details about breaking the chemical bonds between the central metal atom and the molecule.

## Acknowledgements

Financial support by the Deutsche Forschungsgemeinschaft through SFB 677 and discussions with W. A. Hofer, University of Liverpool, and R. Herges, Christian-Albrechts-Universität zu Kiel, are acknowledged.

# APPENDIX A

## *Markov process*

In probability theory, a Markov process, named after the Russian mathematician Andrey Markov, is a time-dependent stochastic process for which present state of the system, its future and past are independent [238].

Markov processes can be applied to describe the motion of some defects and impurities in solids. Their movement can be described by (thermally induced) hopping from one lattice site to a neighboring one. Each such hop usually requires surmounting an activation barrier. Therefore, the rate of hops of any individual defect is many times smaller than the frequency $\nu_0$ of attempts to surmount the barrier. After each hop, the crystal and the defect in its new position release the activation energy to phonons. The time to reach an equilibrium state is usually smaller by many orders of magnitude than the time between two consequent hops. That is why the defect 'forgets' its previous history long before the next hop occurs, the probability of which depends therefore on its present position only. Thus, hopping of defects in a solid is usually a Markov process.

Mathematically a Markov process with two bistable states can be described as follows:

The probability for a transition to the other state in the time interval $\Delta t$ is

$$P_{\text{transition}} = R\Delta t. \qquad (\Delta t \to 0)$$

The probability for a remaining in the given state is therefore

$$P_{\text{stay}} = 1 - R\Delta t. \qquad (\Delta t \to 0)$$

The probability for remaining in the given state after a time $t = n\Delta t$, which is called "lifetime", is thus

$$P(t) = \lim_{n\to\infty} (1 - R\frac{t}{n})^n = e^{-Rt}.$$

Then the probability density of the lifetime $t$ is given by

$$-\frac{dP(t)}{dt} = Re^{-Rt}.$$

The function is nonnegative and its integral over the entire space is equal to one.

Finally the average lifetime $\bar{\tau}$ of a state can be calculated as

$$\begin{aligned} \bar{\tau} &= \int_0^\infty t(-\frac{dP(t)}{dt})dt \\ &= \int_0^\infty tRe^{-Rt}dt \\ &= \frac{1}{R}. \end{aligned}$$

Here, it can be seen that the parameter $R$ is the inverse of the average lifetime $\bar{\tau}$ and therefore $R$ can be denoted as a mean transition rate.

# APPENDIX B

## *Development of a New Sample Preparation Station for High Temperatures*

### *Motivation*

During this thesis a new sample preparation station was developed. The following requirements had to be met: (a) filament exchange without breaking the vacuum, (b) sample temperatures in excess of 2300 K, (c) azimuthal rotation and $z$ translation of the sample, and (d) mounting on a small DN 38 CF flange.

### *Design*

An overview of the preparation station is given in Figure 7.4. In order to obtain temperatures of more than 2300 K the whole station down from the lower insulating macor plate (1 in Figure 7.4a) is manufactured from molybdenum or high purity alumina ($Al_2O_3$). In detail, the preparation station has two electrically contacted pins for a removable filament (2) as well as two other electrically contacted pins for the sample (3). The electrical connections to the filament (4) and sample (5) are covered by alumina beads for insulation (not shown in the Figure). The pins are electrically isolated by alumina split bushes from the left and right arm of the station. Additionally the arms are isolated by alumina split bushes (6) as well from the center part, which is connected to ground. The sample annealing is carried out by electron bombardment, where a high voltage up to 3500 V is applied to the sample. Therefore attention must be kept on avoiding of short circuits. During evaporation of metals not only the sample will be hit by the metal atoms but the whole preparation station as well. Thus a shielding metal plate (7) is mounted at the side of the arm where the sample is placed on the station to avoid a coating of the insulating ceramics by thin conducting metal films. Figure 7.4b shows the top view of the preparation station. The circle represents the diameter (38 mm) of the flange at the preparation chamber where

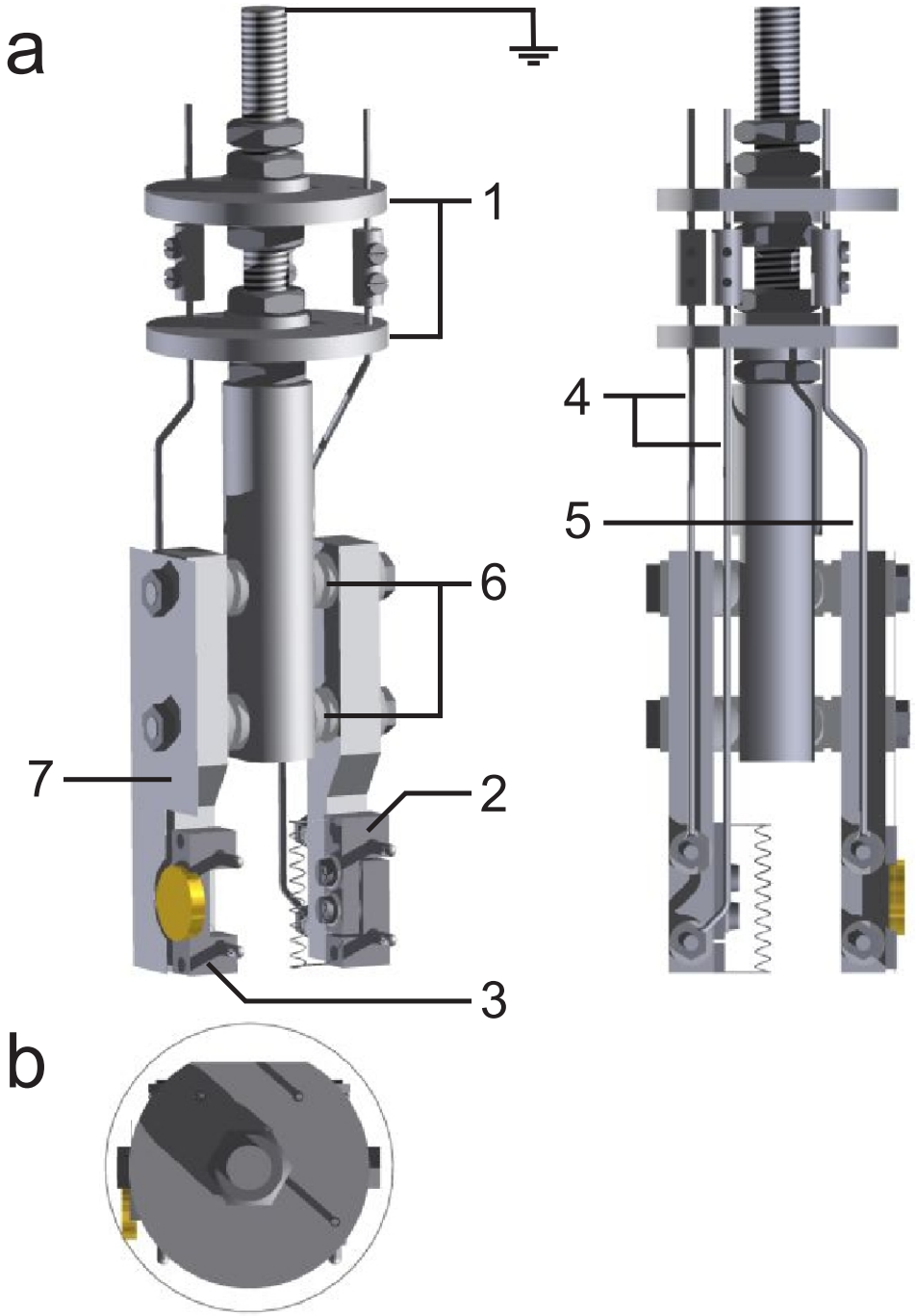


*Fig. 7.4:* Full-scale side (a) and top (b) view of the sample preparation station. Indicated parts (detailed description in the text): (1) Macor plates, (2) filament holder, (3) sample, (4+5) electrical connections to the filament and sample, (6) alumina split bushes and (7) shielding metal plate. The circle in (b) illustrates the diameter (38 mm) of the mounting flange at the preparation chamber where the whole preparation station has to fit through.

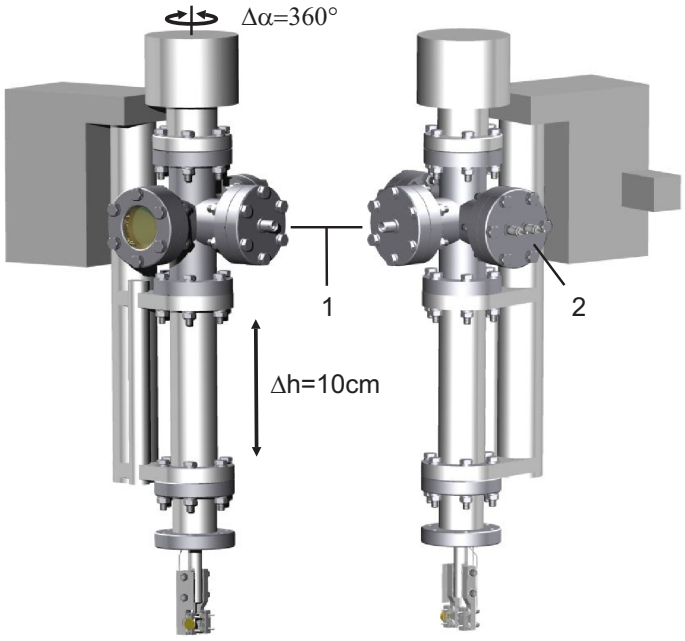


*Fig. 7.5:* Overview of the manipulator with the attached sample preparation station at the bottom. The feedthroughs for the high voltage (1) and the filament current (2) are indicated.

the whole preparation station has to fit through.

To ensure the required rotation and height adjustment a rotary drive and a linear transfer mechanism are attached to the preparation station as can be seen in Figure 7.5. The linear transfer mechanism allows a maximum height variation of 10 cm and is moved by a stepper motor. The rotary drive is manually controlled and allows a rotation of 360 °. The feedthroughs for the high voltage (1) and the filament current (2) are not rotatable, but the cables from the feedthroughs to the preparation station are flexible wires, which are coiled around the rotation axis. However, to prevent cable rupture rotations by more than 360 ° are not recommended.

### *Test and Calibration*

As described above the sample heating is carried out by electron bombardment. The heating power $P_{in}$ which is applied to the sample is the product

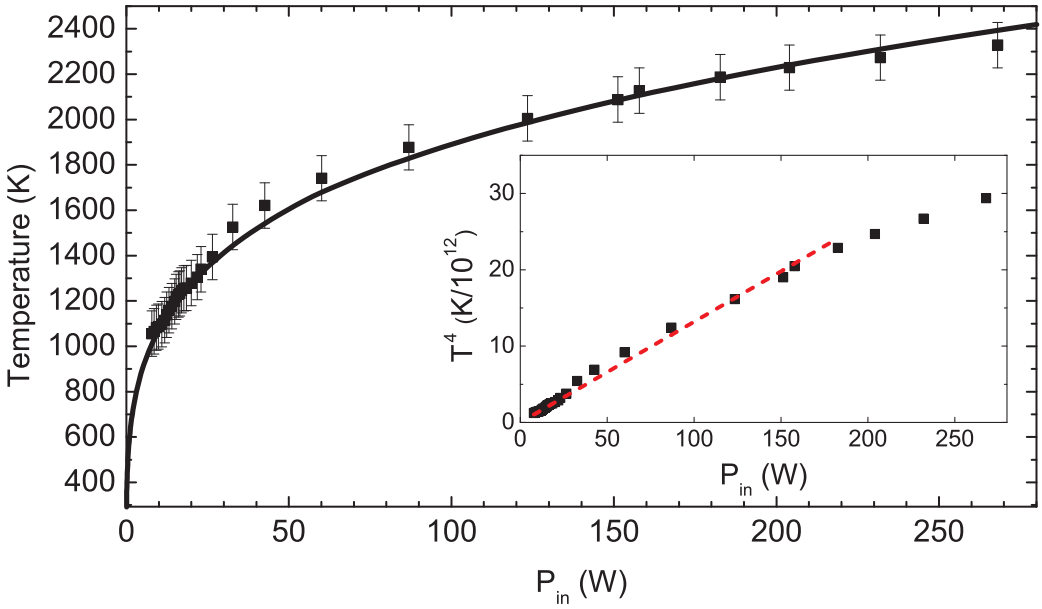


*Fig. 7.6:* Sample temperature as a function of applied heating power. The solid line is a fit to the date using Equation (7.1). Inset: Temperature to the power of 4 as a function of heating power. The dashed line is a guide to the eyes which indicates the temperature range ($T < 2200\,\mathrm{K}$) at which the released energy by heat conduction is negligible compared to the energy released by heat radiation.

of the emission current and voltage. In thermal equilibrium this power will be completely released by heat radiation $P_R$ as well as heat conduction $P_C$:

$$\begin{aligned} P_{in} &= P_{out} \\ &= P_R + P_C \\ &= aT^4 + b(T - T_{RT}). \end{aligned} \tag{7.1}$$

$T_{RT}$ is the ambient temperature which is $\approx 20\,^{\circ}\mathrm{C}$ and $a$ and $b$ are constants which can be tuned more or less by the experimental setup. To maximize the temperature of the sample, $T$, both factors should be minimized. While the heat radiation of the sample and sample holder cannot be suppressed, the heat conduction can be minimized by using a thin cable for the high voltage connection to the sample and small contact areas between sample and preparation station.

The obtained temperatures of the sample are recorded by an external pyrometer. Due to the unknown spectral transmissivity of the viewport of the preparation chamber, the unknown exact emissivity of the sample ( which is dependent on the temperature) and a non-uniform heating of the sample

and sample holder the systematic error in the measurement of the temperature is estimated to be approximately ±100 K, while the statistic error is less than 5 K. Figure 7.6 shows the temperature as a function of applied heating power, $P_{in}$. The maximum temperature during the tests was 2328 K with a heating power of 268 W.[3] The solid line is a fit to the data points using Equation (7.1). In the inset of Figure 7.6 $T^4$ is drawn without systematic errors as a function of applied heating power. The almost linear behavior of $T^4$ as a function of $P_{in}$ up to temperatures of $\approx$ 2200 K indicates that the main part of the applied heating power is released by heat radiation of the sample while heat conduction can be neglected, *i. e.*, here $P_R \gg P_C$. For higher temperatures the deviation of the linear behavior of $T^4$ as a function of $P_{in}$ is most likely due to heat radiation of neighboring parts which must be taken into account. Furthermore $b$ is most likely not constant over the full temperature range. Rather $b$ increases with temperature. The longitudinal expansion coefficients of molybdenum as well as alumina are positive. Therefore all parts of the preparation station expand during heating. This leads to a higher contact pressure between the various parts of the preparation station resulting in a higher transfer of thermal energy away from the sample with increasing temperature.

Overall the preparation station meets the requirements. It has been operated since August 2009 and contributed to various own publications [235, 236, 239]. For the future it permits a planned automatization of the whole sputter and annealing process, which will further facilitate the experimental preparation.

[3] The maximum output of the power supply is 700 W. Consequently significantly higher temperatures are feasible.

# ACKNOWLEDGEMENT

A work like this cannot be accomplished without a lot of help. I thank

- Prof. Dr. Richard Berndt for the possibility to work in his group, his many tips and fruitful discussions,
- Prof. Dr. Jörg Kröger, who guided me for the past years, let me work on his STM and always had a sympathetic ear for my questions,
- Dr. Nicolas Néel for supporting me in my experiments,
- Dr. Michael Becker for countless fruitful discussions ☺,
- Lars Mühlenberend and Simon Altenburg for the enjoyable atmosphere in our office,
- Monika Seeger for helping me tunneling through administrative barriers,
- Mr. Brach, Mr. Brix, and the staff of the workshop for the precise manufacturing of the parts of the new sample preparation station,
- the remaining and former co-workers of the group: Andreas Burtzlaff, Dr. Thiruvancheril Gopakumar, Dr. Markus Gruyters, Christian Hamann, Nadine Hauptmann, Dr. I-Po Hong, Henning Jensen, Dr. Thomas Jürgens, Sujoy Karan, Dr. Francesca Matino, Svenja Mühlenberend, Jörg Neubauer, Torben Pingel, Dr. Jürgen Rathlev, Nico Ruppelt, Katharina Scheil, Natalia Schneider, Johannes Schöneberg, Dr. Guillaume Schull, Dr. Yongfeng Wang, Dr. Alexander Weismann, René Woltmann, Dr. Hao Zheng, Dr. Martin Ziegler for the nice working atmosphere and a lot of fun,
- Addi and Dr. Lüddi for their unconditional love,
- Heidi and Jörg for countless recreative hours in Revensdorf,
- last but not least my parents Christa and Wenzel, who always encouraged me in my studies.

Part of this work was supported by the DFG-Schwerpunktprogramm 1153, the SFB 677 and the Schleswig-Holstein Fonds, which are gratefully acknowledged.

# BIBLIOGRAPHY


[1] J. A. Stroscio and R. J. Celotta, Science **306**, 242 (2004).

[2] J. A. Stroscio *et al.*, Science **313**, 948 (2006).

[3] A. van Houselt and H. J. W. Zandvliet, Rev. Mod. Phys. **82**, 1593 (2010).

[4] O. M. Magnussen *et al.*, Electrochim. Acta **46**, 3725 (2001).

[5] T. Tansel, A. Taranovskyy, and O. M. Magnussen, Chem. Phys. Chem. **11**, 1438 (2010).

[6] V. Gerstner *et al.*, J. Appl. Phys. **88**, 4851 (2000).

[7] O. Takeuchi *et al.*, Appl. Phys. Lett. **85**, 3268 (2004).

[8] Y. Terada *et al.*, Nanotechnology **18**, 044028 (2007).

[9] N. Nilius, T. M. Wallis, M. Persson, and W. Ho, Phys. Rev. Lett. **90**, 196103 (2003).

[10] C. C. Leznoff and A. B. P. Lever, *Phthalocyanines: Properties and Applications* (VCH, Weinheim, 1989).

[11] G. de la Torre, C. G. Claessens, and T. Torres, Chem. Commun. **20**, 2000 (2007).

[12] G. Binnig, H. Rohrer, Ch. Gerber, and E. Weibel, Phys. Rev. Lett. **49**, 57 (1982).

[13] D. M. Eigler and E. K. Schweizer, Nature **344**, 524 (1990).

[14] L. Bartels, G. Meyer, and K.-H. Rieder, Phys. Rev. Lett. **79**, 697 (1997).

[15] S.-W. Hla, K.-F. Braun, B. Wassermann, and K.-H. Rieder, Phys. Rev. Lett. **93**, 208302 (2004).

[16] D. M. Eigler, C. P. Lutz, and W. E. Rudge, Nature **352**, 600 (1991).

[17] L. Bartels *et al.*, Phys. Rev. Lett. **80**, 2004 (1998).

[18] G. Dujardin *et al.*, Phys. Rev. Lett. **80**, 3085 (1998).

[19] S. Fölsch, J. Yang, C. Nacci, and K. Kanisawa, Phys. Rev. Lett. **103**, 096104 (2009).

[20] G. Schull, T. Frederiksen, M. Brandbyge, and R. Berndt, Phys. Rev. Lett. **103**, 206803 (2009).

[21] G. Schull *et al.*, Nature Nanotechnology **6**, 23 (2010).

[22] N. Nilius, T. M. Wallis, and W. Ho, Science **297**, 1853 (2002).

[23] S. Fölsch, P. Hyldgaard, R. Koch, and K. H. Ploog, Phys. Rev. Lett. **92**, 056803 (2004).

[24] N. Nilius, T. M. Wallis, and W. Ho, Applied Physics A **80**, 951 (2005).

[25] J. Lagoute, C. Nacci, and S. Fölsch, Phys. Rev. Lett. **98**, 146804 (2007).

[26] A. Sperl *et al.*, Phys. Rev. B **77**, 085422 (2008).

[27] J. Lagoute, X. Liu, and S. Fölsch, Phys. Rev. Lett. **95**, 136801 (2005).

[28] J. Kliewer, R. Berndt, J. Minár, and H. Ebert, Appl. Phys. A **82**, 63 (2006).

[29] N. Néel *et al.*, Phys. Rev. Lett. **101**, 266803 (2008).

[30] J. Lagoute and S. Fölsch, J. Vac. Sci. Technol. B **23**, 1726 (2005).

[31] H. Jensen, Diploma thesis, 2003.

[32] C. J. Chen, *Introduction to Scanning Tunneling Microscopy* (Oxford University Press, 1993).

[33] R. J. Hamers, in *Scanning Tunneling Microscopy and Spectroscopy. Theory, Techniques, and Applications*, edited by D. A. Bonnell (VCH, New York, 1993).

[34] R. Wiesendanger, *Scanning Probe Microscopy. Methods and Applications* (Cambridge University Press, 1994).

[35] J. Stroscio and W. Kaiser, *Scanning Tunneling Microscopy* (Academic Press Inc, 1994).

[36] H. Güntherodt and R. Wiesendanger, *Scanning Tunneling Microscopy I: General Principles and Applications to Clean and Adsorbate–covered Surfaces v. 1* (Berlin: Springer, 1994).

[37] A. Foster and W. Hofer, *Scanning Probe Microscopy: Atomic Scale Engineering by Forces and Currents* (Berlin: Springer, 2006).

[38] M. Bowker and W. Hofer, *Scanning Tunneling Microscopy in Surface Science* (Wiley-VCH, 2009).

[39] J. G. Simmons, J. Appl. Phys. **34**, 1793 (1963).

[40] J. G. Simmons, J. Appl. Phys. **34**, 2581 (1963).

[41] J. Bardeen, Phys. Rev. Lett. **6**, 57 (1961).

[42] V. A. Ukraintsev, Phys. Rev. B **53**, 11176 (1996).

[43] M. Ziegler *et al.*, Phys. Rev. B **80**, 125402 (2009).

[44] M. Ziegler, Ph.D. thesis, 2009.

[45] S. F. Alvarado, P. F. Seidler, D. G. Lidzey, and D. D. C. Bradley, Phys. Rev. Lett. **81**, 1082 (1998).

[46] M. Feng, J. Zhao, and H. Petek, Science **320**, 359 (2008).

[47] D. B. Dougherty *et al.*, Phys. Rev. B **77**, 073414 (2008).

[48] B. Koslowski, H. Pfeifer, and P. Ziemann, Phys. Rev. B **80**, 165419 (2009).

[49] R. M. Feenstra, J. A. Stroscio, and A. P. Fein, Surf. Sci. **181**, 295 (1987).

[50] B. Koslowski, C. Dietrich, A. Tschetschetkin, and P. Ziemann, Phys. Rev. B **75**, 35421 (2007).

[51] B. Naydenov and J. J. Boland, Phys. Rev. B **82**, 245411 (2010).

[52] M. F. Crommie, C. P. Lutz, and D. M. Eigler, Science **262**, 218 (1993).

[53] E. J. Heller, M. F. Crommie, C. P. Lutz, and D. M. Eigler, Nature **369**, 464 (1994).

[54] H. C. Manoharan, C. P. Lutz, and D. M. Eigler, Nature **403**, 512 (2000).

[55] J. Kliewer, R. Berndt, and S. Crampin, Phys. Rev. Lett. **85**, 4936 (2000).

[56] J. Kliewer, R. Berndt, and S. Crampin, New J. Phys. **3**, 22.1 (2001).

[57] S.-W. Hla, K.-F. Braun, and K.-H. Rieder, Phys. Rev. B **67**, 201402 (2003).

[58] T. M. Wallis, N. Nilius, G. Mikaelian, and W. Ho, J. Chem. Phys. **122**, 011101 (2005).

[59] J. Lagoute, X. Liu, and S. Fölsch, Phys. Rev. B **74**, 125410 (2006).

[60] Z. J. Donhauser *et al.*, Science **292**, 2303 (2001).

[61] A. J. Heinrich, C. P. Lutz, J. A. Gupta, and D. M. Eigler, Science **298**, 1381 (2002).

[62] X. H. Qiu, G. Nazin, and W. Ho, Phys. Rev. Lett. **93**, 196806 (2004).

[63] V. Iancu and S.-W. Hla, Proc. Natl. Acad. Sci. U. S. A. **103**, 13718 (2006).

[64] P. Liljeroth, J. Repp, and G. Meyer, Science **317**, 1203 (2007).

[65] M. Pivetta, M. Ternes, F. Patthey, and W.-D. Schneider, Phys. Rev. Lett. **99**, 126104 (2007).

[66] C. Nacci, J. Lagoute, X. Liu, and S. Fölsch, Phys. Rev. B **77**, 121405 (2008).

[67] C. Silien *et al.*, Nano Lett. **8**, 208 (2008).

[68] T. Kumagai *et al.*, Phys. Rev. B **79**, 035423 (2009).

[69] Y. Wang, J. Kröger, R. Berndt, and W. A. Hofer, J. Am. Chem. Soc. **131**, 3639 (2009).

[70] Y. F. Wang *et al.*, J. Am. Chem. Soc. **132**, 1196 (2010).

[71] A. Safiei, J. Henzl, and K. Morgenstern, Phys. Rev. Lett. **104**, 216102 (2010).

[72] S. Weigelt *et al.*, Nature Materials **5**, 112 (2006).

[73] F. Matino *et al.*, Chem. Commun. **46**, 6780 (2010).

[74] B. C. Stipe, M. A. Rezaei, and W. Ho, Science **279**, 1907 (1998).

[75] L. Gao *et al.*, Phys. Rev. Lett. **101**, 197209 (2008).

[76] N. Néel, L. Limot, J. Kröger, and R. Berndt, Phys. Rev. B **77**, 125431 (2008).

[77] R. Nouchi *et al.*, Phys. Rev. Lett. **97**, 196101 (2006).

[78] X. Ge *et al.*, J. Am. Chem. Soc. **131**, 6096 (2009).

[79] M. Nakaya *et al.*, Advanced Materials **22**, 1622 (2010).

[80] L. J. Lauhon and W. Ho, Phys. Rev. Lett. **84**, 1527 (2000).

[81] A. Zhao *et al.*, Science **309**, 1542 (2005).

[82] N. Baadji *et al.*, Phys. Rev. B **82**, 115447 (2010).

[83] Y. F. Wang *et al.*, Phys. Rev. Lett. **104**, 176802 (2010).

[84] S.-W. Hla, G. Meyer, and K.-H. Rieder, Chem. Phys. Lett. **370**, 431 (2003).

[85] G. Schulze *et al.*, Phys. Rev. Lett. **100**, 136801 (2008).

[86] J. Repp, G. Meyer, K.-H. Rieder, and P. Hyldgaard, Phys. Rev. Lett. **91**, 206102 (2003).

[87] A. Saedi *et al.*, Nano Lett. **9**, 1733 (2009).

[88] A. Sperl, J. Kröger, and R. Berndt, Phys. Rev. B **81**, 035406 (2010).

[89] J. K. Gimzewski, R. Möller, D. W. Pohl, and R. R. Schlittler, Surf. Sci. **189**, 15 (1987).

[90] N. Agraït, J. G. Rodrigo, and S. Vieira, Phys. Rev. B **47**, 12345 (1993).

[91] L. Limot *et al.*, Phys. Rev. Lett. **94**, 126102 (2005).

[92] N. Néel *et al.*, Phys. Rev. Lett. **98**, 065502 (2007).

[93] J. Kröger *et al.*, New J. Phys. **11**, 125006 (2009).

[94] J. Repp, G. Meyer, F. E. Olsson, and M. Persson, Science **305**, 493 (2004).

[95] Datasheet of DHPCA-100 on www.femto.de.

[96] Datasheet of DLPCA-200 on www.femto.de.

[97] M. Persson, Phys. Rev. B **70**, 205420 (2004).

[98] F. E. Olsson *et al.*, Phys. Rev. Lett. **93**, 206830 (2004).

[99] L. Limot, E. Pehlke, J. Kröger, and R. Berndt, Phys. Rev. Lett. **94**, 036805 (2005).

[100] J. Kröger *et al.*, Prog. Surf. Sci. **80**, 26 (2005).

[101] J. Bansmann *et al.*, Surf. Sci. Rep. **56**, 189 (2005).

[102] S. Abbet *et al.*, J. Am. Chem. Soc. **122**, 3453 (2000).

[103] S. Abbet, A. Sanchez, U. Heiz, and W.-D. Schneider, J. Catal. **198**, 122 (2001).

[104] B. Lewis and J. C. Anderson, *Nucleation and growth of thin films* (New York: Academic, 1978).

[105] J. A. Venables, G. D. T. Spiller, and M. Hanbucken, Rep. Prog. Phys. **47**, 399 (1984).

[106] H. Brune, Surf. Sci. Rep. **31**, 121 (1998).

[107] S. Fedrigo, W. Harbich, and J. Buffet, J. Chem. Phys. **99**, 5712 (1993).

[108] H. Haberland, *Clusters of Atoms and Molecules* (Berlin: Springer, 1994).

[109] I. Rabin, W. Schulze, and G. Ertl, Chemical Physics Letters **312**, 394 (1999).

[110] K. H. Lau and W. Kohn, Surf. Sci. **75**, 69 (1978).

[111] M. M. Kamna, S. J. Stranick, and P. S. Weiss, Science **274**, 118 (1996).

[112] E. Wahlström, I. Ekvall, H. Olin, and L. Walldén, Appl. Phys. A **66**, S1107 (1998).

[113] J. Repp, F. Moresco, G. Meyer, and K.-H. Rieder, Phys. Rev. Lett. **85**, 2981 (2000).

[114] N. Knorr *et al.*, Phys. Rev. B **65**, 115420 (2002).

[115] F. Silly *et al.*, Phys. Rev. Lett. **92**, 016101 (2004).

[116] T. von Hofe, J. Kröger, and R. Berndt, Phys. Rev. B **73**, 245434 (2006).

[117] M. Ziegler *et al.*, Phys. Rev. B **78**, 245427 (2008).

[118] N. Néel *et al.*, Phys. Rev. Lett. **98**, 016801 (2007).

[119] J. A. Stroscio, R. M. Feenstra, and A. P. Fein, Phys. Rev. Lett. **57**, 2579 (1986).

[120] L. Limot, T. Maroutian, P. Johansson, and R. Berndt, Phys. Rev. Lett. **91**, 196801 (2003).

[121] J. Kröger, L. Limot, H. Jensen, and R. Berndt, Phys. Rev. B **70**, 033401 (2004).

[122] G. Kresse and J. Hafner, Phys. Rev. B **47**, 558 (1993).

[123] G. Kresse and J. Hafner, Phys. Rev. B **49**, 14251 (1994).

[124] G. Kresse and J. Furthmüller, Comput. Mater. Sci. **6**, 15 (1996).

[125] G. Kresse and J. Furthmüller, Phys. Rev. B **54**, 11169 (1996).

[126] J. P. Perdew *et al.*, Phys. Rev. B **46**, 6671 (1992).

[127] P. E. Blöchl, Phys. Rev. B **50**, 17953 (1994).

[128] G. Kresse and D. Joubert, Phys. Rev. B **59**, 1758 (1999).

[129] T. Klamroth and P. Saalfrank, Surf. Sci. **410**, 21 (1998).

[130] S. D. Kevan and R. H. Gaylord, Phys. Rev. B **36**, 5809 (1987).

[131] S.-C. Liu *et al.*, Phys. Rev. B **39**, 13149 (1989).

[132] G. R. Castro, H. Dürr, R. Fischer, and T. Fauster, Phys. Rev. B **45**, 11989 (1992).

[133] Z. Song *et al.*, Appl. Phys. A **72**, S159 (2001).

[134] D. G. Cahill *et al.*, J. Appl. Phys. **93**, 793 (2003).

[135] A. Pecchia, G. Romano, and A. Di Carlo, Phys. Rev. B **75**, 035401 (2007).

[136] Z. Huang *et al.*, Nano Lett. **6**, 1240 (2006).

[137] N. Néel, J. Kröger, and R. Berndt, Nanotechnology **18**, 044027 (2007).

[138] K. Schouteden *et al.*, New Journal of Physics **10**, 043016 (2008).

[139] K. S. Ralls and R. A. Buhrman, Phys. Rev. Lett. **60**, 2434 (1988).

[140] K. S. Ralls, D. C. Ralph, and R. A. Buhrman, Phys. Rev. B **40**, 11561 (1989).

[141] P. A. M. Holweg, J. Caro, A. H. Verbruggen, and S. Radelaar, Phys. Rev. B **45**, 9311 (1992).

[142] H. E. van den Brom, A. I. Yanson, and J. M. van Ruitenbeek, Physica B **252**, 69 (1998).

[143] J. Kröger, N. Néel, and L. Limot, J. Phys.: Condens. Matter **20**, 223001 (2008).

[144] S.-W. Hla, J. Vac. Sci. Technol. B **23**, 1351 (2005).

[145] T. N. Todorov, Philos. Mag. B **77**, 965 (1998).

[146] T. N. Todorov, J. Hoekstra, and A. P. Sutton, Phys. Rev. Lett. **86**, 3606 (2001).

[147] R. H. M. Smit, C. Untiedt, and J. M. van Ruitenbeek, Nanotechnology **15**, S472 (2004).

[148] M. Tsutsui, Y. Teramae, S. Kurokawa, and A. Sakai, Appl. Surf. Sci. **252**, 8677 (2006).

[149] S. Gao, M. Persson, and B. I. Lundqvist, Solid State Commun. **84**, 271 (1992).

[150] R. E. Walkup, D. M. Newns, and P. Avouris, Phys. Rev. B **48**, 1858 (1993).

[151] M. Brandbyge and P. Hedegård, Phys. Rev. Lett. **72**, 2919 (1994).

[152] S. Gao, M. Persson, and B. I. Lundqvist, Phys. Rev. B **55**, 4825 (1997).

[153] G. Boisvert, L. J. Lewis, and A. Yelon, Phys. Rev. Lett. **75**, 469 (1995).

[154] M. F. Bertino, F. Hofmann, W. Steinhögl, and J. P. Toennies, J. Chem. Phys. **105**, 11297 (1996).

[155] B. G. Briner, M. Doering, H.-P. Rust, and A. M. Bradshaw, Science **278**, 257 (1997).

[156] S. Ovesson, A. Bogicevic, G. Wahnström, and B. I. Lundqvist, Phys. Rev. **64**, 125423 (2001).

[157] J. V. Barth *et al.*, Phys. Rev. Lett. **84**, 1732 (2000).

[158] H. Brune *et al.*, Phys. Rev. B **52**, R14380 (1995).

[159] B. Fischer *et al.*, Phys. Rev. Lett. **82**, 1732 (1999).

[160] H. Yildirim, A. Kara, and T. S. Rahman, Phys. Rev. B **75**, 205409 (2007).

[161] A. Kühnle, G. Meyer, S. Hla, and K.-H. Rieder, Surf. Sci. **499**, 15 (2002).

[162] Y.-C. Chen, M. Zwolak, and M. Di Ventra, Nano Lett. **3**, 1691 (2003).

[163] G. Romano, A. Pecchia, and A. Di Carlo, J. Phys.: Condens. Matter **19**, 215207 (2007).

[164] J. Kröger, Rep. Prog. Phys. **69**, 899 (2006).

[165] S. D. Borisova *et al.*, Phys. Rev. B **78**, 075428 (2008).

[166] J. M. Gottfried *et al.*, J. Am. Chem. Soc. **128**, 5644 (2006).

[167] T. E. Shubina *et al.*, J. Am. Chem. Soc. **129**, 9476 (2007).

[168] F. Buchner *et al.*, ChemPhysChem **8**, 241 (2007).

[169] K. Flechtner *et al.*, J. Phys. Chem. C **111**, 5821 (2007).

[170] Y. Bai *et al.*, J. Phys. Chem. C **112**, 6087 (2008).

[171] F. Buchner *et al.*, J. Phys. Chem. C **112**, 15458 (2008).

[172] A. Weber-Bargioni *et al.*, J. Phys. Chem. C **112**, 3453 (2008).

[173] J. M. Gottfried and H. Marbach, Z. Phys. Chem. **223**, 53 (2009).

[174] C.-L. Song *et al.*, J. Am. Chem. Soc. **132**, 1456 (2010).

[175] A. Kretschmann *et al.*, Chem. Commun. **6**, 568 (2007).

[176] R. Cuadrado *et al.*, J. Chem. Phys. **133**, 154701 (2010).

[177] B. W. Heinrich *et al.*, J. Phys. Chem. Lett. **1**, 1517 (2010).

[178] S.-H. Chang *et al.*, Phys. Rev. B **78**, 233409 (2008).

[179] H. Karacuban *et al.*, Surf. Sci. **603**, L39 (2009).

[180] A. F. Takács *et al.*, Phys. Rev. B **78**, 233404 (2008).

[181] A. Scarfato *et al.*, Surf. Sci. **602**, 677 (2008).

[182] Y. F. Wang, J. Kröger, R. Berndt, and W. A. Hofer, Angew. Chem. Int. Ed. **48**, 1261 (2009).

[183] R. S. Becker, J. A. Golovchenko, and B. S. Swartzentruber, Nature **325**, 419 (1987).

[184] M. Ziegler *et al.*, Appl. Phys. Lett. **96**, 132505 (2010).

[185] A. Pecchia, G. Romano, and A. D. Carlo, Phys. Rev. B **75**, 035401 (2007).

[186] F. Netzer and M. Ramsey, Crit. Rev. Solid State Mater. Sci. **17**, 397 (1992).

[187] N. Sheppard and C. de la Cruz, Adv. Catal. **42**, 181 (1998).

[188] S. Barlow and R. Raval, Surf. Sci. Rep. **50**, 201 (2003).

[189] S. D. Feyter and F. C. D. Schryver, Chem. Soc. Rev. **32**, 139 (2003).

[190] J. V. Barth, Annu. Rev. Phys. Chem. **58**, 375 (2007).

[191] L. Bartels, Nat. Chem. **2**, 87 (2010).

[192] S. C. B. Mannsfeld, K. Leo, and T. Fritz, Phys. Rev. Lett. **94**, 056104 (2005).

[193] S. Lukas, G. Witte, and C. Wöll, Phys. Rev. Lett. **88**, 028301 (2002).

[194] Y. Wang *et al.*, J. Am. Chem. Soc. **131**, 10400 (2009).

[195] N. Weiss *et al.*, Phys. Rev. Lett. **95**, 157204 (2005).

[196] N. Néel, J. Kröger, and R. Berndt, Advanced Materials **18**, 174 (2006).

[197] N. Néel, J. Kröger, and R. Berndt, Appl. Phys. Lett. **88**, 163101 (2006).

[198] J. Kröger *et al.*, Chem. Phys. Lett. **438**, 249 (2007).

[199] J. Kröger, H. Jensen, N. Néel, and R. Berndt, Surf. Sci. **601**, 4180 (2007).

[200] M. Corso *et al.*, Science **303**, 217 (2004).

[201] H. Dil *et al.*, Science **319**, 1824 (2008).

[202] J. A. Theobald *et al.*, Nature **424**, 1029 (2003).

[203] S. Stepanow *et al.*, Nat. Mater. **3**, 229 (2004).

[204] N. Nilius, E. D. L. Rienks, H.-P. Rust, and H.-J. Freund, Phys. Rev. Lett. **95**, 066101 (2005).

[205] A. T. N´Diaye, S. Bleikamp, P. J. Feibelman, and T. Michely, Phys. Rev. Lett. **97**, 215501 (2006).

[206] X. Lin and N. Nilius, J. Phys. Chem. C **112**, 15325 (2008).

[207] T. G. Gopakumar, N. Néel, J. Kröger, and R. Berndt, Chem. Phys. Lett. **484**, 59 (2009).

[208] C. Rogero, J. I. Pascual, J. Gómez-Herrero, and A. M. Baró, J. Chem. Phys. **116**, 832 (2002).

[209] S. Berner *et al.*, Phys. Rev. B **68**, 115410 (2003).

[210] J. Martínez-Blanco, M. Klingsporn, and K. Horn, Surf. Sci. **604**, 523 (2010).

[211] W. Auwärter *et al.*, Phys. Rev. B **81**, 245403 (2010).

[212] A. Rolland, J. Bernadinia, and M. Barthes-Labrousse, Surf. Sci. **143**, 579 (1984).

[213] C. R. Ast *et al.*, Phys. Rev. B **73**, 245428 (2006).

[214] M. Becker and R. Berndt, Phys. Rev. B **81**, 205438 (2010).

[215] R. Strohmaier *et al.*, J. Vac. Sci. Technol. B **14**, 1079 (1996).

[216] J. D. Baran *et al.*, Phys. Rev. B **81**, 075413 (2010).

[217] J. Dalmas *et al.*, Phys. Rev. B **72**, 155424 (2005).

[218] Y. F. Wang, J. Kröger, R. Berndt, and W. A. Hofer, Angew. Chem. **121**, 1287 (2009).

[219] J. D. Baran and J. A. Larsson, Phys. Chem. Chem. Phys. **12**, 6179 (2010).

[220] H. Yanagi, K. Ikuta, H. Mukai, and T. Shibutani, Nano Lett. **2**, 951 (2002).

[221] F. K. Schulte, Surf. Sci. **55**, 427 (1976).

[222] C. M. Wei and M. Y. Chou, Phys. Rev. B **66**, 233408 (2002).

[223] Y. Qi *et al.*, Appl. Phys. Lett. **90**, 013109 (2007).

[224] M. Becker and R. Berndt, Appl. Phys. Lett. **96**, 33112 (2010).

[225] P. M. Echenique and J. B. Pendry, J. Phys. C **11**, 2065 (1978).

[226] N. V. Smith, Phys. Rev. B **32**, 3549 (1985).

[227] E. V. Chulkov, V. M. Silkin, and P. M. Echenique, Surface Science **437**, 330 (1999).

[228] N. V. Smith, N. B. Brookes, Y. Chang, and P. D. Johnson, Phys. Rev. B **49**, 332 (1994).

[229] P. Echenique and J. Pendry, Progress in Surface Science **32**, 111 (1989).

[230] E. G. McRae and M. L. Kane, Surface Science **108**, 435 (1981).

[231] *The Porphyrin Handbook*, edited by K. M. Khadis, K. M. Smith, and R. Guilard (Academic Press, 1999).

[232] C. Isvoranu *et al.*, J. Phys.: Condens. Matter **22**, 472001 (2010).

[233] R. Strohmaier *et al.*, J. Vac. Sci. Technol. B **14**, 1079 (1996).

[234] T. Lukasczyk *et al.*, J. Phys. Chem. C **111**, 3090 (2007).

[235] A. Sperl, J. Kröger, and R. Berndt, Angew. Chem. Int. Ed. **50**, 5294 (2011).

[236] A. Sperl, J. Kröger, and R. Berndt, J. Phys. Chem. A, to be published (2011).

[237] J. Repp *et al.*, Phys. Rev. Lett. **94**, 026803 (2005).

[238] S. Kogan, *Electronic noise and fluctuations in solids* (Cambridge University Press, 1996).

[239] A. Sperl, J. Kröger, and R. Berndt, submitted to J. Am. Chem. Soc. (2011).

# CURRICULUM VITAE

| | |
|---|---|
| Name: | Sperl |
| First Name: | Alexander Nicolai |
| Date of Birth: | January 1, 1982 |
| Place of Birth: | Kiel |
| Nationality: | German |

| | |
|---|---|
| August 1988 – June 1992 | Grundschule Gettorf |
| August 1993 – June 2001 | Humboldt-Schule Kiel |
| October 2001 – September 2002 | Basic Military Service in Goslar and Husum |
| October 2004 | Vordiplom in Physics |
| February 2008 | Diplom in Physics |

**Prices:**

- Poster Price at the 21. Edgar Lüscher Seminar 2010 in Klosters, Switzerland
- Poster Price at the 22. Edgar Lüscher Seminar 2011 in Klosters, Switzerland

# LIST OF PUBLICATIONS

**Complete List of the Author´s Peer-Reviewed Journal Publications**

1. A. Sperl, J. Kröger, N. Néel, H. Jensen, R. Berndt, A. Franke, and E. Pehlke
*Unoccupied States of Individual Silver Clusters and Chains on Ag(111)*,
Phys. Rev. B **77**, 085422 (2008).

2. A. Sperl, J. Kröger, R. Berndt, A. Franke, and E. Pehlke,
*Evolution of Unoccupied Resonance During the Synthesis of a Silver Dimer on Ag(111)*,
New J. Phys. **11**, 063020 (2009).

3. J. Kröger, N. Néel, A. Sperl, Y. Wang, and R. Berndt,
*Single-Atom Contacts with a Scanning Tunnelling Microscope*,
New J. Phys. **11**, 125006 (2009).

4. M. Ziegler, N. Néel, A. Sperl, J. Kröger, and R. Berndt,
*Local Density of States from Constant-Current Tunneling Spectra*,
Phys. Rev. B **80**, 125402 (2009).

5. J. Kröger, A. Sperl, N. Néel, and R. Berndt,
*Scanning Tunneling Microscopic Investigations into the Conductance of Single-Atom Junctions*,
J. Scan. Prob. Microsc. **4**, 49 (2009).

6. A. Sperl, J. Kröger, and R. Berndt,
*Direct Observation of Conductance Fluctuations of a Single-Atom Tunneling Contact*,
Phys. Rev. B **81**, 035406 (2010).

7. A. Sperl, J. Kröger, and R. Berndt,
*Conductance of Ag atoms and Clusters on Ag(111): Spectroscopic and Time-Resolved Data*,
Phys. Status Solidi B **247**, 1077 (2010).

8. A. Sperl, J. Kröger, and R. Berndt,
*Electronic Superstructure of Lead-Phthalocyanine on Lead Islands*,
accepted for publication in J. Phys. Chem. A (2011).

9. A. Sperl, J. Kröger, and R. Berndt,
*Controlled Metalation of a Single Adsorbed Phthalocyanine*,
Angew. Chem. Int. Ed. **50**, 5294 (2011), Hot Paper.

10. A. Sperl, J. Kröger, and R. Berndt,
*Demetalation of a Single Organometallic Complex*,
submitted to J. Am. Chem. Soc..

Hiermit erkläre ich an Eides Statt, dass ich diese Arbeit selbständig unter der Beratung meiner wissenschaftlichen Lehrer und nur mit den angegebenen Hilfsmitteln erstellt habe. Diese Arbeit wurde weder ganz noch in Teilen an anderer Stelle im Rahmen eines Prüfungsverfahrens vorgelegt. Frühere Promotionsversuche wurden von mir nicht vorgenommen.

Kiel, den 2011

_____

(Alexander Sperl)